

THE EFFECT OF THE MADDEN-JULIAN OSCILLATION ON THE
ENERGETICS AND PREDICTION OF EL NIÑO-SOUTHERN OSCILLATION

by

Nicholas D. Lybarger
A Dissertation
Submitted to the
Graduate Faculty
of
George Mason University
In Partial fulfillment of
The Requirements for the Degree
of
Doctor of Philosophy
Climate Dynamics

Committee:

_____ Dr. Cristiana Stan, Committee Chair
_____ Dr. Bohua Huang, Committee Member
_____ Dr. Kathleen Pegion, Committee Member
_____ Dr. Joseph Weingartner, Committee Member
_____ Dr. James Kinter III, Department Chair
_____ Dr. Donna M. Fox, Associate Dean,
Office of Student Affairs and Special
Programs, College of Science
_____ Dr. Ali Andalibi, Interim Dean,
College of Science

Date: _____ Summer Semester 2019
George Mason University
Fairfax, VA

The Effect of the Madden-Julian Oscillation on the Energetics and Prediction of El Niño-Southern Oscillation

A dissertation submitted in partial fulfillment of the requirements for the degree of Doctor of Philosophy at George Mason University

By

Nicholas D. Lybarger
Bachelor of Science
Johns Hopkins University, 2013

Director: Dr. Cristiana Stan, Associate Professor
Department of Atmospheric, Oceanic, and Earth Sciences

Summer Semester 2019
George Mason University
Fairfax, VA

Copyright © 2019 by Nicholas D. Lybarger
All Rights Reserved

Dedication

I dedicate this dissertation to the love of my life, Emily Cortright, who is the motivation for everything I've achieved. Also to my mother and father, Cindy and David Lybarger, who gave me the tools to pursue my goals, and to the rest of my amazing family, whose love and support has been invaluable throughout my life.

Acknowledgments

I would like to thank the following people who made this possible. My advisor, Dr. Cristiana Stan, who never gave up on me. I would also like to thank my committee members, Dr. Bohua Huang, Dr. Kathy Pegion, and Dr. Joseph Weingartner. Finally, Dr. Ben Zaitchik, who inspired me to pursue this path through his passion and expertise.

Portions of Chapter 2 and Chapter 3 of this dissertation are reprinted by permission from Springer Nature Customer Service Centre GmbH: Springer Nature, *Climate Dynamics*, The effect of the MJO on the energetics of El Niño, Lybarger, N.D. and Stan, C., 2018. The final publication is available at <https://link.springer.com/article/10.1007%2Fs00382-017-4047-5>.

Table of Contents

| | Page |
|---------------------------------------------------------------------------------|------|
| List of Tables | vii |
| List of Figures | viii |
| Abstract | xv |
| 1 Introduction | 1 |
| 1.1 ENSO Theories | 1 |
| 1.1.1 Bjerknes Hypothesis | 2 |
| 1.1.2 Delayed Oscillator | 2 |
| 1.1.3 Recharge Oscillator | 3 |
| 1.1.4 Western Pacific Oscillator | 5 |
| 1.1.5 Advective - Reflective Oscillator | 6 |
| 1.1.6 Unified Oscillator | 7 |
| 1.1.7 Stable Mode Triggered by Stochastic Forcing | 7 |
| 1.2 MJO-ENSO Interactions | 7 |
| 1.2.1 Case Studies | 11 |
| 1.3 Objectives | 12 |
| 2 MJO-Kelvin Wave Energetics in Observations | 14 |
| 2.1 ENSO Energetics Framework | 14 |
| 2.2 Derivation of Terms | 15 |
| 2.3 Observational Datasets | 17 |
| 2.4 Application of MJO-Kelvin Energetics to Observations | 18 |
| 2.5 Discussion | 28 |
| 3 MJO-Kelvin Wave Energetics in SP-CCSM4 | 29 |
| 3.1 Model Description | 29 |
| 3.2 El Niño Comparisons | 33 |
| 3.3 Results | 37 |
| 3.4 Discussion | 47 |
| 4 Modification of MJO and Kelvin Wave Forcing in a Simple Ocean Model | 50 |
| 4.1 Model Description and Evaluation | 52 |
| 4.2 Control Experiments | 56 |

| | | |
|-------|-----------------------------------------------------|----|
| 4.3 | Sensitivity Experiment Description | 63 |
| 4.4 | Sensitivity Experiment Results | 65 |
| 4.4.1 | MJO Forcing Modification | 65 |
| 4.4.2 | Kelvin Wave Modification | 70 |
| 4.5 | Discussion | 71 |
| 5 | ENSO Prediction using EOF-Derived Indices | 75 |
| 5.1 | Data and Methods | 75 |
| 5.1.1 | MJO Wind Power | 76 |
| 5.1.2 | EOF Analysis | 79 |
| 5.2 | El Niño Predictors in Observations | 82 |
| 5.3 | El Niño Forecast in CFS-v2 | 90 |
| 5.4 | Discussion | 95 |
| | Bibliography | 98 |

List of Tables

| Table | Page |
|---------------------------------------------------------------------------------------------------------------------------------------------------------------------------------------------------------------------------------------------------------------------------------------------------------------------|------|
| 3.1 Comparison of El Niños included in each of the six composites. Along the left side is the corresponding composite, while along the top is the corresponding El Niño, numbered chronologically within the model run. | 36 |
| 4.1 Summary of control and sensitivity experiment design and nomenclature. . | 65 |
| 5.1 Contingency tables for April-May-June (top) and May-June-July (bottom) for <i>MaKE</i> used as a predictor. All 9 observed El Niño events are correctly predicted. The Heidke Skill Scores (HSS) for each period is also shown. . . | 84 |
| 5.2 Contingency tables for April-May-June (top) and May-June-July (bottom) for Niño 3.4 used as a predictor, as well as corresponding Heidke Skill Scores (HSS). | 85 |
| 5.3 Contingency tables for April-May-June (top) and May-June-July (bottom) for <i>MaKI</i> used as a predictor, as well as corresponding Heidke Skill Scores (HSS). It should be noted that this metric is only applied to the set of years predicted by the <i>MaKE</i> index to be El Niño events (n=17). | 87 |
| 5.4 <i>MaKE</i> contingency table as applied to CFS-v2 reforecasts of each year between 1980 and 2014. The Heidke Skill Score is shown. | 91 |
| 5.5 Niño 3.4 contingency table as applied to CFS-v2 reforecasts of each year between 1980 and 2014. The Heidke Skill Score is shown. | 91 |

List of Figures

| Figure | Page |
|-------------------------------------------------------------------------------------------------------------------------------------------------------------------------------------------------------------------------------------------------------------------------------------------------------------------------------------------------------------------------------------------------------------------------------------------------------------------------------------------------------------------------------------------------------------------------------------------------------------------------------------------------------------------------------------------------------------------------------------------------------------------------------------------------------------------------------------------------------------------------------------------------------|------|
| <p>1.1 Schematic diagram of the recharge-discharge oscillator conceptual model. Beginning with the warm phase (a), where positive SST anomalies in the eastern Pacific associated with westerly wind anomalies and a shallow thermocline drives Sverdrup divergence carrying heat away from the basin. This results in (b), the discharged ocean state, with basin-wide deep thermocline anomalies, leading to the development of (c), with a negative SST anomaly associated with easterly wind anomalies and Sverdrup transport of heat onto the equator, recharging the ocean. This induces to a basin wide shallow thermocline, leading to the development of a positive thermocline anomaly, thus resetting the cycle. The rectangular box represents the Pacific basin, and the plots of h represent thermocline depths anomalies across the basin. Reprinted from Jin (1997).</p> | 4 |
| <p>1.2 Schematic diagram of the western Pacific oscillator. L, C and H represent low SLP, cold SST and high SLP, respectively. τ_1 and τ_2 stand for zonal wind-stress anomalies in the Niño 4 and Niño 5 regions, respectively. T is the SST anomaly in the Niño 3 region and h is the thermocline-depth anomaly in the Niño 6 region. Reprinted from Wang, Chunzai, “A review of ENSO theories”, <i>National Science Review</i>, 2018, 5, by permission of Oxford University Press.</p> | 6 |
| <p>1.3 Schematic diagram of the MJO lifecycle (from top to bottom). Arrows represent circulation anomalies. Clouds represent condensation due to convective activity. Above each phase is a curve representing perturbations to the upper tropospheric pressure, while below each phase is a curve representing perturbations to the sea level pressure. Reprinted from Madden and Julian (1972).</p> | 10 |

| | | |
|-----|---------------------------------------------------------------------------------------------------------------------------------------------------------------------------------------------------------------------------------------------------------------------------------------------------------------------------------------------------------------------------------------------------------------------------------------------------------------------------------------------|----|
| 1.4 | Hovmöller diagram showing the evolution of monthly SST anomalies (a), zonal wind anomalies (b), and thermocline depth anomalies (c) averaged from 2°S - 2°N over the period January 1996 to December 2000. Data provided by the TAO/TRITON array (Hayes et al., 1991; McPhaden, 1995). Reprinted by permission from Springer Nature Customer Service Center GmbH: Springer Nature, Coral Reefs of the World, vol 8. by Wang C., Deser C., Yu JY., DiNezio P., and Clement A., 2017. | 12 |
| 2.1 | Composite of monthly APE_{mp} vs W_{mp} trajectories for El Niño (red) and La Niña (blue) in observations with two month smoothing applied. Solid lines indicate trajectories for the year leading up to an event, while dotted lines indicate trajectories for the year following the onset of the event. A heavy dot indicates January of the ENSO year, while an X marks December of the year following each event. | 19 |
| 2.2 | Composite of $W_{MJO,K}$ standard deviation spatial distribution for all El Niño events in observations. | 21 |
| 2.3 | January to July $W_{MJO,K}$ index time series prior to the peak of El Niño for the three events most affected by MJO (red) and the three events least affected by MJO (blue), as selected by the $W_{MJO,K}$ index. | 21 |
| 2.4 | Scatter plot of the $W_{MJO,K}$ index averaged between January and July prior to the peak of El Niño vs the DJF average Niño 3 index. Superimposed is the linear regression of DJF average Niño 3 index on the normalized $W_{MJO,K}$ index and the El Niño year corresponding to each point. Linear regression is significant at the 80% confidence level. | 22 |
| 2.5 | Composite Hovmöller diagram of the equatorially (5°S - 5°N) averaged Kelvin wave component of 20°C isotherm depth anomalies for El Niño events (n=3) which are most influenced by the MJO (a; 1997, 2006, and 2009) and El Niño events (n=3) which are least influenced by the MJO (b; 1991, 1994, and 2014). Units are meters. | 23 |
| 2.6 | Composite Hovmöller diagram of equatorially (5°S - 5°N) averaged zonal τ_{MJO} for El Niño events (n=3) which are most influenced by the MJO (a; 1997, 2006, and 2009) and El Niño events (n=3) which are least influenced by the MJO (b; 1991, 1994, and 2014). Units are $N \cdot m^{-2}$ | 24 |

| | | |
|-----|----------------------------------------------------------------------------------------------------------------------------------------------------------------------------------------------------------------------------------------------------------------------------------------------------------------------------------------------------------------------------------------------------------------------------------------|----|
| 2.7 | Composite Hovmöller diagram of equatorially (5°S - 5°N) averaged SST anomalies for El Niño events ($n=3$) which are most influenced by the MJO (a; 1997, 2006, and 2009) and El Niño events ($n=3$) which are least influenced by the MJO (b; 1991, 1994, and 2014). Units are $^{\circ}\text{C}$ | 26 |
| 3.1 | Schematic diagram of the MJO lifecycle as constructed from 20-100 day bandpass filtered composites of 850mb zonal wind anomalies and outgoing longwave radiation anomalies from SP-CCSM4. The lifecycle is divided into 8 phases (P1 through P8), and each phase has the number of days specified. | 31 |
| 3.2 | Composite of Niño 3 index vs time (blue) and APE_{mp} vs time (orange) for El Niño events in SP-CCSM4. | 32 |
| 3.3 | Composite of monthly average APE_{mp} vs W_{mp} trajectories for El Niño (red) and La Niña (blue) in SP-CCSM4 with two month smoothing applied. Solid lines indicate trajectories for the year leading up to an event, while dotted lines indicate trajectories for the year following the onset of the event. A heavy dot indicates January of the ENSO year, while an X marks December of the year following each event. | 32 |
| 3.4 | Composite of $W_{MJO,K}$ standard deviation spatial distribution for all El Niño events ($n=20$) in the SP-CCSM4 control run. | 34 |
| 3.5 | Scatter plot of the $W_{MJO,K}$ index averaged between January and July, normalized by the maximum value, prior to the peak of El Niño vs the DJF average Niño 3 index for the SP-CCSM4 control run. Superimposed is the linear regression of DJF average Niño 3 index on the normalized $W_{MJO,K}$ index. | 35 |
| 3.6 | Composited APE vs time for (a) $+N_{RMM}$ (solid blue), (a) $-N_{RMM}$ (dotted blue) (b) $+N_{MJO,K}$ (solid red), (b) $-N_{MJO,K}$ (dotted red), (c) $+N_{TCV}$ (solid green), and (c) $-N_{TCV}$ (dotted green). Units: Joules. | 38 |
| 3.7 | Composited W vs time for (a) $+N_{RMM}$ (solid blue), (a) $-N_{RMM}$ (dotted blue), (b) $+N_{MJO,K}$ (solid red), (b) $-N_{MJO,K}$ (dotted red), (c) $+N_{TCV}$ (solid green), and (c) $-N_{TCV}$ (dotted green). Units: Watts. | 39 |
| 3.8 | Scatter plot of mean perturbation wind power versus mean perturbation buoyancy power in SP-CCSM4, showing a clear, strong linear relationship. The regression line is superimposed. | 40 |
| 3.9 | Hovmöller diagrams of the composite Kelvin wave component of thermocline depth anomaly for each experiment. Units: meters. | 41 |

| | | |
|------|----------------------------------------------------------------------------------------------------------------------------------------------------------------------------------------------------------------------------------------------------------------------------------------------------------------------------------------------------------------------------------------------------------------------------------------------------------------------------------------------------------------------------------------------------------------------------------------------------------------------------------------------------------------------------------------------------------------------------------------|----|
| 3.10 | Composited Niño 3 index vs time for (a) $+N_{RMM}$ (solid blue), (a) $-N_{RMM}$ (dotted blue) (b) $+N_{MJO,K}$ (solid red), (b) $-N_{MJO,K}$ (dotted red), (c) $+N_{TCV}$ (solid green), and (c) $-N_{TCV}$ (dotted green). | 43 |
| 3.11 | As in Figure 3.9, but for monthly SST anomalies averaged between 5°S and 5°N . Units are $^{\circ}\text{C}$ | 43 |
| 3.12 | January-April average latent heat flux anomaly for $+N_{MJO,K}$ (a) and $-N_{MJO,K}$ (b), and mixed layer depth anomaly for $+N_{MJO,K}$ (c) and $-N_{MJO,K}$ (d). Units are $\text{W}\cdot\text{m}^{-2}$ and m , respectively. Negative (positive) values of LHF imply energy flux into (out of) the ocean. | 46 |
| 4.1 | Composite time series of the normalized $W_{MJO,K}$ index during January-July for $+N_{MJO,K}$ (red, left) and $-N_{MJO,K}$ (blue, right). The shading indicates $\pm 1\sigma$ for each composite of seven El Niño events. $+N_{MJO,K}$ ($-N_{MJO,K}$) events are chosen for high (low) variance during this period. | 51 |
| 4.2 | (a) Niño 3 index time series for SP-CCSM4 (black) and ZCocn forced by the SP-CCSM4 wind stress (red). The correlation between these time series is 0.804. Events which are strongly (weakly) influenced by MJO are marked by squares (circles). (b) Probability density function for Niño 3 index for SP-CCSM4 (black) and ZCocn forced by SP-CCSM4 wind stress (red). The mean of each is shown by the respective dashed lines (ZCocn shows a bias of 0.17°C). (c) Power spectra for SP-CCSM4 (black), ZCocn forced by SP-CCSM4 wind stress (red), and the red noise spectrum (blue dashed). | 55 |
| 4.3 | Ensemble average composite of equatorially ($5^{\circ}\text{S} - 5^{\circ}\text{N}$) averaged: a) - b) Kelvin wave component of thermocline depth anomaly and c) - d) total thermocline depth anomaly for strong (Sctl) and weak (Wctl) control cases. Positive (negative) values indicate downwelling (upwelling) Kelvin waves and an anomalously deep (shallow) thermocline. The thick contour is the zero isoline. Stippled regions indicate composite regions that are significantly significant at the 95% level using a two-tailed Student's t-test. The green lines indicate the time after which the flattened, El Niño-like thermocline has emerged and persists throughout the rest of the year. Units are meters. | 58 |

| | | |
|-----|---------------------------------------------------------------------------------------------------------------------------------------------------------------------------------------------------------------------------------------------------------------------------------------------------------------------------------------------------------------------------------------------------------------------------------------------------------------------------------------------------------------------------------------------------------------------------------------------------------------------------------------------------------------------------------------------------------------------------------------------------|----|
| 4.4 | Ensemble average composite of equatorially ($5^{\circ}\text{S} - 5^{\circ}\text{N}$) averaged: a) – b) zonal wind stress anomalies and c) – d) zonal MJO wind stress (τ_{MJO}) for strong (SCtl) and weak (WCtl) control cases. Positive (negative) values indicate westerly (easterly) wind stress anomalies. The thick contour is the zero isoline. Stippled regions of total wind stress anomaly indicate composite regions that are statistically significant at the 95% level using a two-tailed Student’s t-test. The green horizontal lines correspond to those on Figure 4.3, after which the flattened, El Niño-like thermocline has emerged and persists throughout the rest of the year. Units are $N \cdot m^{-2}$ | 59 |
| 4.5 | Ensemble average composite of equatorially ($5^{\circ}\text{S} - 5^{\circ}\text{N}$) averaged SST anomaly for SCtl (top) and WCtl (bottom). The thick contour is the 0°C isotherm. Stippled regions indicate composite regions that are statistically significant at the 95% level using a two-tailed Student’s t-test. The boxes indicate the timing and longitude of maximum SST. Units are $^{\circ}\text{C}$ | 62 |
| 4.6 | Ensemble average composite of the Niño 3 index time series difference between each sensitivity experiment and their respective control experiment. Each set of five bars represents a monthly value for each experiment, with the blue bar as the leftmost value for each month. The shaded areas show $\pm 1\sigma$ computed across events and ensemble members. | 66 |
| 4.7 | As with Figure 4.6, but for wind power. | 68 |
| 4.8 | Ensemble average composite difference in Kelvin wave component of thermocline depth anomaly between each experiment and the control. The thick contour is the zero isoline and the vertical dash lines delineate the longitudes of the $W_{MJO,K}$ region. Stippled regions indicate composite regions that are statistically significant at the 95% level using a two-tailed Student’s t-test. Units are meters. | 69 |
| 4.9 | April – May – June lag correlation between zonal MJO wind stress in the $W_{MJO,K}$ region and Kelvin wave component of thermocline depth anomaly averaged between 5°S and 5°N for SCtl (top) and WCtl (bottom). The white bar indicates the $W_{MJO,K}$ region at zero lag, the region for which the correlation is computed. Negative (positive) lags indicate Kelvin wave activity leading (lagging) MJO wind stress. Stippling indicates correlation significance at the 95% level. | 72 |

| | | |
|-----|------------------------------------------------------------------------------------------------------------------------------------------------------------------------------------------------------------------------------------------------------------------------------------------------------------------------------------------------------------------------------------------------------------------------------------------------------------------------------------------------------------------------------------------------------------------------------------------------------------------------------------------------------------------|----|
| 5.1 | Amplitudes of EOFs resultant from HSVD analysis performed on observed intraseasonally bandpass filtered wind stress anomalies. Units are $N \cdot m^{-2}$. | 77 |
| 5.2 | Hovmöller diagrams of correlation coefficients between actual $W_{MJO,K}$ and the proxy $W_{MJO,K}$. This correlation is computed for each year independently, for the full year (a) and for only the AMJ season (b). | 78 |
| 5.3 | Multivariate EOF patterns of equatorially averaged ($5^{\circ}S - 5^{\circ}N$) $W_{MJO,K}$ (red) and SST anomalies (blue) in the tropical Pacific. Collectively, EOF1 (solid lines) explains 30.8% of the total daily variability and EOF2 (dotted lines) explains 21.1% of the total daily variability. Included in the legend is the fraction of each EOF explained by each variable. | 80 |
| 5.4 | Normalized daily time series of PC1 (red) and PC2 (blue) from multivariate EOF analysis on equatorially ($5^{\circ}S - 5^{\circ}N$) averaged $W_{MJO,K}$ and daily SST anomalies. PC2 has been smoothed by a 30-day running mean filter. Monthly values of Niño 3.4 (black) are also shown to indicate that PC1 captures much of that variability. El Niño events throughout the time series are indicated by the background shading. Events which are strongly influenced by MJO by the criteria described in Chapter 3 are shaded in red (1997, 2006, and 2009), while the other El Niño events (1991, 1994, 2002, 2004, 2014, and 2015) are shaded in gray. | 81 |
| 5.5 | Time series of the $MaKE$ (red) and $MaKI$ (blue) indices in observations. El Niño years are highlighted by the background shading, with events that are strongly influenced by El Niño highlighted in red and all other events highlighted in gray. The -0.5σ (-2σ) threshold value for $MaKE$ ($MaKI$) is shown by the horizontal thin red (blue) line. For each El Niño year, the month of April is indicated by the vertical dash-dotted red line because that is the month identified as having predictive power for these indices. | 83 |

| | | |
|-----|---------------------------------------------------------------------------------------------------------------------------------------------------------------------------------------------------------------------------------------------------------------------------------------------------------------------------------------------------------------------------------------------------------------------------------------------------------------------------------------------------------------------------------------------------------------------------------------------------------------------------------------------------------------------------------------------------------------------------------------------------------------------------------------------------------------------------------------------------------------------------------------------------------------------------------------------------------------------------------------------------------------------------------------------------------------------------------------------------------------------------------------------------------------------------------------------------------------------------------------------------------------|----|
| 5.6 | Composites of AMJ lag correlation between MJO wind stress in the $W_{MJO,K}$ region and equatorially ($5^{\circ}\text{S} - 5^{\circ}\text{N}$) averaged Kelvin wave depth, defined as the meridional structure of a Kelvin wave projected onto daily anomalies of the 20°C isotherm. The sign convection is such that a downwelling Kelvin wave (positive thermocline anomaly) would be correlated with a westerly MJO wind stress anomaly. Each composite includes only years which meet the <i>MaKE</i> threshold. Shown are composites of (a) all years which also meet the <i>MaKI</i> index threshold (1992, 1997, 2001, 2006, 2009, 2014, and 2016; $n=7$), (b) El Niño years which meet the <i>MaKI</i> threshold (1997, 2006, 2009, and 2014; $n=4$), (c) all years which do not meet the <i>MaKI</i> threshold (1990, 1991, 1993, 1994, 1995, 2002, 2004, 2005, 2012, and 2015; $n=10$), (d) and El Niño years which do not meet the <i>MaKI</i> threshold (1991, 1994, 2002, 2004, and 2015; $n=5$). The zonal extent of the $W_{MJO,K}$ region is blacked out. Positive (negative) lags indicate MJO wind stress leading (lagging) Kelvin wave depth. Stippling indicates statistical significance at the 95% level. | 88 |
| 5.7 | Receiver operating characteristic (ROC) plots for each ensemble member of the CFS-v2 reforecasts. ROC plots compare the true positive rate and false positive rate, with any points above the center line outperforming chance. Note that the distance between each point and the center line for <i>MaKE</i> (blue) is considerably larger than for Niño 3.4 (red). The numbered labels indicate the ensemble members represented by each point. | 92 |
| 5.8 | Hovmöller diagram of equatorially averaged ($5^{\circ}\text{S} - 5^{\circ}\text{N}$) zonal (a) MJO wind stress, (b) total wind stress daily anomaly, and (c) SST anomaly. Units of wind stress are $N \cdot m^{-2}$, and units of SST anomaly are $^{\circ}\text{C}$ | 94 |

Abstract

THE EFFECT OF THE MADDEN-JULIAN OSCILLATION ON THE ENERGETICS
AND PREDICTION OF EL NIÑO-SOUTHERN OSCILLATION

Nicholas D. Lybarger, PhD

George Mason University, 2019

Dissertation Director: Dr. Cristiana Stan

Previous studies have documented extensive interactions between the El Niño-Southern Oscillation (ENSO) and the Madden-Julian Oscillation (MJO). These studies have primarily focused on interactions during individual El Niño events, and a comprehensive quantitative framework which captures the mechanisms responsible for the interactions between these sources of variability has yet to be specified. Expanding upon the known relationship between wind power and available potential energy with respect to El Niño, this study exploits the known relationship between MJO wind forcing and Kelvin wave activity to develop such a framework. A statistically significant relationship between MJO influence and Kelvin wave activity from January to July and the ultimate strength of the resultant El Niño event is found, both in an observational dataset and global climate model output. Associated with these stronger events are stronger wind power, available potential energy, and Kelvin wave development. This coupled atmosphere-ocean index of MJO influence is shown to differentiate between composite events more strongly than the purely atmospheric index of MJO strength and a purely oceanic index of thermocline variability. Sensitivity experiments performed on El Niño events which are influenced by the MJO and on those which are not demonstrate that a necessary condition for MJO-ENSO interactions is a

coherent phasing between those phenomena. However, these experiments also show that although MJO can have significant influence on the timing and strength of El Niño, it is not the triggering mechanism of these events. Holistic indices which capture covariability between MJO winds, Kelvin wave activity, and SST anomalies are then shown to have prediction skill with respect to ENSO. Specifically, these indices strongly outperform Niño 3.4 as an ENSO predictor when applied to CFS-v2 hindcasts of 1980-2014.

Chapter 1: Introduction

1.1 ENSO Theories

El Niño – Southern Oscillation (ENSO) is the primary mode of interannual variability in the tropical Pacific Ocean with a 3 – 5 year period (e.g. Fedorov and Philander, 2001; Neelin et al., 1998; Wang et al., 2011). Although ENSO is understood to be a recurring climate pattern resulting from ocean-atmosphere interactions, the importance of atmospheric forcing to the evolution of the system has been debated and three paradigms have emerged: *i*) ENSO is an unstable chaotic oscillation in which internal atmospheric dynamics are neglected or considered secondary to internal ocean dynamics (e.g. Chang et al., 1994; Jin et al., 1994; Munnich et al., 1991; Tziperman et al., 1995; Wang et al., 1999; Zebiak, 1989; Zebiak and Cane, 1987), *ii*) ENSO is a self-sustained and periodic oscillatory mode for which atmospheric forcing provides the observed irregularity and aperiodicity (Battisti, 1988; Jin, 1997; Kirtman, 1997; Neelin et al., 1998; Suarez and Schopf, 1988), and *iii*) ENSO is a damped process for which atmospheric forcing provides the trigger for each discrete event (Lau, 1985; Flugel and Chang, 1996; Flugel et al., 2004; Kleeman and Moore, 1997; Moore and Kleeman, 1999a,b, 1996; Penland and Matrosova, 1994; Penland and Sardeshmukh, 1995; Thompson and Battisti, 2000). Of those studies in the latter two paradigms, many have focused on synoptic scale westerly wind bursts and the intraseasonal Madden-Julian Oscillation (MJO Madden and Julian, 1972) as sources of forcing which influence the evolution of the oceanic state. In the framework of ENSO as a self-sustained oscillatory mode, sea surface temperature (SST) anomalies in the equatorial eastern Pacific respond to the zonal wind stress anomalies in the equatorial central Pacific and equatorial western Pacific through positive and negative feedbacks and the off-equatorial thermocline anomalies in the western Pacific are related to the zonal wind stress anomalies in the

equatorial central Pacific (Wang, 2001). The adjustment of SST and thermocline to the wind stress forcing can occur through ocean wave dynamics (Neelin, 1991). In the damped mode paradigm, slow modes (coupled or SST) resulting from air-sea interactions in the tropical Pacific Ocean interact constructively and are amplified by synoptic-intraseasonal variability (Moore and Kleeman, 1999a).

1.1.1 Bjerknes Hypothesis

Regardless of the underlying theory, what is clear is that the positive feedback loop proposed by Bjerknes (1969) plays an important role in ENSO evolution. This feedback loop begins with a positive SST anomaly in the eastern tropical Pacific Ocean. This anomaly reduces the zonal temperature gradient that exists in the mean state between the eastern and western Pacific. This introduces anomalous rising atmospheric motion in the eastern Pacific and westerly anomalies in the mean state trade winds, inhibiting the Walker circulation. The westerly anomalies lead to a reduction of the mean equatorial upwelling, thus reinforcing the original positive SST anomaly in the eastern Pacific and completing the feedback loop. Bjerknes proposed no mechanism for escaping this loop, and thus this theory explains only how a preexisting anomaly might grow into a fully-fledged event. The following subsections will provide a brief review of oscillatory mechanisms for ENSO growth and decay.

1.1.2 Delayed Oscillator

Suarez and Schopf (1988) introduced the conceptual model of the delayed oscillator mechanism explaining the decay of El Niño. In this model, Bjerknes feedback causes the development of an El Niño event, with warm SST anomalies in the eastern Pacific. This generates free oceanic Rossby waves which propagate westward until they meet the western boundary, where they reflect as upwelling Kelvin waves, which reverse the positive SST anomaly when they arrive in the eastern Pacific. This model assumes that the eastern Pacific is the relevant region for air-sea coupling, and that wave reflection off the eastern boundary is negligible (Wang et al., 2017).

1.1.3 Recharge Oscillator

The concept of the recharge oscillator was introduced by Wyrтки (1975, 1985) and later modeled by Jin (1997) using a modified form of the coupled model of Zebiak and Cane (1987). During the leadup to El Niño, oceanic heat content and warm water volume accumulates over the entire Pacific basin. During the peak of El Niño, Bjerknes feedback induces westerly anomalies in the central Pacific which cause a divergence of Sverdrup transport at the equator, thus expelling warm water from the tropics and leading to a reduction of equatorial oceanic heat content. This leads to a Pacific Ocean state wherein the basin-wide thermocline is anomalously shallow. The mean state climatological upwelling is then able to pump cooler water to the surface, thus producing La Niña. Cooler water at the surface strengthens the Walker circulation, enhances the trade winds, and leads to convergence of Sverdrup transport to the equator, resulting in a buildup of oceanic heat content and warm water volume (Wang et al., 2017). A schematic diagram of this conceptual model is shown in Figure 1.1.

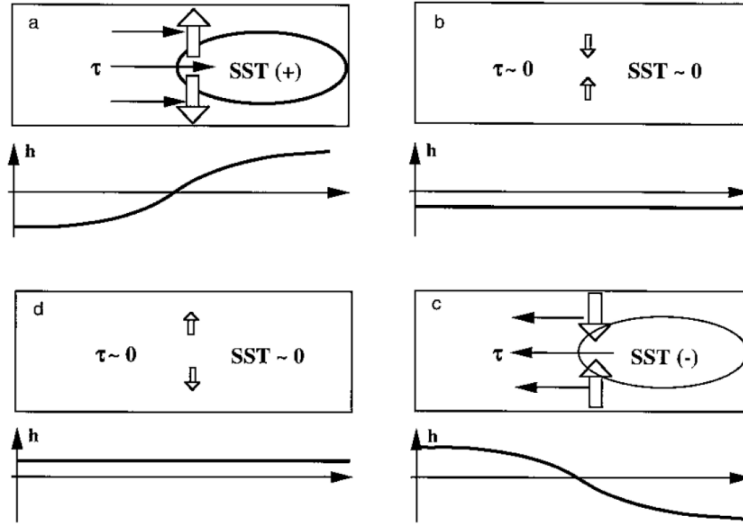


Figure 1.1: Schematic diagram of the recharge-discharge oscillator conceptual model. Beginning with the warm phase (a), where positive SST anomalies in the eastern Pacific associated with westerly wind anomalies and a shallow thermocline drives Sverdrup divergence carrying heat away from the basin. This results in (b), the discharged ocean state, with basin-wide deep thermocline anomalies, leading to the development of (c), with a negative SST anomaly associated with easterly wind anomalies and Sverdrup transport of heat onto the equator, recharging the ocean. This induces to a basin wide shallow thermocline, leading to the development of a positive thermocline anomaly, thus resetting the cycle. The rectangular box represents the Pacific basin, and the plots of h represent thermocline depths anomalies across the basin. Reprinted from Jin (1997).

1.1.4 Western Pacific Oscillator

The western Pacific oscillator conceptual model (Weisberg and Wang, 1997; Wang et al., 1999) addresses the western Pacific influence on ENSO, which had been neglected in the delayed oscillator theory (Suarez and Schopf, 1988). On the basis of a Gill-type atmospheric response to convection (Gill, 1980), heating of the atmosphere due to condensation associated with convective activity creates off-equatorial cyclones which result in westerly anomalies along the equator at the surface. These westerly anomalies deepen the eastern Pacific thermocline, producing positive SST anomalies there and initiating Bjerknes feedback. At the same time, these off-equatorial cyclones in the central Pacific create local shallow thermocline anomalies via Ekman pumping which spread to the western Pacific, inducing off-equatorial negative SST anomalies and positive sea level pressure (SLP) anomalies in that region. These negative SST and positive SLP anomalies are then associated with the production of off-equatorial anticyclonic activity in the western Pacific, which induce equatorial easterly anomalies, enhancing upwelling and divergent Sverdrup transport at the surface, cooling the equatorial SST anomaly and thus providing the negative feedback for termination of the warm phase and the growth of the cool phase (Wang et al., 2017). A schematic diagram of this conceptual model is shown in Figure 1.2.

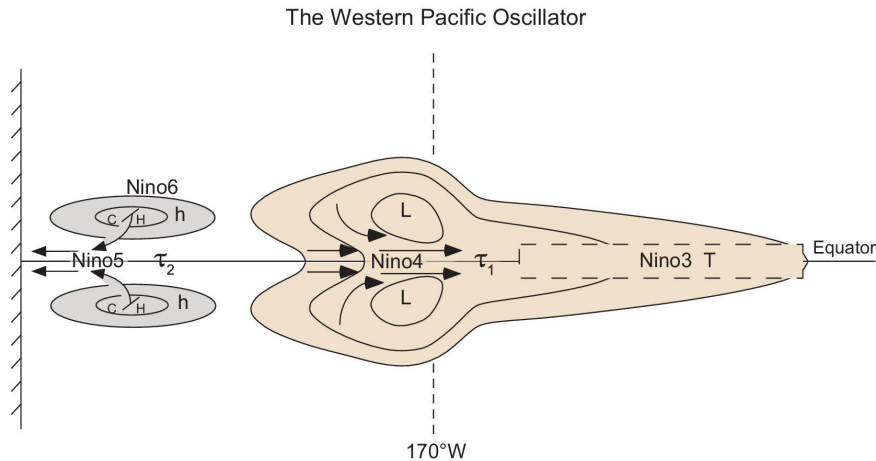


Figure 1.2: Schematic diagram of the western Pacific oscillator. L, C and H represent low SLP, cold SST and high SLP, respectively. τ_1 and τ_2 stand for zonal wind-stress anomalies in the Niño 4 and Niño 5 regions, respectively. T is the SST anomaly in the Niño 3 region and h is the thermocline-depth anomaly in the Niño 6 region. Reprinted from Wang, Chunzai, “A review of ENSO theories”, *National Science Review*, 2018, **5**, by permission of Oxford University Press.

1.1.5 Advective - Reflective Oscillator

Picaut et al. (2002) introduced the advective-reflective oscillator model, wherein the zonal advection of warm pool water by anomalous eastward currents during El Niño is emphasized. During the development of El Niño, heating and westerly wind anomalies in the central Pacific produce off-equatorial upwelling oceanic Rossby waves which propagate westward and downwelling oceanic Kelvin waves which propagate eastward. The Rossby waves reach the western boundary and reflect as upwelling Kelvin waves, while the downwelling Kelvin waves reach the eastern boundary and reflect as downwelling Rossby waves. Both downwelling Rossby waves and upwelling Kelvin waves are associated with westward equatorial currents which counteract the eastward advection of the warm pool, allowing the system to rebound to the cool ENSO phase (Wang et al., 2017).

1.1.6 Unified Oscillator

Wang (2001) combined the physics of these various self-sustaining model into a single framework dubbed the “unified oscillator”, at the same time showing that each of the previously described conceptual models is a special case of the unified oscillator. This framework frees specific mechanistic effects to be time dependent, thus allowing for the possibility that the relative importance of each mechanism can vary from event to event.

1.1.7 Stable Mode Triggered by Stochastic Forcing

Beyond these self-sustaining oscillatory models lies a theoretical framework in which an El Niño event is discrete, a warm extreme on a background of neutral or cold Pacific Ocean conditions which is driven by stochastic forcing external to the coupled Pacific system (Lau, 1985; Flugel and Chang, 1996; Flugel et al., 2004; Kleeman and Moore, 1997; Moore and Kleeman, 1999a,b, 1996; Penland and Matrosova, 1994; Penland and Sardeshmukh, 1995; Thompson and Battisti, 2000). Unlike the self-sustained models, this framework allows for a natural explanation for El Niño variability and prediction difficulty due to the necessary inclusion of external and/or unresolved noise. This noise may take the form of atmospheric phenomena like the MJO and westerly wind bursts, or oceanic phenomena like tropical instability waves. Regardless of the initial triggering mechanism, the physics of the negative feedbacks described in the framework of the discussed conceptual models should still be valid for the termination of an event, even if the event is discrete and triggered by noise processes (Wang et al., 2017).

1.2 MJO-ENSO Interactions

MJO is the dominant signal of intraseasonal variability in the tropics, and is characterized by anomalous convection and zonal winds that originate in the Indian Ocean and propagate eastward across the Maritime Continent into the tropical Pacific (Hendon and Salby, 1994; Zhang, 2005). In the literature, it is often defined in terms of eight phases, categorizing

various features, including SLP, convective activity, and the zonal circulation as it propagates around the equator. Figure 1.3 shows a schematic diagram of each phase as defined in Madden and Julian (1972). The convective envelope itself is associated with wind convergence at the surface, reduced SLP, and reduced outgoing longwave radiation (OLR), and it is preceded by suppressed convection, divergent winds at the surface, and heightened SLP, and thus represents an oscillation of these features. As the convective envelope moves eastward, it leaves in its wake another phase of suppressed convection. As should be expected due to the effect of MJO phase on the SLP, the MJO can affect oceanic Kelvin waves in the western tropical Pacific before they propagate to the eastern Pacific (Enfield, 1987; Hendon et al., 1998; Zhang, 2001). Indeed, coherence between the MJO winds and thermocline variability is sometimes seen during El Niño events (Kessler et al., 1995; Zhang and Gottschalck, 2002).

The power spectrum of oceanic Kelvin waves is characterized by a spectral peak centered at 70-90 days (DeMott et al., 2015) and at 120 days (Cravatte et al., 2003). This peak differs slightly from the spectral peak of the MJO, which is around 30-70 days (DeMott et al., 2015). Hendon et al. (1998) argues that the difference in spectral peak between these processes is due to the fact that Kelvin waves do not respond to higher frequency activity, and the Kelvin wave response is due to the lower frequency tail of the MJO. Roundy and Kiladis (2006) used data from the Tropical Atmosphere Ocean (TAO) mooring array (Hayes et al., 1991) to show that there is a decrease in Kelvin wave phase speeds as the ocean tends toward El Niño, thus delaying the arrival of Kelvin waves to the eastern Pacific and reducing their frequency as the state of the ocean approaches the peak of the event. Their study found that the eastward propagation speed of the effective wind forcing is often reduced during El Niño, resulting in enhancement of the wave amplification process. This reduction is less likely to occur with upwelling Kelvin waves than with downwelling Kelvin waves, which helps explain the finding of Seiki et al. (2009) that the ocean state is more sensitive to westerly wind forcing than easterly wind forcing in the year preceding El Niño. Batstone and Hendon (2005) used National Centers for Environmental Prediction–National Center for Atmospheric Research (NCEP–NCAR) reanalyses (Kalnay et al., 1996) to show

that MJO activity over the central Pacific is responsible for half of the uncoupled wind variability (i.e. the residual wind variability once variability correlated with SST at zero lag has been regressed out) in the leadup to El Niño, but accounts for more than two-thirds of the thermocline perturbation. This finding supports the notion that spatially and temporally coherent signals (such as the MJO) may be able to affect the large scale state of the ocean more strongly than less coherent forcing (Hendon et al., 2007; Kessler et al., 1995; Zhang and Gottschalck, 2002). Marshall et al. (2009) found that strong El Niño events are associated with larger numbers of MJO events, with little difference seen between the magnitude of MJO events associated with strong and weak El Niño events.

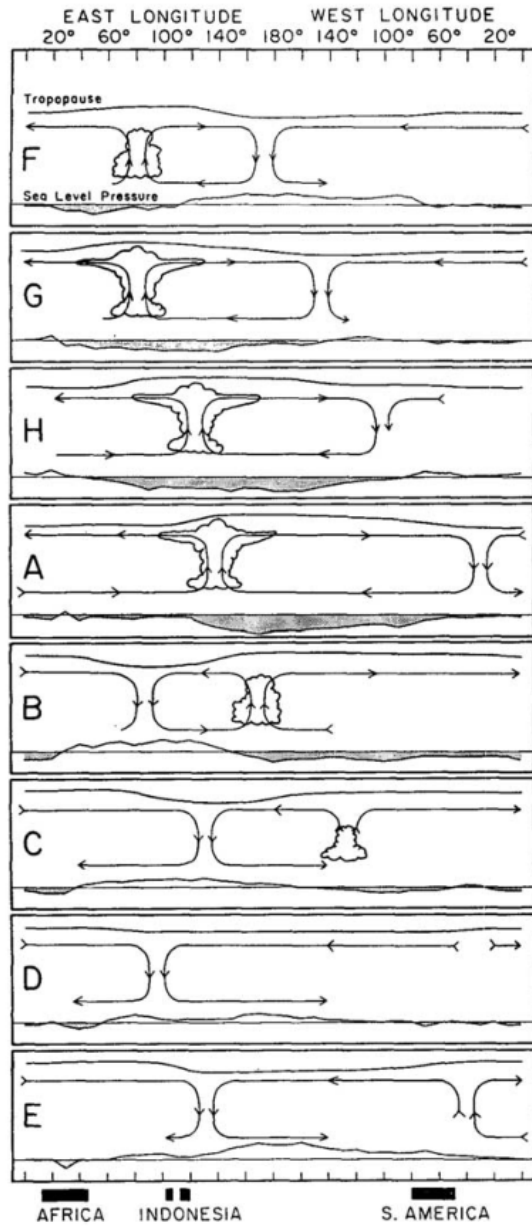


Figure 1.3: Schematic diagram of the MJO lifecycle (from top to bottom). Arrows represent circulation anomalies. Clouds represent condensation due to convective activity. Above each phase is a curve representing perturbations to the upper tropospheric pressure, while below each phase is a curve representing perturbations to the sea level pressure. Reprinted from Madden and Julian (1972).

1.2.1 Case Studies

As demonstrative examples of the wide variety of MJO/ENSO interactions, several particular El Niño events can be considered. The 1997/98 El Niño, which had a strong amplitude, was led by two strong MJO events in the spring of 1997, leading forecast models to predict a far stronger El Niño than they had been before those events (McPhaden and Yu, 1999; Moore and Kleeman, 1999a; Kessler and Kleeman, 2000; Bergman et al., 2001; Boulanger et al., 2004). Figure 1.4 demonstrates the close correspondence between SST, zonal wind, and thermocline anomalies during this event. Particularly striking is the nearly simultaneous eastward propagation of each field throughout 1997, calling attention to the relationship between these fields and MJO activity. However, leading up to the very strong though more slowly developing 1982/1983 event, only weak/moderate MJO activity was observed (Tang and Yu, 2008). Strong MJO activity was observed in the winter and spring of 1989/1990 which ultimately resulted in an aborted El Niño event later that year, indicating that the MJO may influence the timing and strength of El Niño events, but is not responsible for the events themselves (McPhaden and Yu, 1999; Bergman et al., 2001). In 2014, springtime anomalous westerlies in the western Pacific forced substantial Kelvin waves to the eastern Pacific, leading many modeling agencies to predict a strong El Niño that year (Menkes et al., 2014; Chiodi and Harrison, 2017). However, only a modest El Niño event emerged that year, perhaps due to off equatorial cool sea surface temperature anomalies that were not accurately modeled (Zhu et al., 2016) and an unusually strong easterly wind burst in June which inhibited Bjerknes feedback (Hu and Fedorov, 2016; Levine and McPhaden, 2016; Menkes et al., 2014).

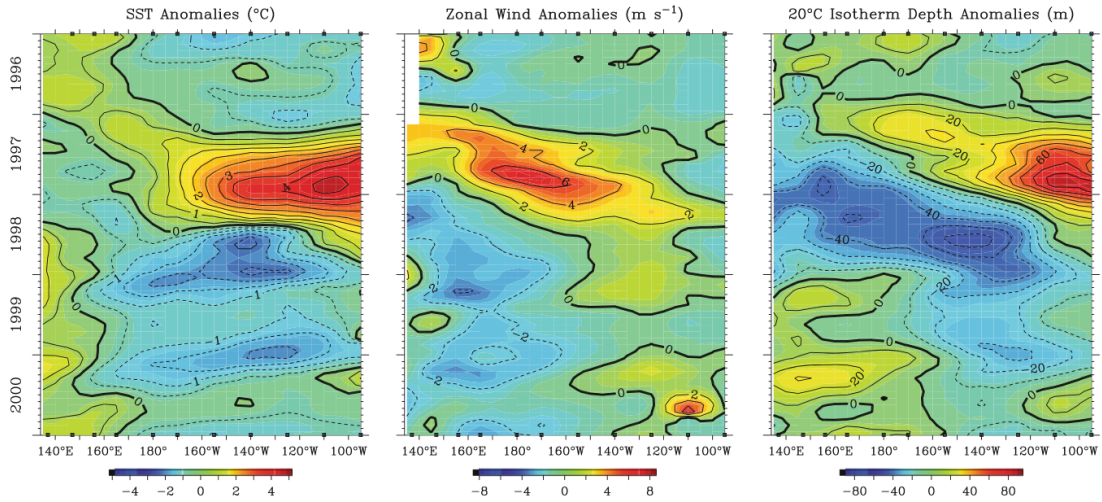


Figure 1.4: Hovmöller diagram showing the evolution of monthly SST anomalies (a), zonal wind anomalies (b), and thermocline depth anomalies (c) averaged from $2^{\circ}\text{S} - 2^{\circ}\text{N}$ over the period January 1996 to December 2000. Data provided by the TAO/TRITON array (Hayes et al., 1991; McPhaden, 1995). Reprinted by permission from Springer Nature Customer Service Center GmbH: Springer Nature, Coral Reefs of the World, vol 8. by Wang C., Deser C., Yu JY., DiNezio P., and Clement A., 2017.

1.3 Objectives

Various features of MJO-ENSO interactions have been studied since the discovery of the MJO, but a quantitative definition of where, when, and how the MJO affects ENSO variability has yet to be specified. Chapter 2 introduces a way to quantify the effect of the MJO on El Niño via its association with surface wind anomalies, ocean surface current anomalies, and Kelvin wave activity. These analyses are applied to observations and several interesting results emerge. However, because of the short observational satellite record, modeling studies are required for more robust results. Chapter 3 applies those same analyses to a 100-year run of a global climate model (GCM), thus providing more statistical evidence for the effect of the MJO on El Niño evolution as quantified here. Chapter 4 then applies modified MJO wind stress forcing and modified Kelvin wave forcing to the coupled model of Zebiak and Cane (1987) to provide evidence of the underlying mechanism tying

together MJO and ENSO variability. That chapter shows that a significant source of this covariability is coherent phasing between the MJO wind stress and Kelvin wave activity in the leadup to El Niño. Chapter 5 creates holistic indices of MJO-ENSO covariability for real-time applications, incorporating the effect of MJO-associated anomalies on SST variability. These indices are shown to have value in predicting ENSO variability.

Chapter 2: MJO-Kelvin Wave Energetics in Observations

2.1 ENSO Energetics Framework

Goddard and Philander (2000) developed a theoretical framework for understanding and diagnosing the energetics balance in the tropical Pacific Ocean as it relates to ENSO. Wind power (W), defined as the covarying winds and ocean currents at the surface of the ocean, generate buoyancy power, forcing vertical deviations in the three dimensional ocean current. These vertical flows generate thermocline variability, quantified by the available potential energy (APE). The following two equations (Hu et al., 2014) introduce the key variables in the energetics balance on interannual timescales, W and APE.

$$W = \iint \mathbf{u} \cdot \boldsymbol{\tau} dA \quad (2.1)$$

$$APE = \iiint \frac{\tilde{\rho}^2}{2S^2} dV \quad (2.2)$$

Here, \mathbf{u} represents horizontal currents at the ocean surface, $\boldsymbol{\tau}$ represents the horizontal wind stress supplied by surface winds to the ocean surface, A is defined as the surface of the Pacific basin (15°S - 15°N, 130°E - 85°W), and V is the volume of the Pacific basin from the surface to a depth of 400m. The potential density, $\tilde{\rho}$ is calculated from temperature and salinity using the equation of state for seawater and then removing the horizontal and time mean density (ρ^*). Finally, $S^2 = -(1/g)d\rho^*/dz$, accounting for gravitational stability. Equations 2.1 and 2.2 can be further decomposed by linearizing \mathbf{u} , $\boldsymbol{\tau}$, and $\tilde{\rho}$ about the mean state, giving $\mathbf{u} = \bar{\mathbf{u}} + \mathbf{u}'$, $\boldsymbol{\tau} = \bar{\boldsymbol{\tau}} + \boldsymbol{\tau}'$, and $\tilde{\rho} = \bar{\tilde{\rho}} + \tilde{\rho}'$, where the overbar denotes monthly climatology and primes represent monthly anomalies. Subbing these decomposed terms back into Equations

2.1 and 2.2 gives $W = W_{mm} + W_{mp} + W_{pp}$ and $APE_{mm} + APE_{mp} + APE_{pp}$, where the subscript mm represents the product of the mean terms, the subscript mp represents the product of the mean and perturbation terms, and the subscript pp represents the product of the perturbation terms. On interannual time scales, the mean-perturbation terms have been shown to dominate (Goddard and Philander, 2000; Hu et al., 2014).

2.2 Derivation of Terms

To isolate the effects of the MJO and oceanic Kelvin waves, and thus to capture variability associated with one of the primary mechanisms by which the MJO has been shown to affect the ocean (e.g. Enfield, 1987; Hendon et al., 1998; Zhang, 2001; Kessler et al., 1995; Zhang and Gottschalck, 2002), the surface current and wind stress perturbations in Equation 2.1 are further decomposed as

$$\mathbf{u}' = \mathbf{u}_K + \mathbf{u}_{residual} \text{ and } \boldsymbol{\tau}' = \boldsymbol{\tau}_{MJO} + \boldsymbol{\tau}_{residual} \quad (2.3)$$

where \mathbf{u}_K is the horizontal surface current associated with equatorial oceanic Kelvin waves and \mathbf{u}_{noise} is the component of the current not associated with equatorial Kelvin waves. $\boldsymbol{\tau}_{MJO}$ represents the surface wind stress due to MJO forcing and $\boldsymbol{\tau}_{noise}$ denotes the surface wind stress due to processes unrelated to MJO, is the focus of this chapter. These noise terms contribute the majority of the variability in the anomalies, but the MJO and Kelvin wave components of these terms represent spatially and temporally coherent signals, which may be more able to affect the large scale state of the ocean (Hendon et al., 2007; Kessler et al., 1995; Zhang and Gottschalck, 2002), as discussed in Section 1.2.

The MJO component of the wind stress anomaly has been calculated following the method of Zhang and Gottschalck (2002). First, a 30-90 day bandpass filter is applied to the daily wind stress anomalies to isolate the intraseasonal variability. Then, the filtered anomaly is decomposed into leading principal components (PCs) via Hilbert singular value decomposition analysis (a regular SVD analysis for a field and its Hilbert transform), which

isolates the dominant oscillatory modes in the intraseasonal wind stress anomalies. The first two leading pairs of PCs are retained, and these PCs are projected onto the intraseasonal wind stress anomalies, yielding a time series of MJO wind stress for each gridpoint ($\boldsymbol{\tau}_{MJO}$). The Kelvin wave component of the ocean current is isolated by multiplying the horizontal current by the meridional structure of a Kelvin wave (Kirtman, 1997). Using the decomposition in Equation 2.3, $\mathbf{u} \cdot \boldsymbol{\tau}$ can be represented for daily anomalies as:

$$\begin{aligned} \mathbf{u} \cdot \boldsymbol{\tau} = & \bar{\mathbf{u}} \cdot \bar{\boldsymbol{\tau}} + \bar{\mathbf{u}} \cdot \boldsymbol{\tau}_{MJO} + \mathbf{u}_K \cdot \bar{\boldsymbol{\tau}} + \mathbf{u}_K \cdot \boldsymbol{\tau}_{MJO} + \\ & \bar{\mathbf{u}} \cdot \boldsymbol{\tau}_{residual} + \mathbf{u}_K \cdot \boldsymbol{\tau}_{residual} + \mathbf{u}_{residual} \cdot \bar{\boldsymbol{\tau}} + \mathbf{u}_{residual} \cdot \boldsymbol{\tau}_{MJO} + \mathbf{u}_{residual} \cdot \boldsymbol{\tau}_{residual} \end{aligned} \quad (2.4)$$

In further discussions, the mean wind power term, $\bar{\mathbf{u}} \cdot \bar{\boldsymbol{\tau}}$, will be neglected, as it describes only the climatological mean state of the coupled system, and is therefore not relevant in discussing the differences between El Niño events (Hu et al., 2014). Although the residual terms constitute a significant part of the variability of W and span many timescales, this study is focused on MJO-Kelvin wave interactions, and thus the residuals are not relevant when discussing these mechanisms. Integrating over the Pacific basin and neglecting the residual terms, the wind power in Equation 2.1 becomes

$$W = W_{MJO} + W_K + W_{MJO,K} \quad (2.5)$$

where $W_{MJO} = \iint \bar{\mathbf{u}} \cdot \boldsymbol{\tau}_{MJO} dA$, $W_K = \iint \mathbf{u}_K \cdot \bar{\boldsymbol{\tau}} dA$, and $W_{MJO,K} = \iint \mathbf{u}_K \cdot \boldsymbol{\tau}_{MJO} dA$. These terms collectively explain about 15% of the daily variability in the total wind power.

The primary focus of this work is the $W_{MJO,K}$ term, describing the covariance between wind stress anomalies associated with the MJO and ocean current anomalies associated with oceanic Kelvin waves. This term is thus a measure of the MJO forcing on oceanic Kelvin wave activity. This term was chosen as the focus of this study due to the clarity

with which potentially predictable processes can be associated with it. It is therefore the hope that if a relationship between $W_{MJO,K}$ and ENSO can be established, it will shed light on the mechanisms responsible for that relationship, which would not necessarily be the case for W_{MJO} and W_K . Furthermore, additional analysis (not shown) with the terms W_{MJO} and W_K indicate that there is little to distinguish events with high and low values of these terms, and it is in fact the term which captures both MJO activity and Kelvin wave activity simultaneously ($W_{MJO,K}$) that produces the greatest contrast between composite events.

2.3 Observational Datasets

Due to the need for long term daily observations in order to capture MJO variability during as many El Niño events as possible, two wind stress datasets are used here. The Blended Sea Winds wind stress product from NOAA – NCEI (QSCAT) contains high-resolution ($0.25^\circ \times 0.25^\circ$) daily scatterometer data from multiple satellite sources at daily time scales covering July 9, 1987 to September 30, 2011 (Zhang et al., 2006b,a; Peng et al., 2013). Daily-averaged, high resolution ($0.25^\circ \times 0.25^\circ$) wind stress fields (DASCAT) estimated from ASCAT retrievals are obtained from the Centre de Recherche et d’Exploitation Satellitaire (CERSAT), at IFREMER, Plouzané (France) (Bentamy and Fillon, 2012). This dataset covers the period from March 21, 2007 to the present, but for this analysis, only the period until December 31, 2016 is used. For the overlapping period of March 21, 2007 to September 30, 2011, the gridded linear average of the two datasets is used instead. Because QSCAT comes from multiple sources and is further supplemented by NCEP Reanalysis 2 (Kanamitsu et al., 2002) to fill in missing data, there are no coverage problems related to sparse satellite swaths. However, DASCAT comes from a single source, and therefore does suffer these problems. To counteract this, DASCAT is supplemented by QSCAT in the overlapping period, and is interpolated in time to cover missing periods thereafter. There is rarely a period of more than a few days interpolated in this way. Furthermore, there are

some unrealistically extreme wind stress data during certain conditions which had to be eliminated.

Ocean observations are also required for this analysis. Unfortunately, long term, high temporal resolution ocean current and sea surface temperature observations are difficult to obtain, so a reanalysis dataset will be used as a proxy for observations. The Global Ocean Data Assimilation System (GODAS) (Nishida et al., 2011; Saha et al., 2006) covers the period 1979 – present, but only 1988 – 2016 will be used, due to the limitations imposed by the availability of the wind stress fields discussed above. GODAS has pentad temporal resolution and a spatial resolution of $1^\circ \times 1^\circ$. Analysis done over the overlapping periods show general agreement between surface stress fields from GODAS and the scatterometer data (not shown), and thus GODAS is determined to be reasonable approximation of observations, as suggested by Nishida et al. (2011), who validated GODAS fields and found them to be appropriate for oceanographic studies, excepting the salinity data, which is not used for this analysis. GODAS is interpolated from pentad to daily resolution. DASCAT and QSCAT is interpolated in space to match the $1^\circ \times 1^\circ$ resolution of GODAS. DASCAT, QSCAT, and GODAS data will hereafter be referred to by the catch-all term “observations”.

2.4 Application of MJO-Kelvin Energetics to Observations

For comparison with Goddard and Philander (2000), composites of W_{mp} vs APE_{mp} for El Niño and La Niña events are shown in Figure 2.1. The general nature of these trajectories are consistent with their findings, but in the El Niño composite (red), the decreasing APE is associated with small but generally positive values of W_{mp} , in contrast with their finding that negative wind power drives decreasing APE in the lead up to El Niño events. Hu et al. (2014) found that El Niño events perturbed with an imposed westerly wind burst in their modeling study showed strongly negative values of W_{mp} associated with decreasing APE_{mp} , but in the unperturbed composite, little association was found. It is therefore likely that in the composite of all El Niño events shown in Figure 2.1, events that do not

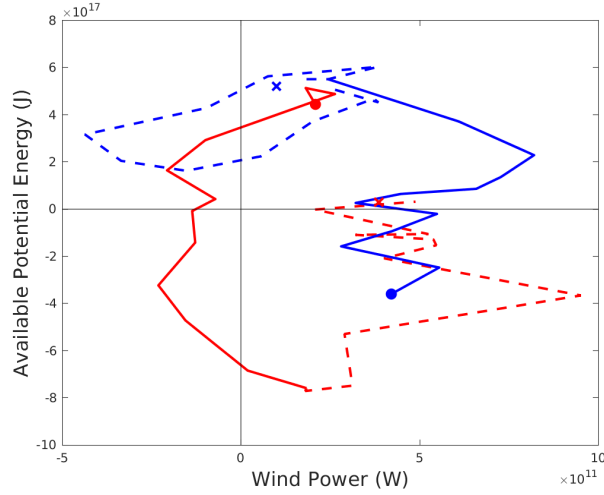


Figure 2.1: Composite of monthly APE_{mp} vs W_{mp} trajectories for El Niño (red) and La Niña (blue) in observations with two month smoothing applied. Solid lines indicate trajectories for the year leading up to an event, while dotted lines indicate trajectories for the year following the onset of the event. A heavy dot indicates January of the ENSO year, while an X marks December of the year following each event.

show the development of strong westerly winds wash out the events that do. With such a small number of events ($n=9$), it is hard to draw statistically meaningful conclusions, thus necessitating the modeling study carried out in Chapter 3.

To explore the spatial variance of $W_{MJO,K}$, Figure 2.2 shows the composite of $\mathbf{u}_K \cdot \boldsymbol{\tau}_{MJO}$ standard deviation during El Niño events. This figure shows a maximum along the coast of New Guinea, as well as a larger meridional influence in the western tropical Pacific, which weakens into the central and eastern Pacific. This zonal extent is consistent with the MJO characteristics in observations, where MJO events form in the Indian Ocean and propagate eastward into the Pacific. The meridional extent is largely driven by the spatial extent of Kelvin wave activity, which is sharply confined to the Equator. This variability differs somewhat from what is found in the modeling study described in Chapter 3, which will be discussed there. In particular, the spatial variability in $W_{MJO,K}$ is found to peak at the date line, and that spatial variability is used to create an index characterizing the influence

of the MJO wind stress on Kelvin wave-associated currents in a GCM (Lybarger and Stan, 2018). For direct comparison with that study, the same region is used here ($1^{\circ}\text{S} - 3^{\circ}\text{N}$ and $175^{\circ}\text{E} - 160^{\circ}\text{W}$, hereafter referred to as “the $W_{MJO,K}$ region”) to compute the analogous index for observations. That index is created by averaging the square of $\mathbf{u}_K \cdot \boldsymbol{\tau}_{MJO}$ in the $W_{MJO,K}$ region over January-July, and thus captures periods during which \mathbf{u}_K and $\boldsymbol{\tau}_{MJO}$ covariability is of maximum amplitude in the first seven months of the year, regardless of sign. To demonstrate this, Figure 2.3 shows the daily time series of $W_{MJO,K}$ for a selection of three El Niño events for which the $W_{MJO,K}$ index is at maximum and three El Niño events for which the $W_{MJO,K}$ index is at minimum. It can clearly be seen that this index selects for events which have high variability in this term. Not only that, but Figure 2.4 shows that this index shows a linear relationship with December-January-February Niño 3 index, which is significant at the 80% confidence level. This indicates that when variability in $W_{MJO,K}$ is high, the resulting El Niño event is of stronger amplitude. The three events which are determined to be most strongly influenced by the MJO are the 1997/98 event, the 2006/07 event, and the 2009/10 event and the three events least influenced by MJO are the 1991/92 event, the 1994/95 event, and the 2014/15 event.

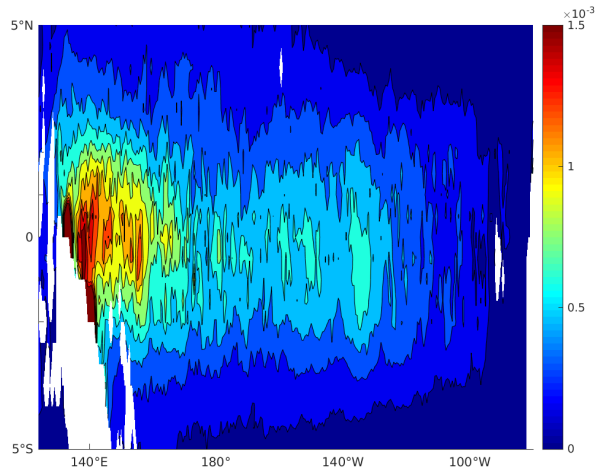


Figure 2.2: Composite of $W_{MJO,K}$ standard deviation spatial distribution for all El Niño events in observations.

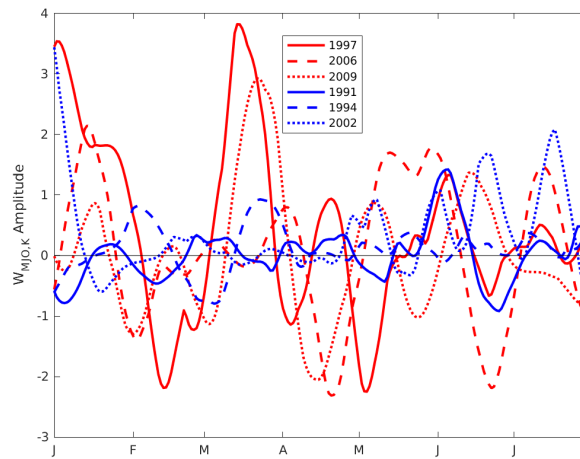


Figure 2.3: January to July $W_{MJO,K}$ index time series prior to the peak of El Niño for the three events most affected by MJO (red) and the three events least affected by MJO (blue), as selected by the $W_{MJO,K}$ index.

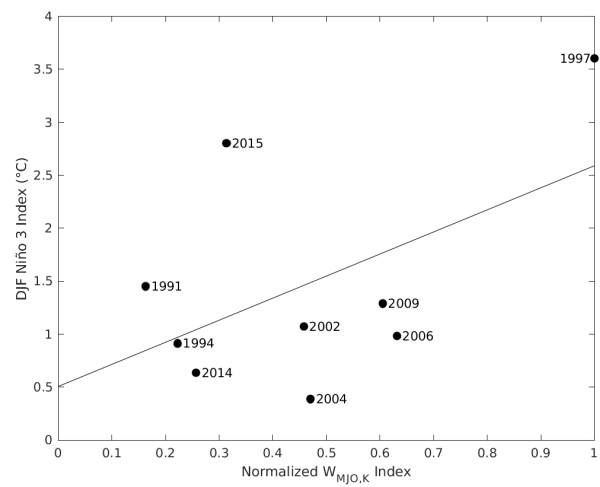


Figure 2.4: Scatter plot of the $W_{MJO,K}$ index averaged between January and July prior to the peak of El Niño vs the DJF average Niño 3 index. Superimposed is the linear regression of DJF average Niño 3 index on the normalized $W_{MJO,K}$ index and the El Niño year corresponding to each point. Linear regression is significant at the 80% confidence level.

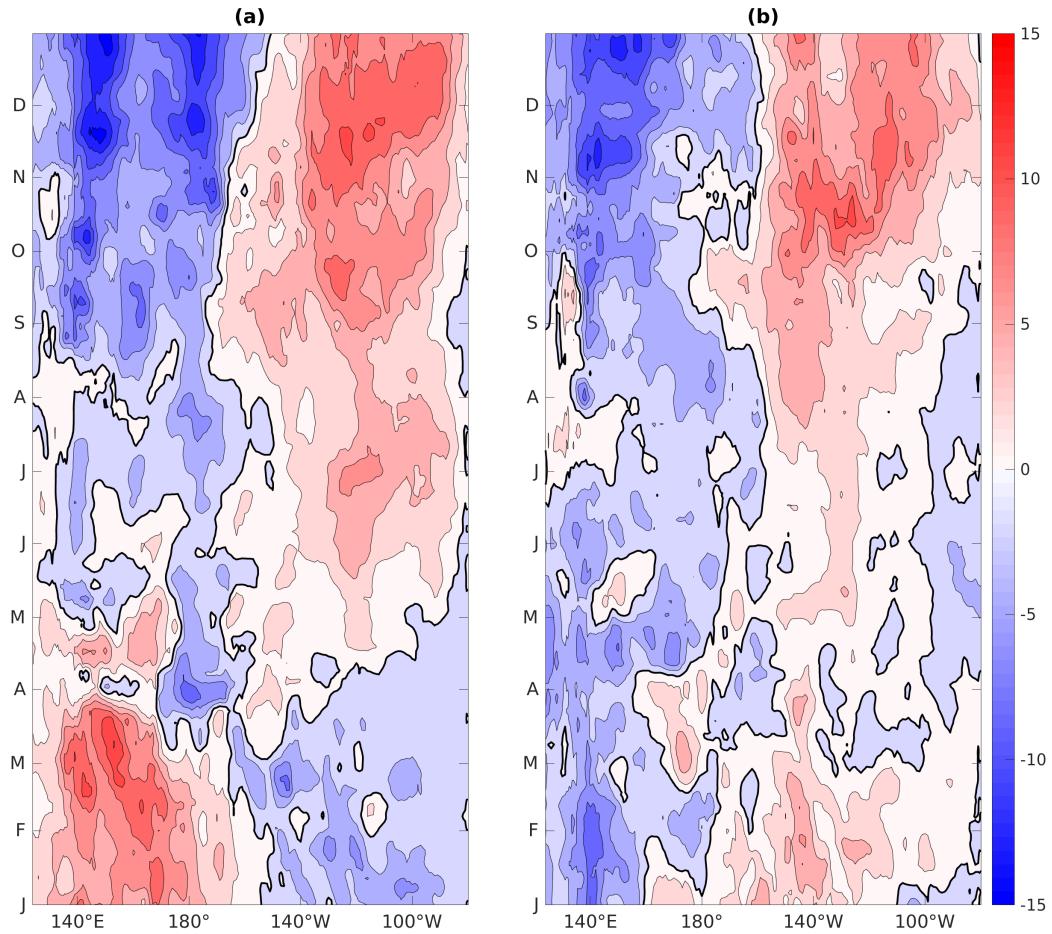


Figure 2.5: Composite Hovmöller diagram of the equatorially ($5^{\circ}\text{S} - 5^{\circ}\text{N}$) averaged Kelvin wave component of 20°C isotherm depth anomalies for El Niño events ($n=3$) which are most influenced by the MJO (a; 1997, 2006, and 2009) and El Niño events ($n=3$) which are least influenced by the MJO (b; 1991, 1994, and 2014). Units are meters.

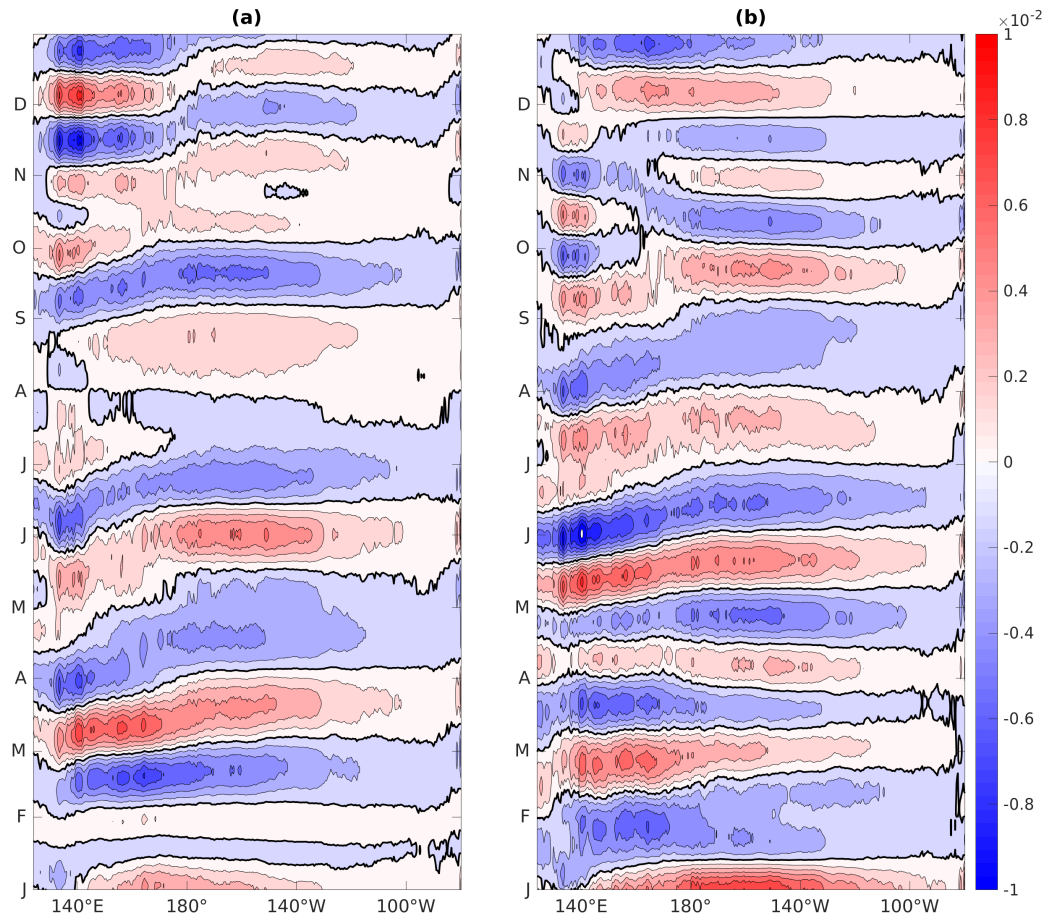


Figure 2.6: Composite Hovmöller diagram of equatorially ($5^{\circ}\text{S} - 5^{\circ}\text{N}$) averaged zonal τ_{MJO} for El Niño events ($n=3$) which are most influenced by the MJO (a; 1997, 2006, and 2009) and El Niño events ($n=3$) which are least influenced by the MJO (b; 1991, 1994, and 2014). Units are $N \cdot m^{-2}$.

To further develop the relationship between the $W_{MJO,K}$ index and the state of the tropical atmosphere and the tropical Pacific Ocean, composite Hovmöller diagrams of various field variables are shown. It should be noted that each composite is composed of only three events. These composites are therefore susceptible to being characterized by individual events, especially the very large amplitude 1997/98 El Niño event, which is included in the composite of events which are strongly influenced by the MJO. Again, this caveat necessitates the modeling study discussed in the next chapter in order to establish more robust statistical results. However, it is still beneficial to carry out this analysis for comparison. Figure 2.7 shows the composite Hovmöller diagrams of SST anomalies for those El Niño events determined to be most strongly influenced by the MJO and those determined to be least influenced by the MJO. There are several interesting features differentiating these diagrams. The peak SST anomalies in Figure 2.7(a) are of considerably greater amplitude than (b), and they also peak in the far eastern Pacific, while the anomalies in (b) peak in the central Pacific, around 150°W. In Figure 2.7(a) the anomalies seem to propagate from the western Pacific to the central and eastern Pacific between April and July, while in (b) the anomalies emerge around the dateline and largely persist there, with some eastward growth occurring in the summer. This eastward propagation which is much stronger in (a) is consistent with MJO-associated Kelvin wave activity (Enfield, 1987; Hendon et al., 1998; Zhang, 2001).

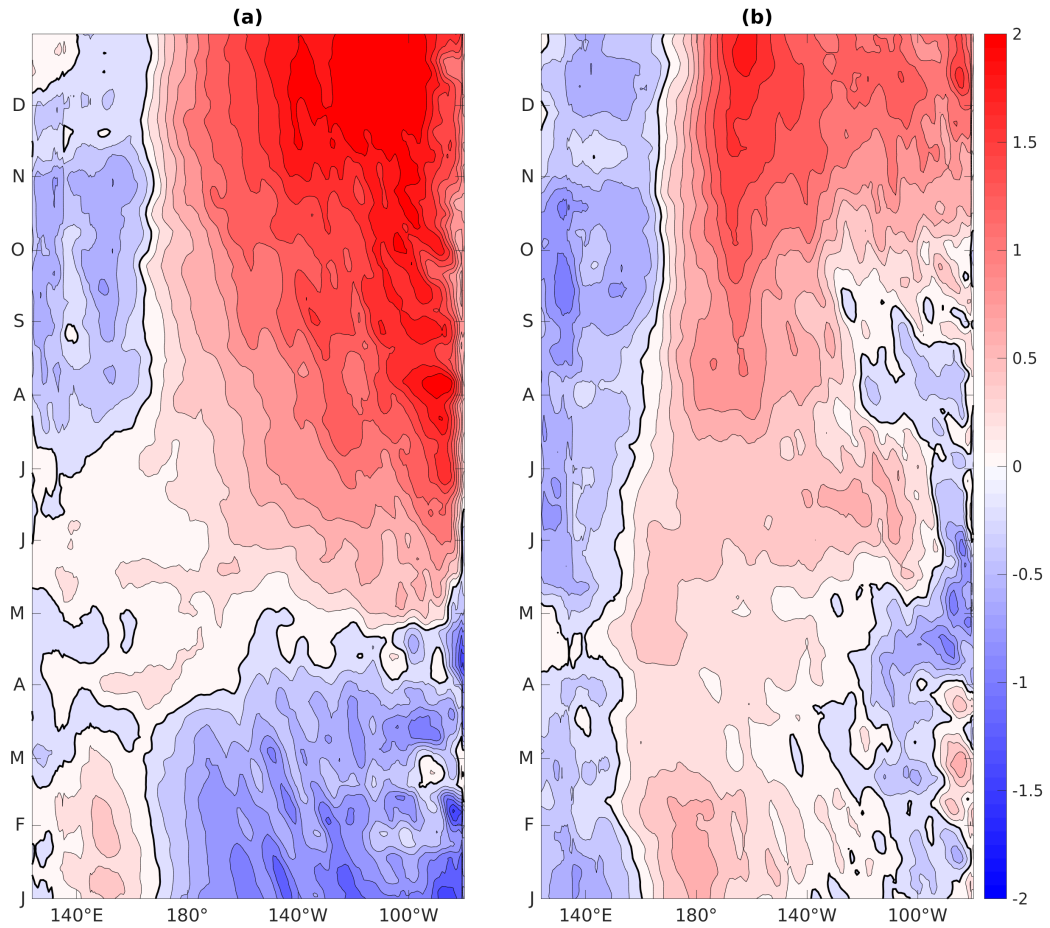


Figure 2.7: Composite Hovmöller diagram of equatorially ($5^{\circ}\text{S} - 5^{\circ}\text{N}$) averaged SST anomalies for El Niño events ($n=3$) which are most influenced by the MJO (a; 1997, 2006, and 2009) and El Niño events ($n=3$) which are least influenced by the MJO (b; 1991, 1994, and 2014). Units are $^{\circ}\text{C}$.

To show the state of Kelvin wave activity in each composite, Figure 2.5 shows the equatorial Kelvin wave component of thermocline depth (defined as the 20°C isotherm depth) anomaly, which is determined by projecting the meridional structure of a Kelvin wave (Kirtman, 1997) onto the thermocline depth anomalies. Figure 2.5(a) shows the development of considerable anomalous downwelling in the western Pacific from the beginning of the year, and significant eastward propagation of that downwelling from March to June, consistent with the positive SST anomalies seen to develop in the same region at roughly one month delay. In the latter half of the year, upwelling anomalies are seen in the western Pacific, while downwelling anomalies are seen throughout the eastern Pacific in both composites, consistent with the flattening of the thermocline seen during El Niño events. Downwelling signals in Figure 2.5(b) are inconsistent and are generally confined to the central/eastern Pacific. Of course, these composites are created with covariability of MJO wind stress and Kelvin wave activity in mind, so it should not be surprising that stronger Kelvin wave activity is seen in the composite of high $W_{MJO,K}$ index values. What is somewhat surprising at first glance, however, is Figure 2.6. Here, we see that the events that are weakly influenced by the MJO, seen in Figure 2.6(b), actually show higher amplitudes of zonal τ_{MJO} . However, along with the Kelvin wave composite, the reason for this becomes clear. Because the Kelvin wave activity is inconsistent and very weak in the western Pacific in 2.5(b), this τ_{MJO} forcing apparently does not project strongly on the ocean state, while the τ_{MJO} activity seen in Figure 2.6(a) does, likely due to the fact that the lower frequency tail of MJO-related wind activity projects more strongly onto Kelvin wave activity (Hendon et al., 1998) than higher frequency MJO winds. Indeed, the strong bout of downwelling Kelvin wave signals in March and the triggering of eastward propagation into the central and eastern Pacific in late April/March is simultaneous with a strongly westerly phase of the MJO wind stress in March and later a rapidly propagating bout of westerly MJO wind stress in late April/May. Easterly phases of MJO wind stress are also seen in Figure 2.6, but, as discussed in Section 1.2, this is consistent with the findings of Seiki et al. (2009), that westerly wind anomalies more strongly influence the ocean state in the lead up to El

Niño than do easterly wind anomalies.

2.5 Discussion

The relationship between the $W_{MJO,K}$ index and the ultimate strength of El Niño events via the mechanism of MJO wind stress forcing of oceanic Kelvin waves has been established in observations. The $W_{MJO,K}$ index is also found to select for lower frequency MJO wind activity, consistent with Hendon et al. (1998), who found Kelvin wave activity to be more responsive to the lower frequency tail of the MJO. Those results, along with those shown in figures 2.7, 2.5, and 2.6 establish $W_{MJO,K}$ as a viable way to quantify the influence of MJO activity on the state of the ocean. However, due to the relatively short time period of these observations and the interannual nature of ENSO, these results are not particularly robust. The next chapter will explore the relationships found in observations in a long free run of a GCM in order to more robustly characterize these relationships. That the 1997/98 event is chosen as the clear standout in observations by this index is encouraging, as this event has previously been established to have been strongly influenced by MJO activity (e.g. McPhaden and Yu, 1999). Figure 2.7 shows a peculiar property of this index, in that it seems to differentiate between central Pacific (CP) and eastern Pacific (EP) El Niño events. This relationship has not been further explored here for two reasons: in observations, further segregating El Niño events into CP and EP events would even further dilute the robustness of the results, and the model used in Chapter 3 does not capture CP El Niño variability with much reliability.

Chapter 3: MJO-Kelvin Wave Energetics in SP-CCSM4

3.1 Model Description

The analyses and results discussed in this chapter are based on the Super-Parameterized Community Climate System Model, version 4 (SP-CCSM4) (Stan and Xu, 2014), which uses an explicit 2D cloud resolving model (CRM) with horizontal resolution of 4km to simulate moist convection processes. A CRM is embedded in each grid column of the atmospheric model. The primary reason for choosing this GCM is the fidelity of the MJO simulated by SP-CCSM4 and a reasonable simulation of ENSO (Stan and Xu, 2014), despite the relatively coarse horizontal resolution of the ocean model ($1^\circ \times 1^\circ$ at the equator). The fidelity of the MJO in SP-CCSM4 is demonstrated by the phase diagram shown in Figure 3.1, which compares well to the schematic diagram shown in Figure 1.3. The horizontal resolution of the atmospheric model is 2.5° (longitude) \times 1.9° (latitude), with 30 vertical levels. The simulation used for this study is a basic free control run using the present day atmospheric CO₂ concentration of 368.9 ppmv. This run was initialized in 2006 and run for 150 years, though only the last 100 years of the simulation will be used here, to account for spin-up time. In these 100 years, 20 El Niño events and 19 La Niña events occur.

The energetics relationships described in Section 2.2 are present in SP-CCSM4. Figure 3.2 shows the strong anticorrelation between the Niño 3 index and APE with around one month lag time in the El Niño composite, and Figure 3.3 shows the same relationship between monthly means of APE and W as in Hu et al. (2014), where El Niño events trace a counter-clockwise trajectory in the lower left quadrant and La Niña events trace a counter-clockwise trajectory in the upper right quadrant, forming an approximately closed loop and indicating that leading up to El Niño (La Niña), W is negative (positive) and APE is

decreasing (increasing). The relationship shown between monthly means of APE and W also hold between daily values (not shown).

MJO Lifecycle composite

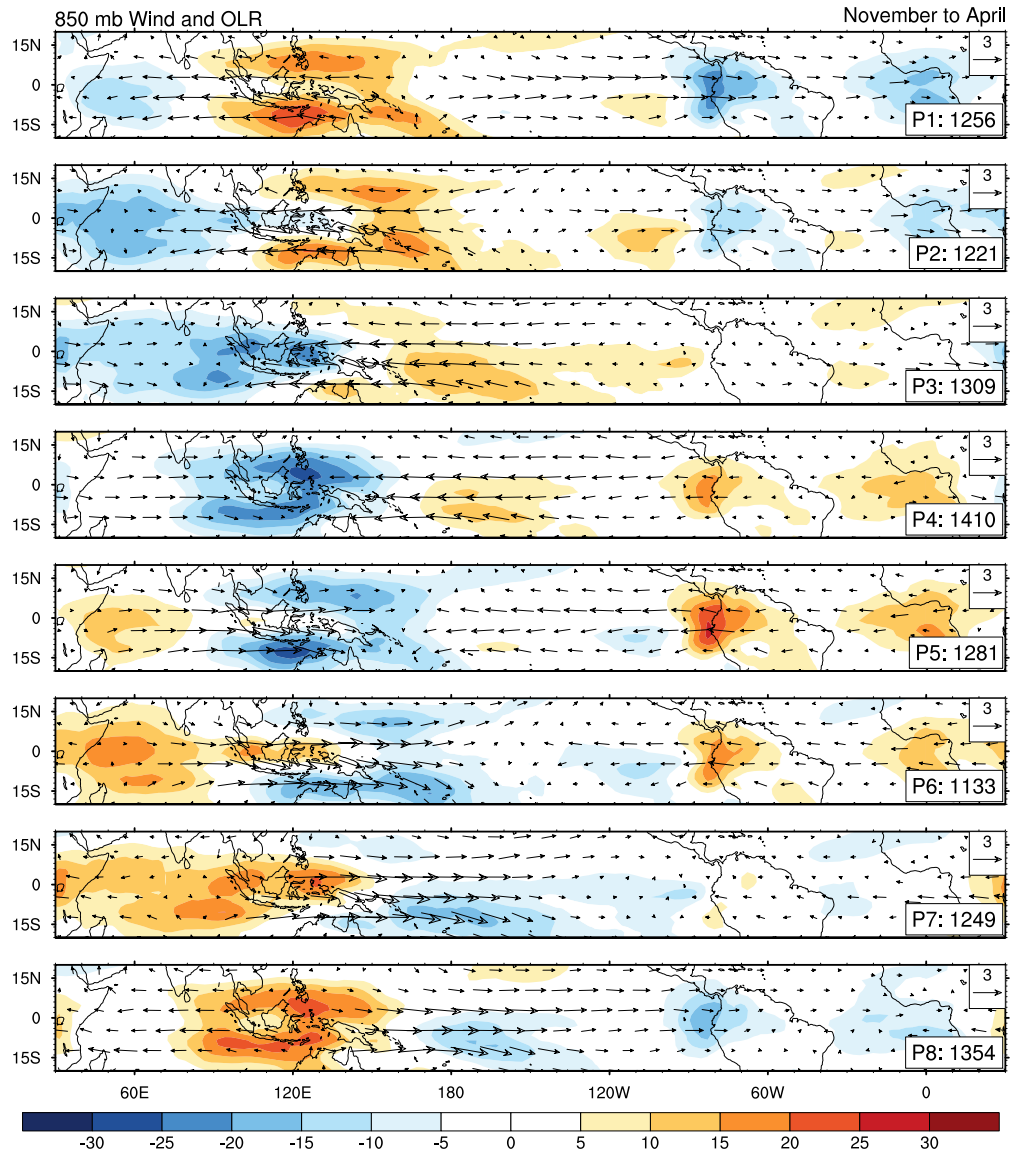


Figure 3.1: Schematic diagram of the MJO lifecycle as constructed from 20-100 day bandpass filtered composites of 850mb zonal wind anomalies and outgoing longwave radiation anomalies from SP-CCSM4. The lifecycle is divided into 8 phases (P1 through P8), and each phase has the number of days specified.

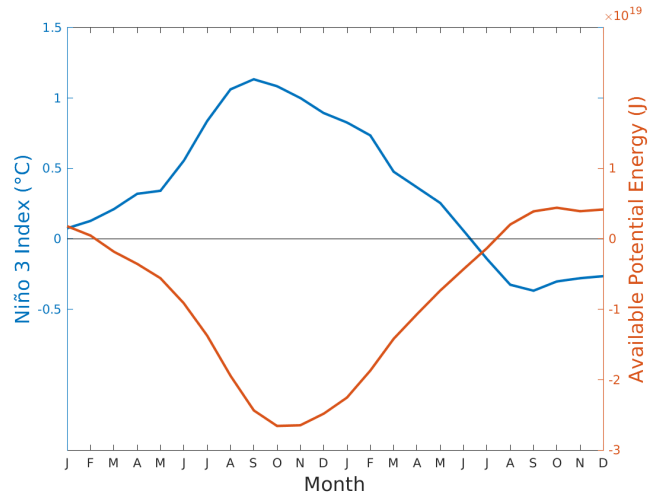


Figure 3.2: Composite of Niño 3 index vs time (blue) and APE_{mp} vs time (orange) for El Niño events in SP-CCSM4.

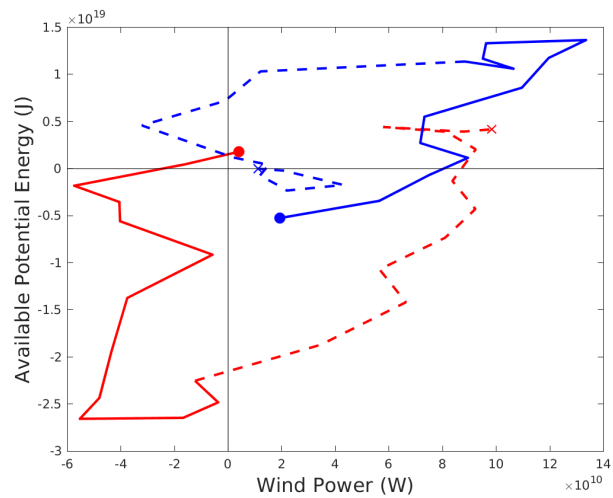


Figure 3.3: Composite of monthly average APE_{mp} vs W_{mp} trajectories for El Niño (red) and La Niña (blue) in SP-CCSM4 with two month smoothing applied. Solid lines indicate trajectories for the year leading up to an event, while dotted lines indicate trajectories for the year following the onset of the event. A heavy dot indicates January of the ENSO year, while an X marks December of the year following each event.

3.2 El Niño Comparisons

The spatial structure of $W_{MJO,K}$ variability during a typical El Niño in SP-CCSM4 is determined by calculating the standard deviation of $\mathbf{u}_K \cdot \boldsymbol{\tau}_{MJO}$ over each gridpoint in the tropical Pacific for the year leading to each El Niño event (i.e. one value per gridpoint per El Niño event). The composite of the standard deviation across all El Niños simulated by the model is then taken, as was done for Figure 2.2. A composite map of $\mathbf{u}_K \cdot \boldsymbol{\tau}_{MJO}$ standard deviation is shown in Figure 3.4. Based on Figure 3.4, an index of $W_{MJO,K}$ variability is created by averaging the square of $\mathbf{u}_K \cdot \boldsymbol{\tau}_{MJO}$ between 1°S - 3°N and 175°E - 160°W. This region is indicated by the box in Figure 3.4, and is the same region used for calculating the $W_{MJO,K}$ index in Chapter 2. For each El Niño year, the December-January-February average of Niño 3 index during the peak of the event is regressed on the $W_{MJO,K}$ index averaged between January and July leading up to the event, as was done for Figure 2.3 in Section 2.4. The regression coefficient in SP-CCSM4 is found to be statistically significant at the 95% level. A scatter plot of this regression is shown in Figure 3.5. No such relationship is found for average, maximum, or minimum values of $W_{MJO,K}$ during this period, and so it is total variability in $W_{MJO,K}$ over this region that seems to be relevant for El Niño development, as supported by the results shown in Chapter 2. Although the correlation coefficient between u_K and zonal τ_{MJO} in the region indicated by Figure 3.4 is quite small, it reaches a maximum when zonal τ_{MJO} leads u_K by two months, thus necessitating the inclusion of summer months to account for this lag, despite relative weakness of MJO activity in boreal summer.

To capture the overall state of thermocline variability across the Pacific basin, another index defined as the square of thermocline depth anomaly integrated over the domain will be used (TCV). As a measure of MJO activity that is distinct from oceanic measures, the Real-time Multivariate MJO (RMM) index will be used. The RMM index is calculated by taking the leading pair of EOFs of the combined fields of normalized, near-equatorially averaged 850-hPa zonal wind, 200-hPa zonal wind, and outgoing longwave radiation and

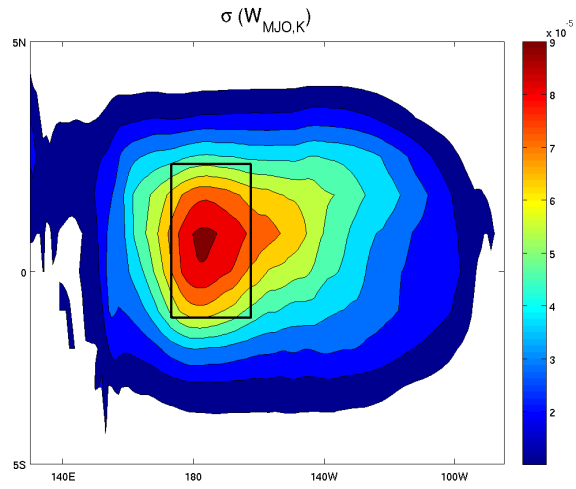


Figure 3.4: Composite of $W_{MJO,K}$ standard deviation spatial distribution for all El Niño events ($n=20$) in the SP-CCSM4 control run.

projecting the daily observed data onto these EOFs with the annual cycle and interannual variability removed (Wheeler and Hendon, 2004). For simplicity, APE_{mp} will hereafter be referred to as APE, and W_{mp} will hereafter be referred to as W .

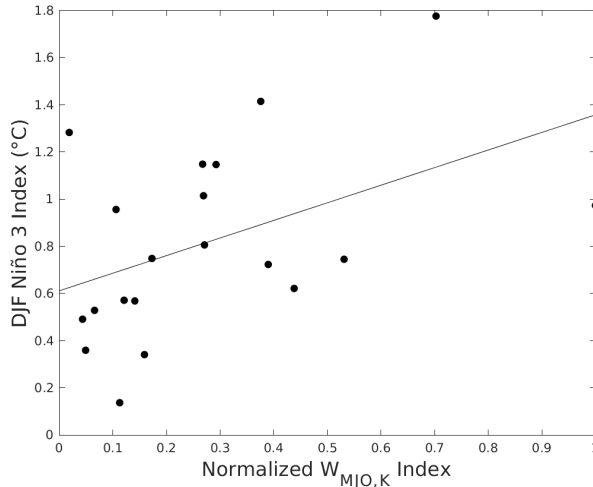


Figure 3.5: Scatter plot of the $W_{MJO,K}$ index averaged between January and July, normalized by the maximum value, prior to the peak of El Niño vs the DJF average Niño 3 index for the SP-CCSM4 control run. Superimposed is the linear regression of DJF average Niño 3 index on the normalized $W_{MJO,K}$ index.

To compare the state of the modeled system during various El Niño events, three comparison criteria have been used. First, the maximum of the monthly average RMM index between January-July prior to the peak of El Niño for each of the twenty El Niño years is calculated, and thus give a comparison of El Niño events with strong and weak MJO activity based solely on the atmospheric state. $+N_{RMM}$ corresponds to the composite of the seven El Niño events with the strongest maximum monthly RMM values and $-N_{RMM}$ corresponds to the composite of the seven El Niño events with the weakest maximum monthly RMM values. Second, the El Niño years are ranked according to the average value of the $W_{MJO,K}$ index from January to July prior to the peak of El Niño. $+N_{MJO,K}$ is a composite of the seven El Niño events for which this criterion is at its strongest, and $-N_{MJO,K}$ is a composite of the seven El Niño events for which this criterion is at its weakest, giving a comparison of those years with quantifiably strong MJO influence on the ocean via induced or amplified Kelvin wave activity. Finally, the El Niño years are ranked according to the average value of TCV during January to July of prior to the peak

Table 3.1: Comparison of El Niños included in each of the six composites. Along the left side is the corresponding composite, while along the top is the corresponding El Niño, numbered chronologically within the model run.

| Event Case | 1 | 2 | 3 | 4 | 5 | 6 | 7 | 8 | 9 | 10 | 11 | 12 | 13 | 14 | 15 | 16 | 17 | 18 | 19 | 20 |
|---------------|---|---|---|---|---|---|---|---|---|----|----|----|----|----|----|----|----|----|----|----|
| $+N_{RMM}$ | | | ■ | | | | ■ | | | ■ | ■ | ■ | ■ | ■ | ■ | | | | | |
| $-N_{RMM}$ | ■ | ■ | | | ■ | | | ■ | ■ | | | | | ■ | | | | | | ■ |
| $+N_{MJO,K}$ | | ■ | ■ | ■ | | | | | | | ■ | | | | ■ | | | | ■ | ■ |
| $-N_{MJO,K}$ | | | | | | ■ | | ■ | | | | | | ■ | | ■ | ■ | ■ | | ■ |
| $+N_{TCV}$ | ■ | | ■ | | ■ | | | | | | | ■ | | | | | | | | ■ |
| $-N_{TCV}$ | | ■ | | | | | ■ | | | ■ | | | ■ | | | ■ | ■ | | ■ | |

of El Niño ($+N_{TCV}$ designates the seven El Niño events for which the average value of TCV is at its strongest and $-N_{TCV}$ designates the seven El Niño events for which the average value of TCV is at its weakest) to contrast events with strong and weak basin-wide thermocline variability. Contrasting the El Niño years this way gives three distinct criteria for comparison, allowing separation of the effects of strong MJO activity alone, the effect of strong MJO forcing that projects quantifiably onto Kelvin wave activity, and the effect of thermocline variability from any source. It should be noted that there is overlap between the composites. $+N_{RMM}$ and $+N_{MJO,K}$ share three events, while $-N_{RMM}$ and $-N_{MJO,K}$ share four. $+N_{TCV}$ shares one event with $+N_{MJO,K}$ and two with $+N_{RMM}$. $+N_{TCV}$ actually shares three cases with $-N_{MJO,K}$ and five with $-N_{RMM}$, suggesting that the ocean thermocline variability is driven by processes other than the winds in this composite. $-N_{TCV}$ shares only one event each with $-N_{MJO,K}$ and $-N_{RMM}$, while it shares two with $+N_{MJO,K}$ and $+N_{RMM}$. This information is summarized in Table 3.1.

In this framework, the MJO exerts an influence on the oceanic state via the wind power. The wind power generates APE via buoyancy power in the ocean, which is then converted into the kinetic energy of Kelvin waves, which in turn affects the total thermocline

variability which here is quantified by TCV. TCV describes the thermocline variability and thus the SST variability in the eastern Pacific, and therefore is associated with ENSO events. TCV can be generated by phenomena other than the MJO (e.g., layers with large density gradients), and is therefore used as a separate criterion for ranking to distinguish El Niño years with especially active thermocline variations from those with strong Kelvin wave activity associated with MJO. Conversely, as discussed in Section 1.2, the MJO occurs in varying strength every year, yet every year does not result in an ENSO event, and so using the RMM index as a ranking measure will provide insights as to how the MJO affects ENSO development without regard to the subsequent projection onto the oceanic state, given only that the system will subsequently evolve into El Niño.

3.3 Results

Noticeable differences emerge from the composites of El Niño events based on the RMM index (atmosphere only), the $W_{MJO,K}$ index (atmosphere-ocean), and TCV (ocean only). Figure 3.6 shows the composite time series of APE over the year leading to an El Niño event, based on the ranking criteria described in Section 3.2, along with error bars indicating the standard deviation of composite members. The year begins with little to distinguish complementary composite pairs, though $\pm N_{RMM}$ begin the year at essentially zero, $\pm N_{MJO,K}$ begin the year slightly positive, and $\pm N_{TCV}$ begin the year slightly negative. As the year enters spring, $+N_{RMM}$ and especially $+N_{MJO,K}$ decrease more rapidly than the other cases, with $-N_{RMM}$ and $-N_{MJO,K}$ decreasing considerably more slowly and $\pm N_{TCV}$ barely decreasing at all. By March, $+N_{MJO,K}$ has separated from $-N_{MJO,K}$, and they remain separated for the rest of the year, a condition that the other composite pairs never reach, suggesting that the $W_{MJO,K}$ index outperforms both TCV and the RMM index as indicators of APE development. Each of the cases show qualitatively similar structure. Early in the year, all cases show relatively weakly decreasing APE until the summer, during which the negative slope intensifies. APE reaches a minimum in the fall, coinciding with

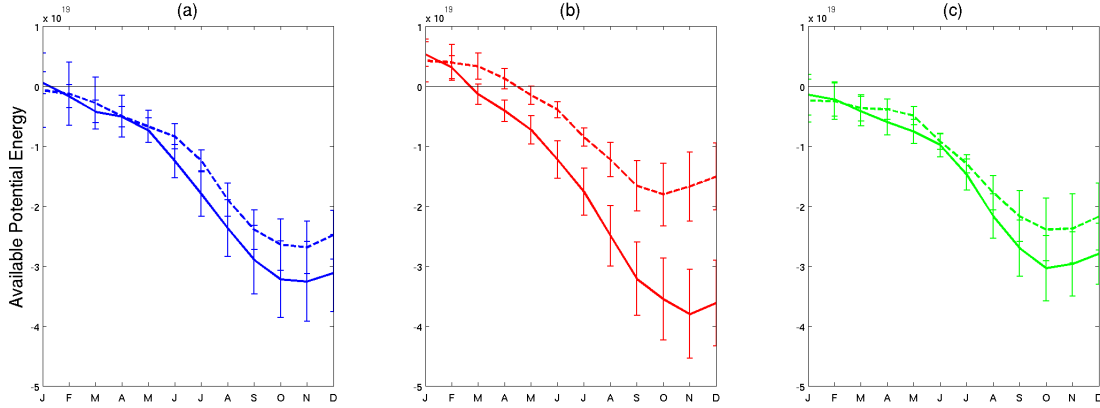


Figure 3.6: Compositd APE vs time for (a) $+N_{RMM}$ (solid blue), (a) $-N_{RMM}$ (dotted blue) (b) $+N_{MJO,K}$ (solid red), (b) $-N_{MJO,K}$ (dotted red), (c) $+N_{TCV}$ (solid green), and (c) $-N_{TCV}$ (dotted green). Units: Joules.

the peak of the event, after which it begins to increase again.

APE is driven by W in this framework, so it should be expected that the more negative slopes in the APE of $+N_{RMM}$ and especially $+N_{MJO,K}$ are accompanied by more negative values of W . Figure 3.7 shows that is generally the case. Interestingly, $+N_{RMM}$ shows the most negative values of W in January (though this is closely followed by $-N_{RMM}$), while $+N_{MJO,K}$ shows the most positive values. In February, $\pm N_{RMM}$ show a slightly positive slope, while $\pm N_{MJO,K}$ and $\pm N_{TCV}$ have decreased. In March, $+N_{MJO,K}$ shows the strongest negative values of W for the whole year, while $-N_{MJO,K}$ changes little between February and March. W for $\pm N_{RMM}$ and $\pm N_{TCV}$ all decrease over this period, and, as with the APE, we do not see the separation beyond a standard deviation between these composite pairs like we do with $\pm N_{MJO,K}$. Interestingly, W for $+N_{RMM}$ increases suddenly in April, significantly greater than $-N_{RMM}$, before dropping back down in May as $-N_{RMM}$ becomes positive by June, while $+N_{RMM}$ continues to decrease, resulting in one of the clearest differences in W between any complementary pairs. Despite this clear June separation in W for $\pm N_{RMM}$, this does not result in a clear separation in APE, perhaps due to the switch

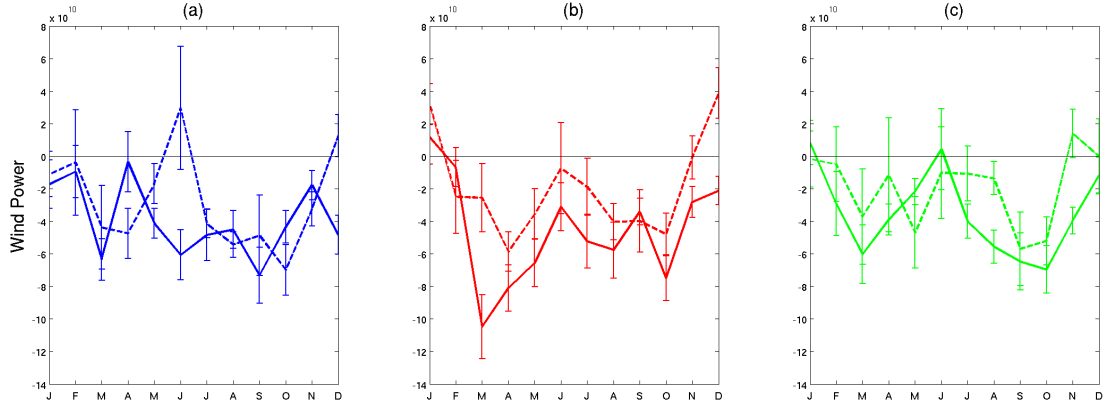


Figure 3.7: Compositd W vs time for (a) $+N_{RMM}$ (solid blue), (a) $-N_{RMM}$ (dotted blue), (b) $+N_{MJO,K}$ (solid red), (b) $-N_{MJO,K}$ (dotted red), (c) $+N_{TCV}$ (solid green), and (c) $-N_{TCV}$ (dotted green). Units: Watts.

that occurs in April, suggesting that sustained wind projection onto the ocean current is more important than one-off events. W for $+N_{MJO,K}$ takes on very strong negative values in March, indicative of sustained winds projected onto the ocean current, and though the same magnitude separation is not seen in $\pm N_{MJO,K}$ for the rest of the year, $+N_{MJO,K}$ retains strongly negative values of W , in agreement with the strongly negative slope of APE for that case. $+N_{TCV}$ wind power is more negative than $-N_{TCV}$ in early spring, coinciding with the more rapid decrease of $+N_{TCV}$ APE during this period, but $-N_{TCV}$ wind power becomes more negative in the summer, causing the convergence of APE in these cases. Interestingly, $\pm N_{TCV}$ are the only complementary composites showing clear separation after the summer, driving the resultant separation in APE for the peak of El Niño. Toward the end of summer, all cases largely converge to similar magnitudes, likely indicating the feedback of the maturing El Niño on the wind power.

To support the assertion that W creates APE via the influence of the buoyancy power (B), W is regressed on B . Over the last 100 years of the model run, the correlation coefficient between these two variables is 0.8, indicating a very strong linear relationship. Figure 3.8 shows a scatter plot of this relationship, along with the regression line. It is clear from

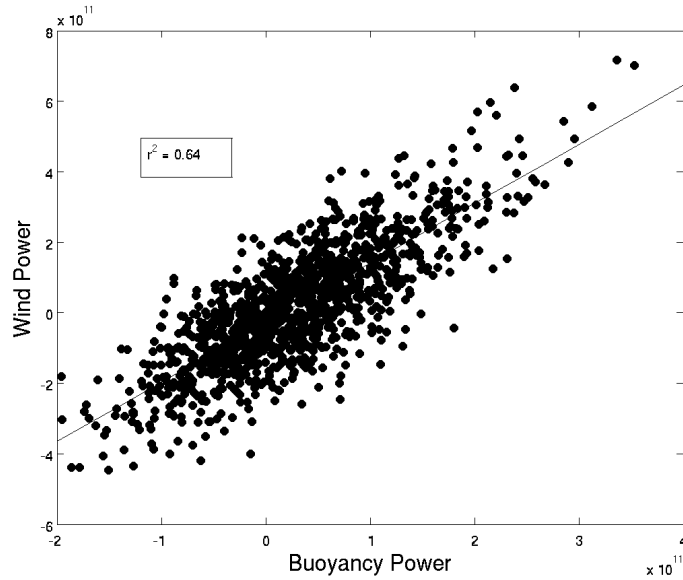


Figure 3.8: Scatter plot of mean perturbation wind power versus mean perturbation buoyancy power in SP-CCSM4, showing a clear, strong linear relationship. The regression line is superimposed.

this plot that close correspondence exists between the wind driven current and thermocline perturbations due to divergence of the ocean basin mass field, thus demonstrating the mechanistic relationship through which W creates APE.

It is clear from the evolution of W and APE that $\pm N_{MJO,K}$ show the greatest separation between complementary composite pairs. Indeed, $+N_{MJO,K}$ shows the greatest magnitude of APE beginning around July and persisting until the end of the year. This is driven by the fact that $+N_{MJO,K}$ generally shows the greatest magnitudes of W and B , particularly in the spring. Once APE is generated in the ocean, it must be released in the form of wave activity, including Kelvin waves, and so it should be expected that the cases which show the greatest magnitude of APE should also show the strongest Kelvin wave activity. Figure 3.9 shows composite Hovmöller diagrams of monthly values of the Kelvin wave component of thermocline depth anomalies (Kirtman, 1997) for each of the six cases. It is apparent from this figure that $+N_{RMM}$, $+N_{MJO,K}$, and $+N_{TCV}$ show considerably stronger

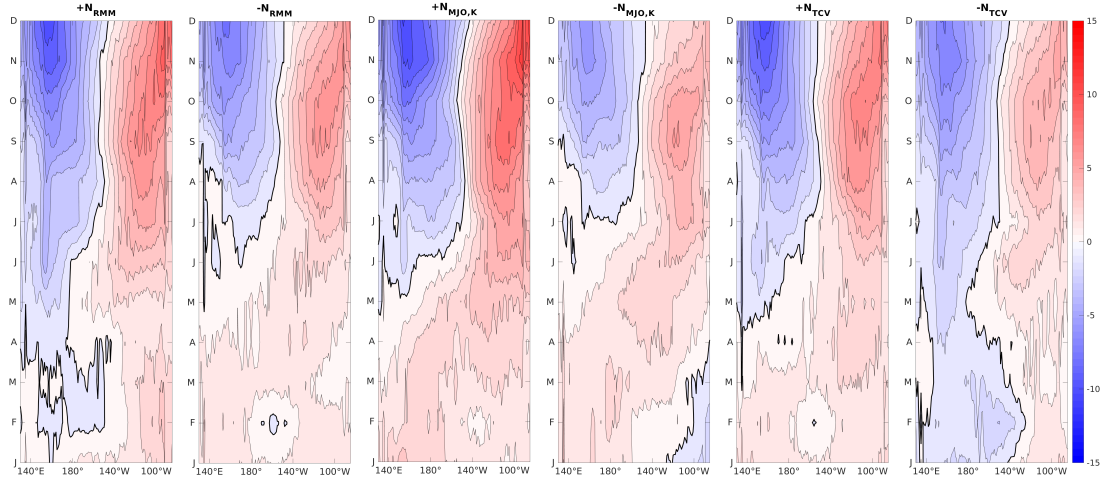


Figure 3.9: Hovmöller diagrams of the composite Kelvin wave component of thermocline depth anomaly for each experiment. Units: meters.

Kelvin wave generation by the second half of the year than do their respective counterparts. Indeed, Figure 3.9 is in direct agreement with Figure 3.6 given the understanding of the relationship between these quantities, especially for $+N_{MJO,K}$, which shows the greatest peak magnitude of APE and the greatest peak Kelvin wave generation, followed by $+N_{RMM}$, then $+N_{TCV}$. Again, the greatest difference between complementary composites is seen between $\pm N_{MJO,K}$. Figure 3.9 is consistent with the asserted relationship between W , APE, and Kelvin wave generation in the Pacific basin. In January and February, there is little to distinguish $\pm N_{MJO,K}$ in any of these quantities. However, there is a dramatic decrease in W in March for $+N_{MJO,K}$, and this condition remains until the late summer, when the cases converge to similar values. This wind power drives a more rapid decrease in APE for $+N_{MJO,K}$ than for $-N_{MJO,K}$, leading to their clear separation by April and remaining so for the rest of the year. This especially strong APE generation in $+N_{MJO,K}$ leads to especially strong Kelvin wave generation beginning in the late spring and persisting through the year.

This Kelvin wave activity gives rise to strong SST anomalies. Figure 3.10 shows the Niño 3 index for each case, clearly showing that the cases with the greatest Kelvin wave activity also show the greatest SST anomalies expressed at the peak of El Niño, with the strongest SST anomalies in $+N_{MJO,K}$, followed by $+N_{RMM}$, then $+N_{TCV}$. To investigate the spatial distribution of these anomalies, Figure 3.11 shows Hovmöller diagrams of SST anomalies for each case. All three of the strong cases show rapid increases in SST from the very start of the year. This rapid increase is mostly confined to the eastern and central Pacific, particularly in $+N_{TCV}$, but $+N_{RMM}$ and $+N_{MJO,K}$ do show positive SST anomalies west of the dateline early in the year as well. Central Pacific ($180^\circ - 150^\circ\text{W}$) SST anomalies briefly seem to acquire greater values than the eastern Pacific around the end of spring. This, in addition to the fact that the positive SST anomalies and positive Kelvin wave depth seem to have an eastward propagating component around this time, suggest that Kelvin wave activity is a significant source of SST anomalies due to zonal advection of warm water from the warm pool to the cold tongue region and due to deepening the thermocline in the eastern Pacific (i.e. transferring APE from the western Pacific to the eastern Pacific). It is possible that the initial MJO forcing which occurs in March for $+N_{MJO,K}$, the influence of which is seen in Figure 3.7(b), induces this extension, which then allows further MJO influence to extend into the central Pacific, further amplifying the SST anomaly there (Levine et al., 2017; Puy et al., 2016). For SST anomalies, as with APE and Kelvin wave depth, the greatest difference in complementary pairs is seen between $\pm N_{MJO,K}$. Because $\pm N_{RMM}$ also show strong differences, it is clear that strong MJO activity early in the year can enhance peak El Niño SST anomalies, but it is by coupling the oceanic state related to Kelvin wave activity to the atmospheric state related to MJO into a single index that the strongest differences are seen.

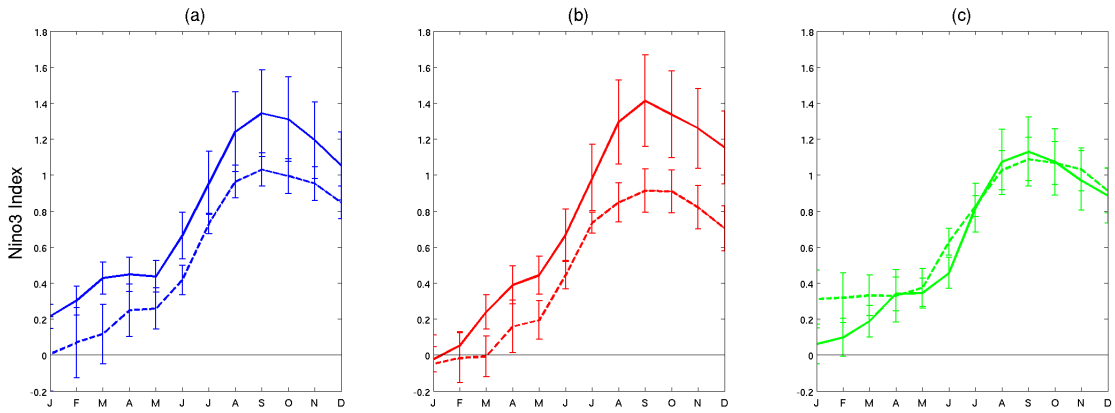


Figure 3.10: Composited Niño 3 index vs time for (a) $+N_{RMM}$ (solid blue), (a) $-N_{RMM}$ (dotted blue) (b) $+N_{MJO,K}$ (solid red), (b) $-N_{MJO,K}$ (dotted red), (c) $+N_{TCV}$ (solid green), and (c) $-N_{TCV}$ (dotted green).

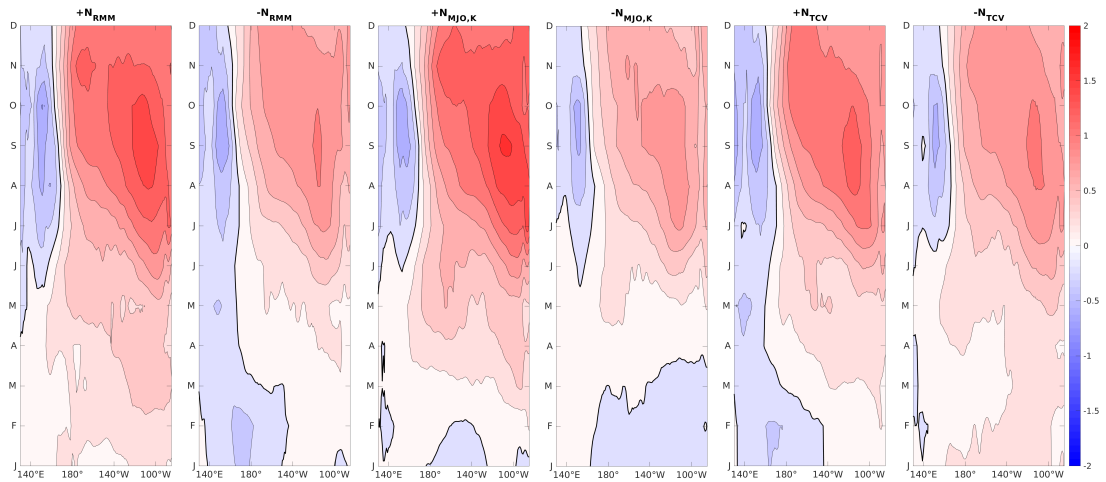


Figure 3.11: As in Figure 3.9, but for monthly SST anomalies averaged between 5°S and 5°N . Units are $^{\circ}\text{C}$.

As a preliminary examination of the differences between atmospheric and oceanic conditions between $\pm N_{MJO,K}$, the January-April average latent heat flux anomaly (LHF) and mixed layer depth anomaly (MLD) fields are shown in Figure 3.12. This time range was chosen because little difference in the structure of these fields is seen between the two cases for the rest of the year, only a difference in magnitude associated with the onset of the stronger El Niño events for $+N_{MJO,K}$. The structure of these fields is largely similar in each case, but there are some noticeable differences. Between the equator and 5°S , LHF for $+N_{MJO,K}$ shows strong negative values across the whole basin, accompanied by strong positive values between the equator and 5°N , indicating reduced evaporation there and possibly a northward shift of the ITCZ compared to the climatology. Intriguingly, the westward extent of these patches are coincident with the region associated with strong $W_{MJO,K}$ variability. Furthermore, this is also the region in which strong positive SST anomalies begin to develop in late spring/early summer for $+N_{MJO,K}$, as seen in Figure 3.11. It is possible that the thermodynamic control demonstrated in Figure 3.12(a) is influenced by the MJO activity suggested by Figure 3.7(b) in the late spring, which then amplifies the SST in the central Pacific, enhancing or inducing an eastward extension of the warm pool. The solar radiation absorbed by the water surface is then transferred into the water rather than used in evaporation. Although the effects of cloud cover are not quantified here, Dommenges and Yu (2016) showed that total cloud cover should damp SST development in spring, an effect that is not seen in $+N_{MJO,K}$, as SST is above normal throughout spring and into summer, suggesting that the total cloud cover effect on incoming solar radiation is not significantly influential during this period for this composite. A temperature gradient must exist between the surface and subsurface for heat transfer to occur. This temperature stratification will damp the shear driven turbulent mixing and reduce the depth of the mixed layer. In the aforementioned region between the equator and 5°S , $-N_{MJO,K}$ shows weak signals near zero (Figure 3.10(b)). Figure 3.10(c) shows that the warming of the ocean across this region is appropriately associated with shallow MLD in the southern off-equatorial eastern Pacific, but around the date line, this signal is

overshadowed by a strongly positive MLD off the coast of New Guinea. The deepening of the mixed layer is associated with a positive LHF anomaly, consistent with the cooling of the ocean associated with anomalously strong evaporation and MJO active convection. The MLD anomaly seen here seems inordinate compared to the magnitude of the LHF anomaly, especially in comparison to the MLD response to the LHF anomaly in the eastern Pacific. This may be due to the mixing induced by MJO wind forcing in this region penetrating the salinity-stratified layer which has a tendency to form in the western Pacific, leading to subsequent thermocline penetration by the mixed layer, thus enhancing the cooling of the subsurface via entrainment (Lukas and Lindstrom, 1991). It seems that in $+N_{MJO,K}$, there is a southward extension of anomalous convection in the western Pacific. Compared to the strength and spatial coherence of the signals seen in Figures 3.12(a) and (c), the signals seen in $-N_{MJO,K}$ are considerably weaker and largely decoupled from each other. In particular, the regions of strong negative LHF anomaly flanking New Guinea in (d) are associated with very weakly positive values of MLD anomaly, and the weakly positive MLD anomaly seen in the central Pacific is associated with weakly negative values of LHF anomaly. For the same surface heating, the shallower mixed layer in the eastern Pacific during $+N_{MJO,K}$ has a smaller heat capacity and larger SST response than the deeper mixed layer in $-N_{MJO,K}$.

These results are consistent with previous findings showing that surface fluxes control the heating and cooling of mixed layer in the western Pacific (e.g. Andersen and Kuang, 2011; Duvel and Vialard, 2007; McPhaden, 2002). In the central and eastern Pacific ocean processes dominate the mixed layer variability (e.g. Halkides et al., 2011; Lucas et al., 2010; McPhaden, 2002).

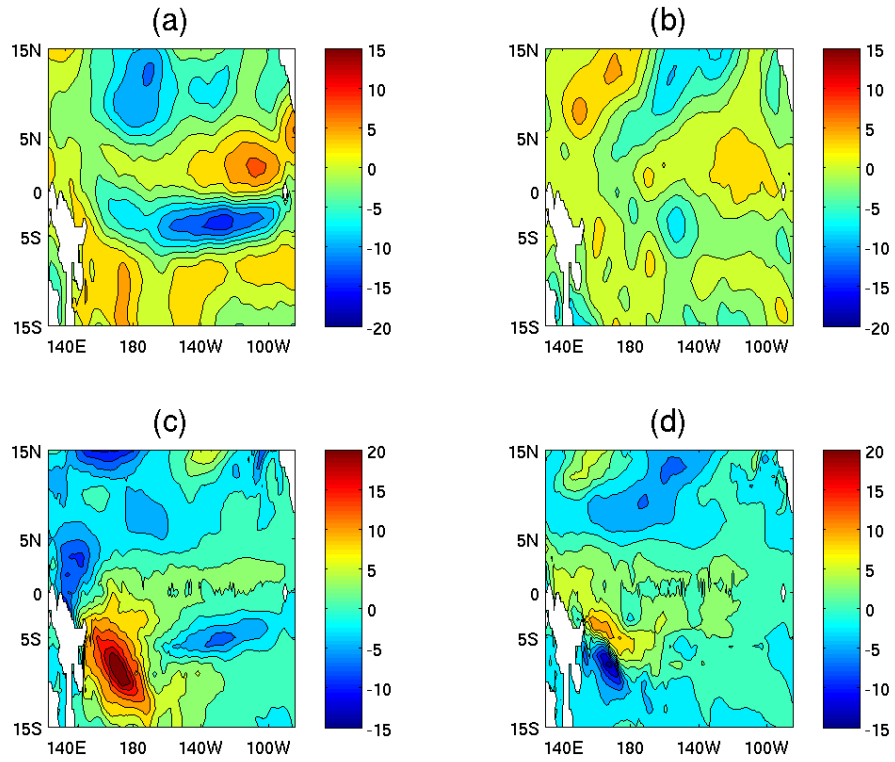


Figure 3.12: January-April average latent heat flux anomaly for $+N_{MJO,K}$ (a) and $-N_{MJO,K}$ (b), and mixed layer depth anomaly for $+N_{MJO,K}$ (c) and $-N_{MJO,K}$ (d). Units are $\text{W}\cdot\text{m}^{-2}$ and m, respectively. Negative (positive) values of LHF imply energy flux into (out of) the ocean.

3.4 Discussion

This chapter investigates the effect of the MJO on El Niño development in SP-CCSM4, in the context of the energetics framework developed by Goddard and Philander (2000) and refined by Hu et al. (2014). In this framework, the wind power is the main driver of the quasi-geostrophic APE in the ocean. The component of the wind power associated with the MJO and oceanic Kelvin waves is isolated, due to the well documented relationship between the intraseasonal variability of the tropical atmosphere and oceanic perturbations (e.g. Kessler et al., 1995; Boulanger et al., 2004; McPhaden et al., 2006; Wang et al., 2011). Using this component of the wind power, an index is created to measure the influence of the MJO on the ocean variability via induced oceanic Kelvin waves. Linear regression of DJF average Niño 3 index with the $W_{MJO,K}$ index averaged between January-July leading up to the event as the predictor is significant at the 95% level. When El Niño composites of the top and bottom tercile of the wind power index strength ($\pm N_{MJO,K}$) are compared with similar composites based on strong and weak MJO activity ($\pm N_{RMM}$) and strong and weak thermocline variability ($\pm N_{TCV}$), the strongest differences in APE, W, Kelvin wave activity, and SSTs are seen in $\pm N_{MJO,K}$, and the most extreme values of each are seen in $+N_{MJO,K}$. At the beginning of the year leading to an El Niño event the negative APE associated with both $\pm N_{TCV}$ cases (Figure 3.6) suggest the existence of an ocean state with an eastern Pacific thermocline that has already begun to deepen. This result could explain why not all MJO events are accompanied by El Niño events. The work done by the MJO induced winds increases the preexisting APE perturbations generated by the perturbation buoyancy. The wind power of $\pm N_{TCV}$ cases (Figure 3.7) for this period is close to zero. The evolution of the time series suggests a non-linear interaction between the surface winds and ocean variability, such as state dependent forcing associated with anomalous eastward extension of the warm pool (Eisenman et al., 2005; Jin et al., 2007; Levine et al., 2016; Puy et al., 2016; Levine et al., 2017), or nonlinear Bjerknes feedback enhancement (Choi et al., 2013; Takahashi and Dewitte, 2016), for which early summer wind forcing is especially

important for the strength of the subsequent El Niño event. For situations with weak MJO influence ($-N_{MJO,K}$) the negative APE takes longer to develop due to the work done by winds on the ocean, resulting in weaker El Niño events.

During the spring, the decrease in APE (Figure 3.6) is driven by the strong negative perturbations in the wind power (Figure 3.7) through the perturbation buoyancy, with the strongest development seen in $+N_{MJO,K}$ cases. This precedes the development of significant SST anomalies in the region of greatest $W_{MJO,K}$ variability, suggesting that when a strong MJO event influences the oceanic state, as seen in March in Figure 3.7(b), this forcing results in an eastward extension of the warm pool into the central Pacific, as seen in Figure 3.11 for $+N_{MJO,K}$ around April. This enhances further development of negative mean perturbation wind power, providing a sustained forcing in the central Pacific which enhances ENSO development through APE development and subsequent Kelvin wave forcing. Larson and Kirtman (2017) found that stochastic zonal wind stress forcing in March has particularly strong influence on the subsequent development of ENSO, in agreement with the findings here, that when MJO influence is at its highest for a particular event, the maximum wind power is found in March, initiating the development of APE and further wind power forcing later in the spring and summer. The Pacific basin average energetic balance well established for the low frequency variability (Goddard and Philander, 2000) holds up for intraseasonal timescales.

The thermodynamical control exerted by the MJO on the ocean mixed layer manifests through the southward extension of anomalous convective activity along the coast of New Guinea, as well as a possible northward shift of the ITCZ, as anomalously reduced evaporation is seen along the equator and anomalously enhanced evaporation is seen to the north of the equator in $+N_{MJO,K}$, hinting at the importance of the radiation budget in a mechanistic role linking MJO and ENSO evolution. Changes in the surface latent heat fluxes associated with cooling of the ocean and accordingly to strong deepening of the mixed layer there coincide with Kelvin wave activity and growing SSTs east of the dateline, suggesting that this region may have an influence on oceanic Kelvin wave activity and further on ENSO

evolution. Springtime was also hypothesized by Hendon et al. (2007) as the season when enhanced MJO activity in the western Pacific can influence the development of El Niño in the subsequent fall-winter. They attributed the MJO-ENSO interaction to equatorially symmetric MJO activity and its high sensitivity to the SST variability at the eastern edge of the warm pool persisting in late spring/early summer. Several other studies have further investigated the relationship between the MJO, westerly wind events, and the eastward extension of the warm pool (Levine et al., 2016; Puy et al., 2016; Levine et al., 2017). The basin wide influence of the MJO hinted at by the preliminary heat budget analysis, as seen in Figure 3.12, is different from previous studies, which reported a strongest correlation in the central Pacific (Zhang and Gottschalck, 2002) and western Pacific (Hendon et al., 2007).

The relationship found between the $W_{MJO,K}$ index, the forcing of downwelling Kelvin wave activity from the western tropical Pacific to the central/eastern Pacific, and the ultimate strength of El Niño events found in observations has been shown to hold true for SP-CCSM4 as well, in a statistically robust manner. This further solidifies $W_{MJO,K}$ as a reasonable measure of the MJO influence on the ocean.

Chapter 4: Modification of MJO and Kelvin Wave Forcing in a Simple Ocean Model

This chapter revisits the mechanisms governing the interaction between the MJO, El Niño, and Kelvin wave activity using sensitivity experiments with a simple model of the Pacific Ocean. These experiments suggest that MJO activity that is collocated, contemporaneous, and in phase with Kelvin wave activity is a necessary condition for a strong effect on ENSO development.

In Section 3.3, SP-CCSM4 composites of El Niño events in the upper tercile ($n=7$) of $W_{MJO,K}$ index values averaged between January and July ($+N_{MJO,K}$) develop strong values of W and APE . This leads to deeper eastern tropical Pacific thermocline anomalies, resulting in strong SST anomalies during the onset and peak of El Niño. Composites of El Niño events in the lower tercile ($n=7$) of $W_{MJO,K}$ index values from January to July ($-N_{MJO,K}$) showed weaker W and APE development, resulting in shallower thermocline anomalies and El Niño events which did not achieve the peak amplitude or rapid onset of the events in $+N_{MJO,K}$. Figure 4.1 shows the seven-month time series of the $W_{MJO,K}$ index for each composite from January-July. High (low) variability is seen in $+N_{MJO,K}$ ($-N_{MJO,K}$) because the events in this composite are specifically chosen for that reason.

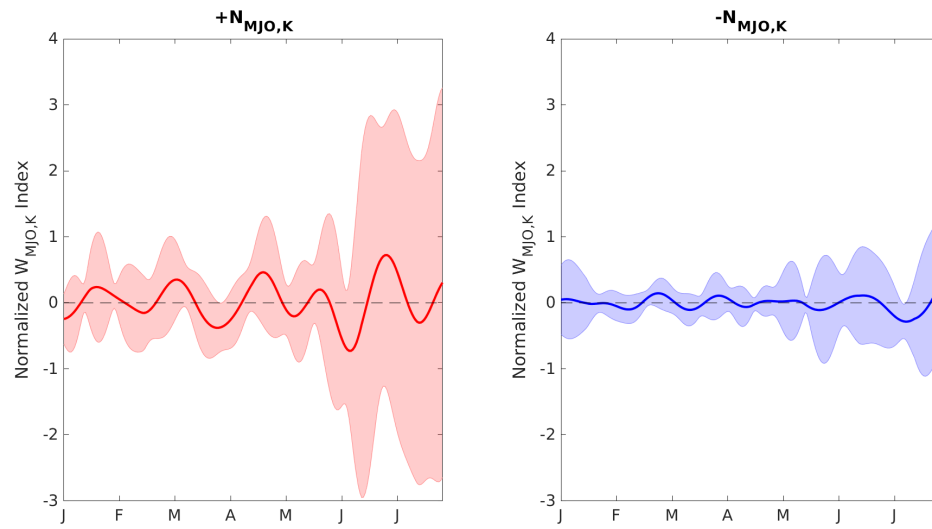


Figure 4.1: Composite time series of the normalized $W_{MJO,K}$ index during January-July for $+N_{MJO,K}$ (red, left) and $-N_{MJO,K}$ (blue, right). The shading indicates $\pm 1\sigma$ for each composite of seven El Niño events. $+N_{MJO,K}$ ($-N_{MJO,K}$) events are chosen for high (low) variance during this period.

4.1 Model Description and Evaluation

This study employs a simple ocean model to identify features which differentiate $\pm N_{MJO,K}$ cases developed and discussed in Chapter 3. The model used is the oceanic component of the nonlinear dynamical model of the coupled ocean-atmosphere developed by Zebiak and Cane (1987) for the Pacific basin (ZCocn). This model has a zonal resolution of 2° and a meridional resolution of 0.5° , covering the Pacific basin from $124^\circ\text{E} - 80^\circ\text{W}$ and $29^\circ\text{S} - 29^\circ\text{N}$. In the experiments of this study, the atmospheric model is removed in favor of prescribed wind stress forcing. The prescribed wind stress is applied to the surface of the ocean model, which updates the ocean dynamics through Kelvin and Rossby wave responses, and ultimately the SST is updated. The model has also been modified to allow for daily wind stress forcing instead of the 10-day time step of the original model, which is too coarse to effectively capture intraseasonal variability. Following the modifications of Kapur et al. (2012), the SST is first updated based on the previous time step (initial SST conditions are climatological). Then, the wind stress is prescribed to the ocean dynamical model for ten days before the SST is updated again. Thus, the prescribed wind stress and ocean dynamical fields are applied and iterated daily. The SST field is iterated at the native period of ten days because the thermodynamics of the SST model have been tuned to the ten day period and cannot be changed without affecting interactions with the mean state, to which the Zebiak-Cane model is known to be sensitive (Kapur et al., 2012). The wind stress forcing is taken from the last 100 years of the same SP-CCSM4 simulation as was used in Chapter 3.

To determine specific processes important for the relationship found in Chapter 3, tests are performed on the ZCocn model to determine if this model is sufficiently complex to capture broad features of the El Niño events simulated by SP-CCSM4. It should be noted that although the horizontal extent of El Niño is well captured by SP-CCSM4, the period is slightly shorter (48 months) than observed (Stan and Xu, 2014). To check the fidelity of ZCocn in comparison to SP-CCSM4, wind stress anomalies about the daily climatology from the last 100 years of the free run of SP-CCSM4 (the same wind stress that was used

in the free run in Chapter 3) are interpolated to the ZCocn spatial resolution and applied to the model. The resulting Niño 3 index agrees quite well with the Niño 3 index from SP-CCSM4, with a correlation coefficient of 0.804 over the whole 100 years. A comparison of these time series is shown in Figure 4.2(a), which shows a better agreement between the models during El Niño events than during La Niña events. This is confirmed by the probability density function (PDF) in Figure 4.2(b), which shows a close agreement between values of each PDF for positive Niño 3 and an underrepresentation of negative temperature anomalies in ZCocn, resulting in a bias in ZCocn of 0.17°C . Because the ocean response in this case can only be purely wind driven, roughly 35% of the variability in Niño 3 from SP-CCSM4 is supplied by processes other than the linear response of the ocean to wind forcing, perhaps nonlinear interactions or boundary forcing from outside the Pacific basin as defined in ZCocn. This chapter is focused on the interactions between the MJO wind forcing and oceanic Kelvin waves, so these factors are not as important to this chapter as the wind driven response. Figure 4.2(c) shows that the power spectra of ZCocn and SP-CCSM4 Niño 3 index peak at similar periods: 38 and 44 months, respectively. ZCocn thus seems to capture the appropriate variability related to La Niña, but does not simulate the amplitude very well. This is likely due to model limitations with respect to the temperature tendency parameterization which are tuned for El Niño prediction and may not be appropriate for La Niña. Excepting the insensitivity during La Niña, the close correspondence between Niño 3 is interesting because it has previously been found that the Zebiak-Cane coupled model is relatively insensitive to stochastic wind forcing, and thus produces an El Niño that is too regular both in amplitude and oscillation. However, Figure 4.2 demonstrates that when prescribing wind stress, ZCocn is capable of recovering most of the variability seen in Niño 3 in SP-CCSM4. Due to the high correlation between Niño 3 time series from ZCocn and SP-CCSM4 (particularly during El Niño), corresponding PDFs for positive SST anomalies, and similar power spectra, it is determined that the ZCocn model should be sufficiently complex to test the hypothesis that interactions between the MJO and Kelvin wave activity are important for the evolution of especially strong El Niño events with relatively early onset,

as is suggested by the findings in Chapter 3. Due to the relatively large spatial scale of the MJO, the spatial resolution of ZCocn should be sufficient to effectively capture the effect of the MJO wind stress at the ocean surface.

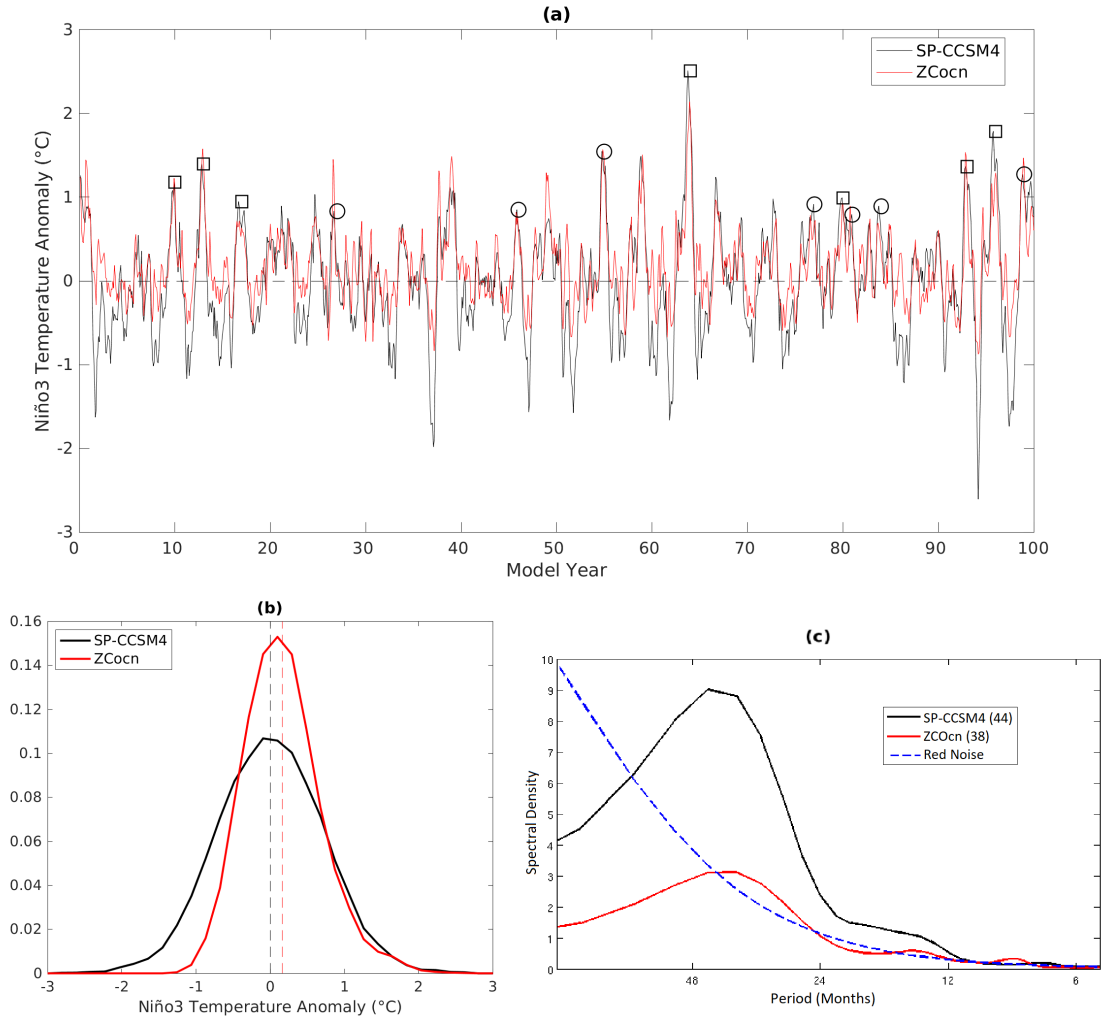


Figure 4.2: (a) Niño 3 index time series for SP-CCSM4 (black) and ZCocn forced by the SP-CCSM4 wind stress (red). The correlation between these time series is 0.804. Events which are strongly (weakly) influenced by MJO are marked by squares (circles). (b) Probability density function for Niño 3 index for SP-CCSM4 (black) and ZCocn forced by SP-CCSM4 wind stress (red). The mean of each is shown by the respective dashed lines (ZCocn shows a bias of 0.17°C). (c) Power spectra for SP-CCSM4 (black), ZCocn forced by SP-CCSM4 wind stress (red), and the red noise spectrum (blue dashed).

4.2 Control Experiments

In the 100 year free run shown in Figure 4.2(a), seven El Niño events are identified as strongly influenced by the MJO based on the events having the greatest variability in the $W_{MJO,K}$ index, $+N_{MJO,K}$ (marked by squares), and seven El Niño events are identified as weakly influenced by the MJO based on the events having the weakest variability in the $W_{MJO,K}$ index, $-N_{MJO,K}$ (marked by circles). There are 6 other El Niño events with $W_{MJO,K}$ index variability falling between the upper and lower terciles selected for these composites, for a total of 20 El Niño events during the 100 year run, giving an average El Niño period of 5 years. These weakly and strongly influenced events are simulated in this study using the ZCocn model and referred to as the control runs, with Sctl corresponding to $+N_{MJO,K}$ cases and Wctl to $-N_{MJO,K}$. For each of these cases, the model is forced using the Pacific basin-wide wind stress anomalies about the daily climatology of SP-CCSM4 and initialized on January 1 prior to each El Niño. Each run is twelve months long and consists of eleven ensemble members. Each ensemble member is initialized using wind stress data from ± 5 days about January 1. The same ocean initial conditions from January 1 of the El Niño year are used for each ensemble member. For all the following figures, the ensemble average of the 11 members is taken for each event within each case, then a composite is created by averaging all seven events.

Contrasting features between the Sctl and Wctl runs elucidates the mechanisms controlling the rapid and strong growth of El Niño events with strong MJO influence. Figure 4.3 shows the Kelvin wave component of thermocline depth anomaly and total thermocline depth anomaly of the strong and weak control cases. The Kelvin wave component of thermocline depth anomaly is determined analytically by the ocean dynamics as a response to wind stress forcing, with thermocline depth anomalies and surface currents being the sum of the Rossby and Kelvin wave contribution to each. ZCocn computes anomalies around a monthly climatological state for SST and thermocline depth anomaly, meaning anomalous values are output natively every ten days (the monthly climatology is interpolated to the

ten day period by the model). The most prominent feature of Kelvin wave activity is the growth of very strong downwelling Kelvin wave activity east of the dateline in the latter half of the year, associated with the growth of the strong El Niño in Sctl, contrasted with the considerably weaker activity during the same period in Wctl. Throughout the first six months of the year, downwelling Kelvin wave activity dominates in the central and eastern Pacific in Sctl. This stands in contrast to the same period in Wctl, where although significant downwelling activity is seen, there are brief periods of predominant upwelling Kelvin wave activity propagating eastward from the western Pacific.

Later in the year, as the El Niño approaches its peak, the thermocline depth anomalies shown in Figures 4.3(c) and (d) display broadly similar features between Sctl and Wctl, albeit with a slightly smaller amplitude in Wctl. That is, shallow thermocline anomalies are seen in the western Pacific and deep thermocline anomalies are seen in the eastern Pacific, demonstrating the flattening of the tropical Pacific thermocline as is typical of El Niño. The development of this flattened thermocline occurs earlier in the year in Sctl than in Wctl, in March and May, respectively, as highlighted in Figures 4.3(c) and (d).

Upwelling Rossby waves are also seen in each composite (Figure 4.3(c), (d)), but their activity in Wctl (Figure 4.3(d)) is of higher frequency and higher wave number in the first six months. The initial ocean state of the events in this composite could contribute to this feature, as much of the Rossby wave activity seems to originate prior to the run initialization. Rossby wave activity in Wctl causes a delay of a persistent flattening of the thermocline. By contrast, in Sctl the upwelling Rossby wave signal that arrives in the western Pacific in April actually facilitates the flattening of the thermocline. Rossby wave reflection could also be a significant source of Kelvin wave activity, as we see the development of significant downwelling Kelvin wave signals in the western Pacific simultaneous with the arrival of this upwelling Rossby wave signal.

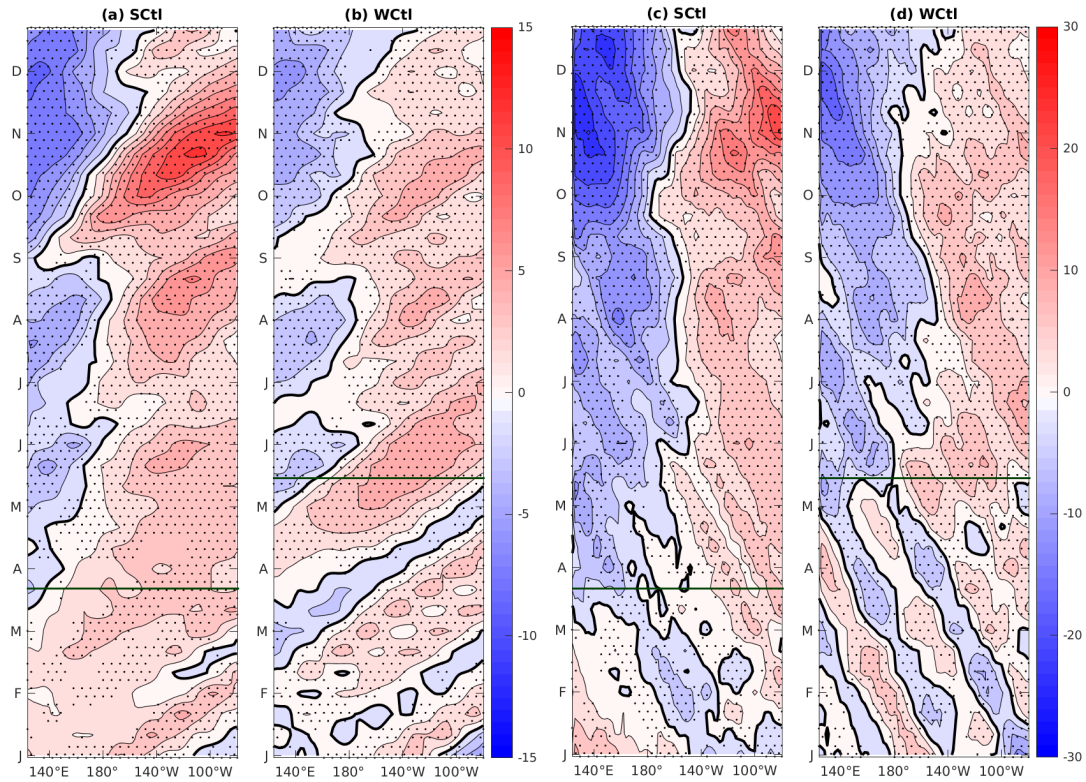


Figure 4.3: Ensemble average composite of equatorially ($5^{\circ}\text{S} - 5^{\circ}\text{N}$) averaged: a) – b) Kelvin wave component of thermocline depth anomaly and c) – d) total thermocline depth anomaly for strong (Sctl) and weak (Wctl) control cases. Positive (negative) values indicate downwelling (upwelling) Kelvin waves and an anomalously deep (shallow) thermocline. The thick contour is the zero isoline. Stippled regions indicate composite regions that are significantly significant at the 95% level using a two-tailed Student’s t-test. The green lines indicate the time after which the flattened, El Niño-like thermocline has emerged and persists throughout the rest of the year. Units are meters.

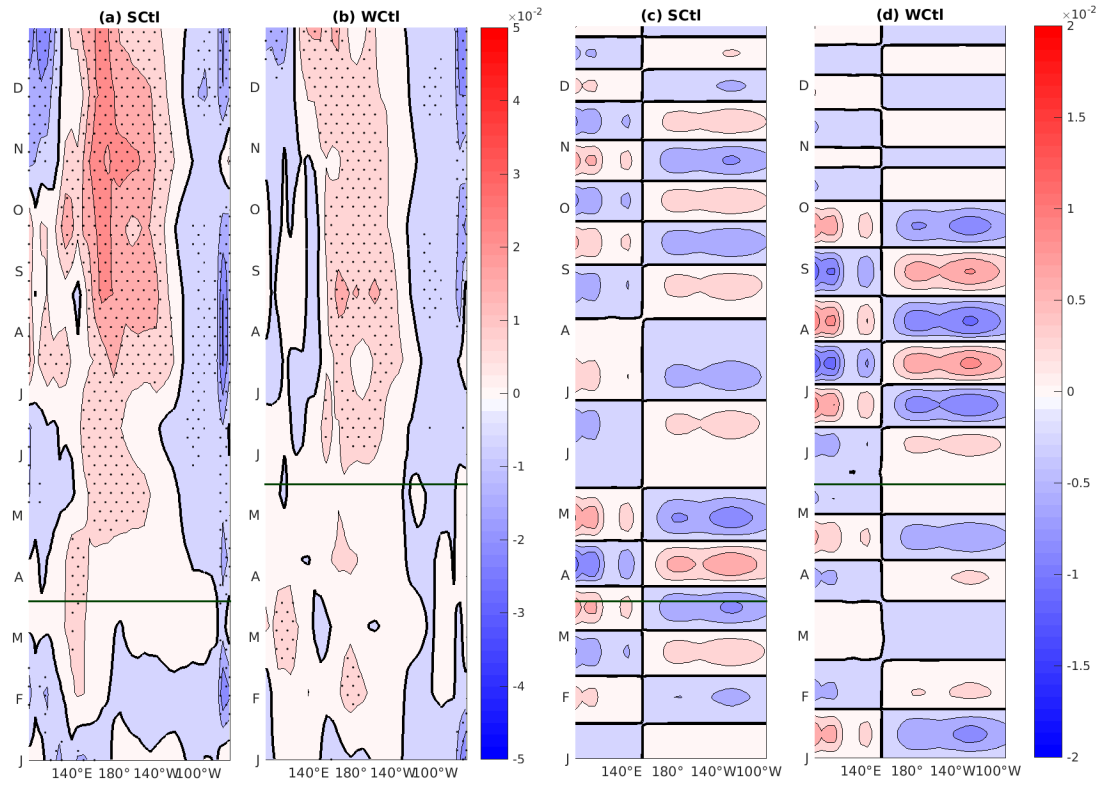


Figure 4.4: Ensemble average composite of equatorially ($5^{\circ}\text{S} - 5^{\circ}\text{N}$) averaged: a) – b) zonal wind stress anomalies and c) – d) zonal MJO wind stress (τ_{MJO}) for strong (Sctl) and weak (Wctl) control cases. Positive (negative) values indicate westerly (easterly) wind stress anomalies. The thick contour is the zero isoline. Stippled regions of total wind stress anomaly indicate composite regions that are statistically significant at the 95% level using a two-tailed Student’s t-test. The green horizontal lines correspond to those on Figure 4.3, after which the flattened, El Niño-like thermocline has emerged and persists throughout the rest of the year. Units are $N \cdot m^{-2}$.

Also contributing to the development of the flattened thermocline are westerly wind anomalies, which begin to dominate the western Pacific in Sctl in February and continue to grow in strength and zonal extent throughout the year (Figure 4.4(a)). Although some patches of significant westerly anomalies are seen in Wctl (Figure 4.4(b)), a persistently significant westerly signal is not seen until after the thermocline has flattened. Higher frequency and relatively strong amplitude MJO activity develops prior to the end of March in Sctl, and thus leads the flat thermocline by a month. Higher frequency and strong amplitude MJO activity does not develop in Wctl until June/July, and thus lags the flat thermocline by a month. Comparing Figures 4.4(c) and (d) demonstrate significant differences between the MJO wind stress computed in SP-CCSM4 compared to that computing for observations, shown in Figure 2.6. SP-CCSM4 MJO wind stress shows what look to be standing oscillations, while clear propagation of wind stress anomalies is seen in observations. This could be due to the 100 years included in the calculation for SP-CCSM4, which allows for more clearly defined regions to dominate. It may also be related to the interpolation required for implementation into ZCocn, which may wash out some spatial variability in τ_{MJO} . In any case, some general features are retained between each. The Sctl composite shows the development of relatively lower amplitude, lower frequency MJO wind stress than seen in Wctl, although this higher frequency and higher amplitude activity doesn't occur until the summer in SP-CCSM4. This is consistent with the finding that lower frequency MJO activity can more strongly affect the state of the ocean.

The thermocline evolution in the two cases gives rise to differing SST evolutions as well. Figure 4.5 compares SST anomalies for Sctl and Wctl. Each case shows the growth of a positive anomaly from the beginning of the year centered around 130°W. In Sctl, the SST anomalies along the dateline grow more rapidly, becoming positive a few months before Wctl, and the SST anomalies exceed 0.2°C considerably earlier in the year in the western equatorial Pacific in Sctl. The SST anomalies of Wctl also cease growing earlier in the year than in Sctl. Perhaps the most prominent feature of Figure 4.5 is that Sctl reaches its peak in winter and about 10° east of the peak anomalies in Wctl which occur

at the end of summer (indicated by the black boxes). Downwelling Kelvin wave activity dominates ocean dynamics in SCtl, while WCtl is interspersed with periods, albeit brief, of upwelling predominance in Kelvin wave activity, as well as high frequency Rossby wave propagation resulting in the delayed onset of significant eastern Pacific SST anomalies in WCtl by several months as compared to SCtl. This delayed onset can be attributed to destructive interference between high frequency waves that makes the overall state of the thermocline transient-like until later in the year. The buildup of this state months earlier in SCtl corresponds quite well to the relative timing of positive SST anomaly growth in SCtl and WCtl.

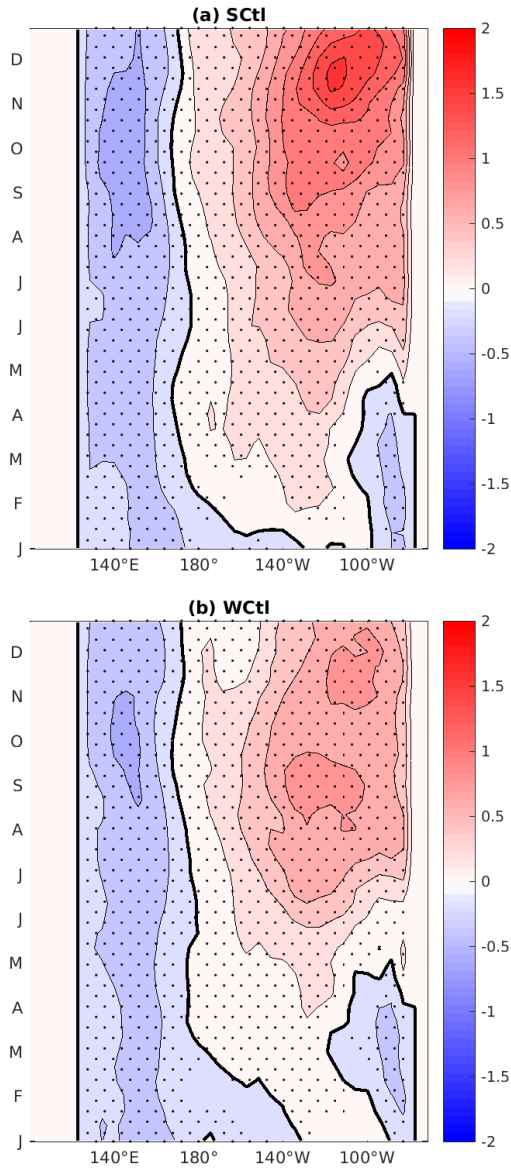


Figure 4.5: Ensemble average composite of equatorially ($5^{\circ}\text{S} - 5^{\circ}\text{N}$) averaged SST anomaly for Sctl (top) and Wctl (bottom). The thick contour is the 0°C isotherm. Stippled regions indicate composite regions that are statistically significant at the 95% level using a two-tailed Student's t-test. The boxes indicate the timing and longitude of maximum SST. Units are $^{\circ}\text{C}$.

There are several features differentiating Sctl from Wctl. First, the flattened thermocline state occurs earlier in Sctl than in Wctl, coinciding with significant westerly wind anomaly development and more frequent, higher amplitude MJO activity development in each. Second, in Wctl there are periods of predominant upwelling Kelvin wave activity which are coincident with easterly wind stress that do not occur in Sctl. Finally, in Sctl peak SST anomalies occur later in the year and further to the east than in Wctl, consistent with the observational analysis performed in Chapter 2. These composites are developed based on the relative contribution of the MJO on the evolution of the oceanic state. Features separating these composites have been identified, but the mechanistic source of these features has not. Sensitivity experiments on these control runs are now necessary to discern if and how the MJO wind stress contributes to the development of these features.

4.3 Sensitivity Experiment Description

Two complementary sets of experiments are conducted. In the first set, the wind stress is modified and the response of the dynamic state of the ocean and SST is analyzed. In the second, oceanic Kelvin waves are modified and the response of SST is analyzed. For each experiment, 11 lagged ensemble members are created for each El Niño in $+N_{MJO,K}$ and $-N_{MJO,K}$ at ± 5 day lag (like the control runs) to improve robustness of results. All figures shown in this chapter are based on composites of ensemble averages for each case.

In the first experiment, the model is initialized on January 1 and run until December 31 of each of the seven El Niño years corresponding to the $+N_{MJO,K}$ cases. During this run, the westerly wind stress associated with the MJO is removed from the wind stress forcing applied to ZCocn (NMJO_Sctl) to identify the direct effect of the MJO wind stress for these cases. The selection of westerlies is motivated by the findings of Roundy and Kiladis (2006) and Seiki et al. (2009), who have shown that in the year leading up to an El Niño event, westerly winds have a stronger influence on the state of the ocean than do easterlies of similar amplitude. A similar experiment was performed wherein both easterly and westerly

MJO wind stress was removed, which resulted in alternating positive and negative eastern Pacific SST anomalies that ultimately cancelled each other out.

Two experiments are carried out on the seven El Niño years corresponding to the $-N_{MJO,K}$ cases. These runs are initialized on January 1 of the year preceding the El Niño and run until December 31 of the same year. In the first of these experiments, westerly wind stress associated with the MJO during these runs is doubled (MJO2x-WCtl). This experiment is designed to address whether increasing the amplitude of the MJO forcing for $-N_{MJO,K}$ events can replicate the differentiating features seen between them and $+N_{MJO,K}$. In a second experiment on $-N_{MJO,K}$, the MJO associated westerly wind stress from the El Niño event for which the $W_{MJO,K}$ index is the strongest is applied to $-N_{MJO,K}$ (SMJO-WCtl). This experiment allows for the quantification of the effect of strong MJO activity identified as strongly affecting the oceanic state on the development of an El Niño with different ocean conditions and different total wind stress anomalies. By comparing the effects of these two experiments on the oceanic state, conclusions can be drawn regarding the features of MJO wind stress most important for the development of the features differentiating WCtl and Sctl.

A pair of experiments are also performed to determine the effect of directly modifying Kelvin wave activity in the ocean. Specifically, these experiments aim to determine if modifying the phasing of Kelvin wave activity with respect to the MJO associated wind stress can reproduce the features discussed in Section 4.2. In these experiments, each of the seven $+N_{MJO,K}$ ($-N_{MJO,K}$) cases are modified by reversing the sign of downwelling (upwelling) Kelvin wave activity that passes into the $W_{MJO,K}$ region while in (out of) phase with the MJO associated wind stress in that region. That is, if MJO wind stress in the $W_{MJO,K}$ region is predominantly westerly and the Kelvin wave entering this region from the west is downwelling (upwelling), the sign of that Kelvin wave is reversed to break (impose) that phased relationship. These artificial phase reversals force Kelvin waves in Sctl to be out of phase with τ_{MJO} , and force Kelvin waves in WCtl to be in phase with τ_{MJO} . The experiment performed on $+N_{MJO,K}$ ($-N_{MJO,K}$) cases is labeled

Table 4.1: Summary of control and sensitivity experiment design and nomenclature.

| Experiment | Description | Control |
|---------------|----------------------------------------------------------------------------------------------------------|---------|
| SCtl | Strong case control run | -- |
| WCtl | Weak case control run | -- |
| NMJO_SCtl | Westerly τ_{MJO} removed from forcing | SCtl |
| SPhasing_SCtl | Downwelling Kelvin waves are reversed when simultaneous with westerly τ_{MJO} in $W_{MJO,K}$ region | SCtl |
| SMJO_WCtl | Westerly τ_{MJO} from strongest event added to forcing | WCtl |
| MJO2x_WCtl | Westerly τ_{MJO} doubled | WCtl |
| WPhasing_WCtl | Upwelling Kelvin waves are reversed when simultaneous with westerly τ_{MJO} in $W_{MJO,K}$ region | WCtl |

SPhasing_SCtl (WPhasing_WCtl). If it can be shown that composites of field variables in SPhasing_SCtl (WPhasing_WCtl) are drawn toward those of WCtl (SCtl), then it is reasonable to conclude that the relative phasing of Kelvin waves and MJO wind stress contributes to the development of each set of events. That is, a coherent phase or resonance between the MJO and Kelvin waves produces stronger events than a decoupled phasing. A summary of numerical experiments carried out in this chapter is presented in Table 4.1.

4.4 Sensitivity Experiment Results

4.4.1 MJO Forcing Modification

The wind stress modification experiments carried out here quantify the effect of removing the MJO wind stress from SCtl and adding the MJO wind stress to WCtl, in order to discern the effect of the MJO wind stress on the features differentiating these control runs. Figure

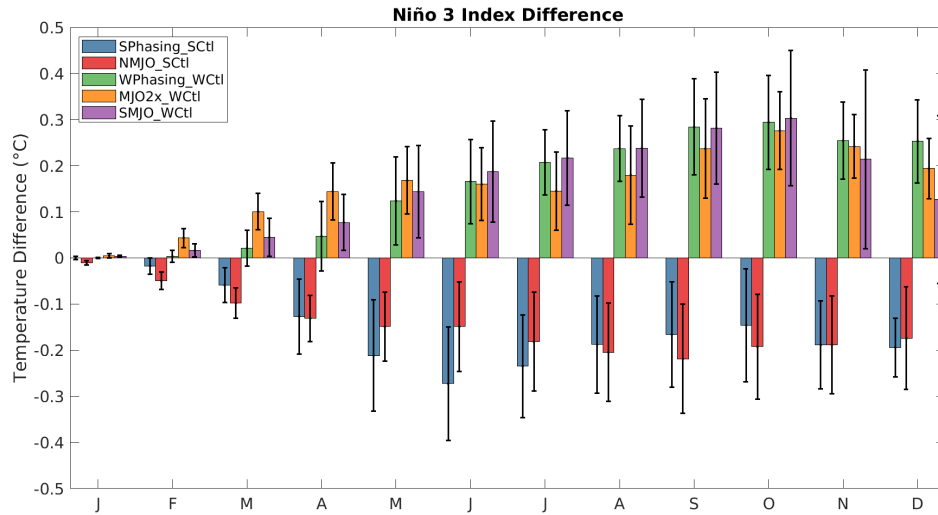


Figure 4.6: Ensemble average composite of the Niño 3 index time series difference between each sensitivity experiment and their respective control experiment. Each set of five bars represents a monthly value for each experiment, with the blue bar as the leftmost value for each month. The shaded areas show $\pm 1\sigma$ computed across events and ensemble members.

4.6 shows the composite difference in Niño 3 index time series between each of the five experiments and the control run. The removal of westerly anomalies associated with the MJO results in a reduction of the Niño 3 index of about 0.2°C in the latter half of the year, albeit slightly more modest than the two experiments on WCtl, which show an increase of around 0.3°C at the peak of the event in autumn. In MJO2x_WCtl SST anomalies grow quite rapidly early in the year, before decreasing in the summer, finally increasing toward the peak of El Niño. SMJO_WCtl shows more gradual growth of SST anomalies until the spring, after which SST anomalies of SMJO_WCtl exceed those in MJO2x_WCtl and show consistently rapid growth until reaching a stronger peak. This suggests that the forcing of the SMJO_WCtl experiment projects more strongly onto the mean Kelvin wave state than does the forcing contained within each composite in WCtl, which despite being doubled in MJO2x_WCtl, do not produce as much of a response as the forcing introduced in SMJO_WCtl.

ZCocn is a shallow water model, thus making it difficult to calculate APE. However, due to the fidelity of El Niño events in ZCocn and the known relationship between W , APE, and Niño 3 (which was also shown in Chapter 3 for SP-CCSM4), discussions of APE will be foregone. Figure 4.7 shows the difference in total wind power between each experiment and the control. Here we see a consistent reduction in W for the weak case experiments and a consistent increase in W for the strong case experiments. Because values of W are generally negative during El Niño development in SP-CCSM4 composites (Figure 3.7), positive (negative) differences correspond to a reduction (increase) in W magnitude. MJO2x_WCtl shows stronger W development than WCtl in the spring due to the doubling of westerly MJO-related wind stress in this experiment, consistent with the more rapid increase in Niño 3 during this period. By the summer, SMJO_WCtl has surpassed MJO2x_WCtl, and this remains true for several months, again consistent with the more rapid growth of Niño 3 seen in SMJO_WCtl during this period. Because the methodology of MJO2x_WCtl only enhanced westerlies that are already present, the coherence between the MJO and Kelvin wave activity is not affected, whereas in SMJO_WCtl new episodes of westerly forcing from the event most influenced by the MJO are introduced, which could affect the phasing. These results further motivate the Kelvin wave modification sensitivity experiments, discussed in Section 4.4.2.

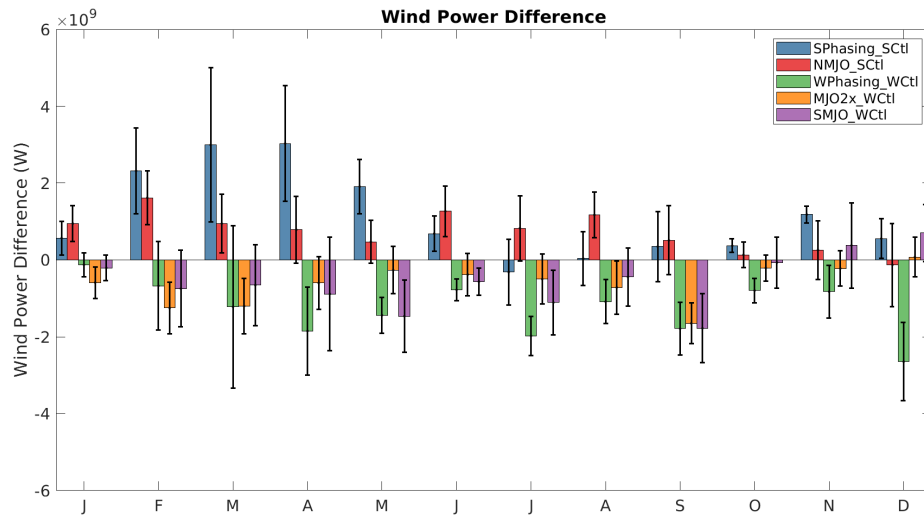


Figure 4.7: As with Figure 4.6, but for wind power.

These changes in W should also reflect changes to Kelvin wave activity. Figure 4.8 shows the difference in the Kelvin wave component of thermocline depth anomaly between each experiment and the control. Anomalous upwelling (downwelling) compared to the control is seen in the eastern Pacific throughout the year in NMJO_SCtl (SMJO_WCtl/MJO2x_WCtl). In the western Pacific, the opposite is seen, with anomalous downwelling (upwelling) in NMJO_SCtl (SMJO_WCtl/MJO2x_WCtl). The most significant response of the Kelvin wave activity in MJO2x_WCtl occurs early in the year, with strong downwelling anomalies in the eastern Pacific simultaneous with the rapid growth of the Niño 3 index. In the summer, the response of the ocean in MJO2x_WCtl is dominated by the western Pacific upwelling signals, reaching as far east as 140°W . The eastern Pacific response is largely suppressed during this period, simultaneous with a reduction of the Niño 3 index. Similarly, strong eastern Pacific downwelling anomalies are seen during early summer in SMJO_WCtl, simultaneous with the most rapid growth of the Niño 3 index for this experiment. Later in the year, some significant downwelling anomalies are seen as well, but the similarities during this period seen in both MJO2x_WCtl and SMJO_WCtl indicate that these are likely

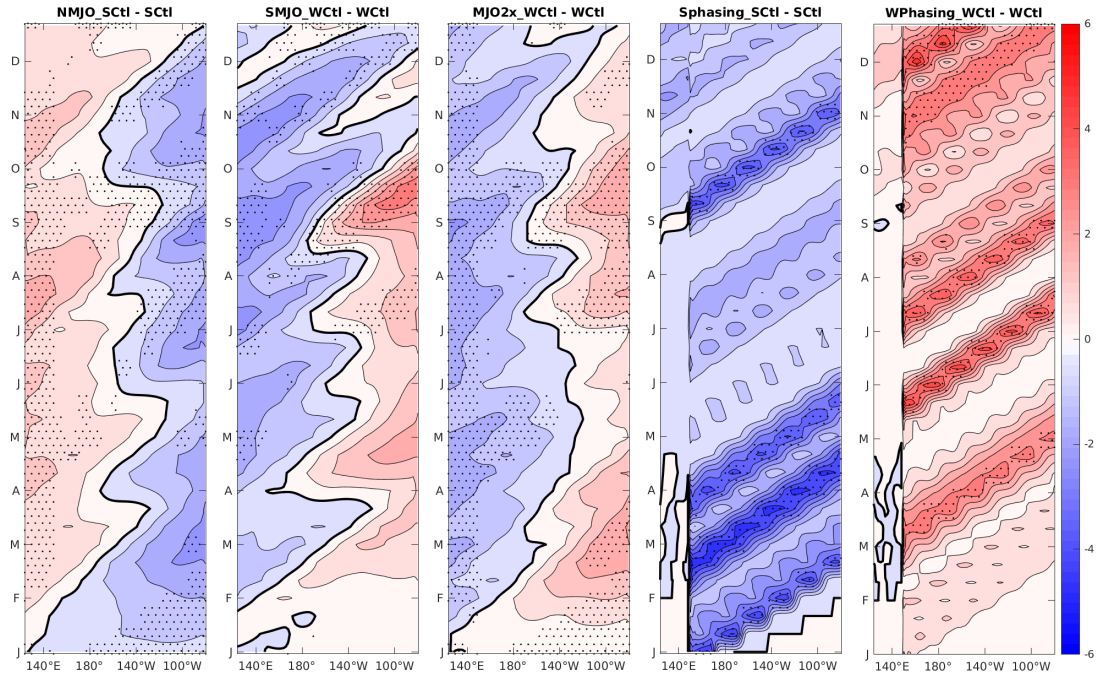


Figure 4.8: Ensemble average composite difference in Kelvin wave component of thermocline depth anomaly between each experiment and the control. The thick contour is the zero isoline and the vertical dash lines delineate the longitudes of the $W_{MJO,K}$ region. Stippled regions indicate composite regions that are statistically significant at the 95% level using a two-tailed Student's t-test. Units are meters.

due to the response of the MJO forcing to the growth of the El Niño in SP-CCSM4. It is important to note that the flattened thermocline state discussed at the end of Section 4.2 is closely reflected in changes to Kelvin wave activity seen in Figure 4.8. NMJO_Sctl shows a weakening of this state (consistent with the removal of westerly MJO wind stress), while SMJO_Wctl and MJO2x_Wctl both show a strengthening of this state (consistent with the addition of westerly MJO wind stress).

4.4.2 Kelvin Wave Modification

The second set of sensitivity experiments focus on altering the phasing between the MJO wind stress and Kelvin wave activity via the reversal of Kelvin wave phase. In Figure 4.6, there is a notable correspondence between WPhasing_WCtl and SMJO_WCtl Niño 3 index, suggesting at least some features of the MJO wind stress in the strongest event is captured by altering the phase of Kelvin wave activity in WPhasing_WCtl, in agreement with the similar evolution of W . SPhasing_SCtl shows a stronger decrease in Niño 3 than NMJO_SCtl until autumn, accompanied by a greater reduction in the magnitude of W until the end of summer.

The Kelvin wave difference between the experiments and control shown in Figure 4.8 reveal the nature of SPhasing_SCtl and WPhasing_WCtl changes to the El Niño events. In SPhasing_SCtl, there are strong reductions to the predominant Kelvin wave activity seen in the first half of the year in SCtl, indicating that this is a period when the MJO wind stress is predominantly westerly. There are weaker reductions in the Kelvin wave activity from the summer into autumn, then there is a considerable weakening of the very strong downwelling Kelvin wave activity seen at the peak of the event in SCtl. The fact that the predominant Kelvin wave activity seen in SCtl propagating from the western boundary in the summer to the eastern boundary is not strongly affected by SPhasing_SCtl indicates that the MJO is in its easterly phase during this period, and probably does not contribute significantly to the growth Kelvin wave activity during this period. Altogether, three periods of predominant downwelling Kelvin wave activity pass through the $W_{MJO,K}$ region in the first three months of the year in SCtl during periods in which the oceanic response is dominated by westerly MJO wind stress, and this activity serves to enhance the Niño 3 index during the growth of El Niño. In SPhasing_SCtl, the reversal of this activity serves to drastically reduce W magnitude until the end of summer, when this experiment briefly shows an increase in W magnitude. Interestingly, SPhasing_SCtl is the only experiment wherein the maximum effect on Niño 3 occurs during the summer instead of during autumn. This may suggest the importance of the nonlinear wind response to the evolving ocean state to the growth of

El Niño (e.g. Kessler and Kleeman, 2000), which is not captured here due to the prescribed wind stress forcing. In March, the predominant upwelling signal seen in Figure 4.3 in WCtl is reversed, as is the relatively weak upwelling signal originating at the western boundary at the beginning of the year. These reversals serve to bring the Kelvin wave intensity closer to SCtl by removing interruptions to the growth of significant thermocline depth anomalies in the eastern tropical Pacific. In fact, it is difficult to pick out any strong upwelling signals in WCtl that are not reversed in WPhasing_WCtl, indicating that each of these periods is coincident with periods of predominant westerly MJO wind stress. The phasing of Kelvin wave activity and MJO wind stress will be discussed further in Section 4.5.

4.5 Discussion

In this study, the oceanic component of the Zebiak-Cane (ZCocn) model is forced by wind stress from SP-CCSM4, a model shown to have a reasonable simulation of the MJO and ENSO. SCtl composites show earlier onset of the flattened El Niño thermocline state, fewer periods of predominant upwelling Kelvin wave activity, and peak SST that is of greater amplitude, later in the year, and further to the east than in WCtl. These composites also reveal this thermocline flattening to be associated with the development of persistent westerly wind anomalies. Sensitivity experiments on these events demonstrate the importance of the MJO to the development of these features, especially the early onset of the flattened thermocline. Figure 4.6 shows a close correspondence between SMJO_WCtl and WPhasing_WCtl despite the very different methods applied to these sensitivity experiments. A possible explanation is presented here. By applying westerly MJO forcing from an event that does not exist in WCtl, we enhance the effective likelihood that westerly MJO phases are simultaneous with downwelling Kelvin wave activity. In WPhasing_WCtl, coherence between MJO phase and downwelling Kelvin wave activity is directly enhanced. SMJO_WCtl and WPhasing_WCtl thus result in similar Niño 3 (Figure 4.6) and wind power (Figure 4.7) trajectories due to the encouragement of the same phasing relationship in each experiment.

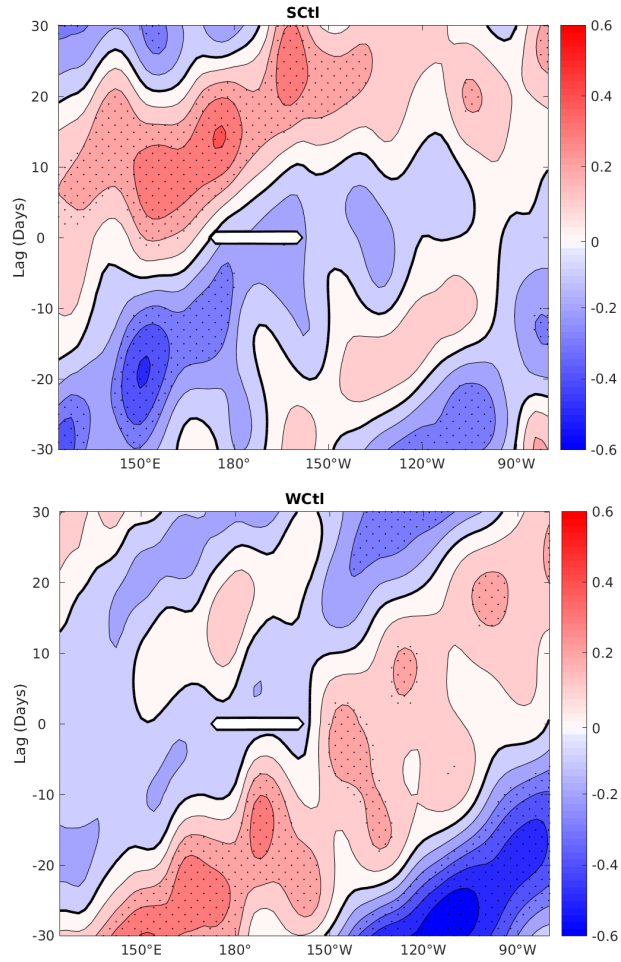


Figure 4.9: April – May – June lag correlation between zonal MJO wind stress in the $W_{MJO,K}$ region and Kelvin wave component of thermocline depth anomaly averaged between 5°S and 5°N for Sctl (top) and Wctl (bottom). The white bar indicates the $W_{MJO,K}$ region at zero lag, the region for which the correlation is computed. Negative (positive) lags indicate Kelvin wave activity leading (lagging) MJO wind stress. Stippling indicates correlation significance at the 95% level.

The phase relationship between the MJO and oceanic Kelvin waves can be revealed by lag-correlation analysis. Figure 4.9 shows the April – May – June lag correlation between the MJO wind stress averaged over the $W_{MJO,K}$ region ($1^{\circ}\text{S} - 3^{\circ}\text{N}$ and $175^{\circ}\text{E} - 160^{\circ}\text{W}$) and the Kelvin wave component of thermocline depth anomaly averaged between 5°S and 5°N for Sctl and Wctl. The correlation is plotted as a function of longitude across the Pacific basin. Seasonal composites were made for the rest of the year as well, revealing little coherence in either case for January – February – March and little difference between cases in the second half of the year. This figure shows that for Sctl, MJO activity is preceded by Kelvin wave activity of opposite sign and followed by Kelvin wave activity of the same sign. In AMJ for Sctl, westerly MJO wind stress over the $W_{MJO,K}$ region is preceded by upwelling Kelvin wave activity in the western Pacific and followed by downwelling Kelvin waves that expand progressively into the eastern Pacific. The upwelling shoals the thermocline in the western Pacific whereas the downwelling deepens the thermocline and increases the SST in the east (Wang, 2001). The significant correlation at negative lags suggests that the Kelvin waves are not necessarily excited by the MJO wind forcing. In Wctl, the opposite is found, and the Kelvin wave activity following the MJO is only insignificantly related to the MJO activity, and thus is either coincidental or a weak response. This indicates a coherence between the MJO and Kelvin wave activity in Sctl that is not seen in Wctl.

This evidence demonstrates the importance of MJO – Kelvin wave coherence to strong El Niño development. However, the results shown in Figure 4.8 indicate that the MJO is not the primary source of the Kelvin wave activity seen in Figure 4.3, because the mean amplitude of Kelvin wave activity in NMJO_Sctl is reduced by only 40% of the mean amplitude in Sctl. This indicates that the MJO can amplify Kelvin waves that would have been produced by ocean dynamics such as Rossby wave reflection off the western boundary of the tropical Pacific basin or other sources of wind variability. However, in our experiments, the MJO is not forcing them directly. The simplicity of ZCocn may prevent this model from exciting Kelvin waves in response to MJO forcing as has been shown in observations (e.g. Hendon et al., 1998; McPhaden and Yu, 1999) and an ocean model with increased complexity may

capture this aspect. Nevertheless, the results of this study indicate that while MJO forcing can significantly affect El Niño timing and strength, it is not the triggering mechanism for El Niño events. With respect to the ENSO theory paradigms discussed in Section 1.1, the results of this study imply ENSO falls into the second paradigm. That is, that ENSO is a self-sustained and periodic oscillatory mode for which atmospheric forcing provides the observed irregularity and aperiodicity.

Unlike previous studies in the literature that focus on individual El Niño events, in this study results are based on statistics of El Niño events. In any case, coherent phasing between MJO wind stress and Kelvin wave activity is shown to be an important facilitator of MJO-ENSO interactions. This would also explain the features separating WCtl from SCtl discussed at the end of Section 4.2. The zonal fluctuations in the thermocline seen in Figure 4.3 for WCtl indicate inconsistent thermocline activity in the composite, inhibiting the development of the thermocline response seen in SCtl and resulting in less consistent El Niño strength. The thermocline response of SCtl after the spring facilitates the interaction between the MJO and Kelvin wave activity earlier in the year, as supported by Figure 4.9.

It is shown in Chapter 2 that τ_{MJO} in El Niño events which are not influenced by MJO (1991, 2004, and 2014) is of relatively large amplitude but high frequency, which inhibits that wind stress from influencing the ocean (Hendon et al., 1998). Here, the SCtl composite shown in Figure 4.4(a) shows higher frequency than the WCtl composite in (b), but this frequency is still lower than that of Figure 2.6(b), and so τ_{MJO} is still able to project onto the Kelvin wave state. Furthermore, WCtl shows high frequency τ_{MJO} developing later in the year, consistent with the higher frequency MJO activity seen in Figure 2.6(b). These results are thus consistent with the findings regarding the relationship between $W_{MJO,K}$, Kelvin wave activity, and El Niño development in Chapter 2.

Chapter 5: ENSO Prediction with EOF-Derived Indices

Chapter 4 suggests that the primary source of the MJO-Kelvin wave-ENSO relationship is the coincident phasing or resonance between westerly wind anomalies due to MJO activity and downwelling Kelvin waves during April-May-June (AMJ). This resonance is likely impossible if the MJO activity is of too high frequency, as in observations it is seen that although significant τ_{MJO} activity is seen in events determined by $W_{MJO,K}$ to not be influenced by the MJO, that activity does not project onto the Kelvin wave state. The source of the oceanic Kelvin waves can be direct excitation from MJO wind anomalies (McPhaden 1999) or produced by internal ocean dynamics and amplified by τ_{MJO} .

The previous chapters have focused on quantifying the relationship between the MJO and ENSO using the Kelvin wave activity as a mechanism linking them. The feedback mechanism between westerly MJO wind stress and the growth of positive SST anomalies in the central/eastern tropical Pacific has not been directly addressed. The first objective of this chapter is to develop a method for holistically representing the MJO-ENSO relationship by creating indices that incorporate the covariability of MJO wind stress, Kelvin wave activity, and SST anomalies that can be used for real-time applications. The second objective is to demonstrate the applicability of these indices to seasonal forecast systems for El Niño prediction. Development of these indices draws upon the empirical work shown in Chapter 3 (Lybarger and Stan, 2018), which introduced a method for quantifying the influence of MJO/Kelvin wave covariability on the growth and peak of El Niño.

5.1 Data and Methods

This chapter will perform analyses on precisely the same datasets as were used for the observational study in Chapter 2. The analyses done for observations are also performed

for the National Centers for Environmental Prediction (NCEP) Climate Forecast System, version 2 (CFS-v2) (Saha et al., 2013) reforecasts of each year during the period 1980-2014 (Huang et al., 2017). Each reforecast consists of five ensemble members initialized in April and run for three months, from which daily wind stress, surface currents, and sea surface temperature is retained. For further information on these reforecasts, see Huang et al. (2017).

5.1.1 MJO Wind Power

For real-time applications, the methodology used in the previous chapters cannot be used to compute the $W_{MJO,K}$ index because that methodology requires bandpass filtering and HSVD analysis to compute the MJO wind stress. A surrogate method must therefore be developed. In this real-time methodology for computing τ_{MJO} , the HSVD spatial patterns computed for observations are projected onto the unfiltered wind stress anomalies. Because these patterns are computed for intraseasonal wind stress anomalies, they should isolate at least some portion of the variability associated with intraseasonal timescales, even if they are projected onto unfiltered anomalies. The HSVD spatial patterns based on observations are shown in Figure 5.1. EOFs 1 and 2 display stronger amplitudes in the western Pacific, and a lesser basin wide influence. EOF3 shows a tripole pattern, with positive amplitudes along the western boundary north of the equator, negative amplitudes along the dateline that extend along the equator north to central America, and those eastern Pacific negative anomalies are flanked on the north and south by positive anomalies. EOF4 shows the opposite pattern for many regions when compared with EOF3, with a negative analog to the positive amplitudes seen along the western boundary north of the equator. A strong positive amplitude extends from the coast of New Guinea southeastward into the central Pacific, of opposite sign to the amplitudes seen there in EOF3. These EOFs are projected onto the unfiltered wind stress anomalies and combined, giving a proxy for τ_{MJO} that can be used for real-time applications. The computation of daily Kelvin wave-related surface current requires no change for real-time applications. Combining these terms gives a proxy

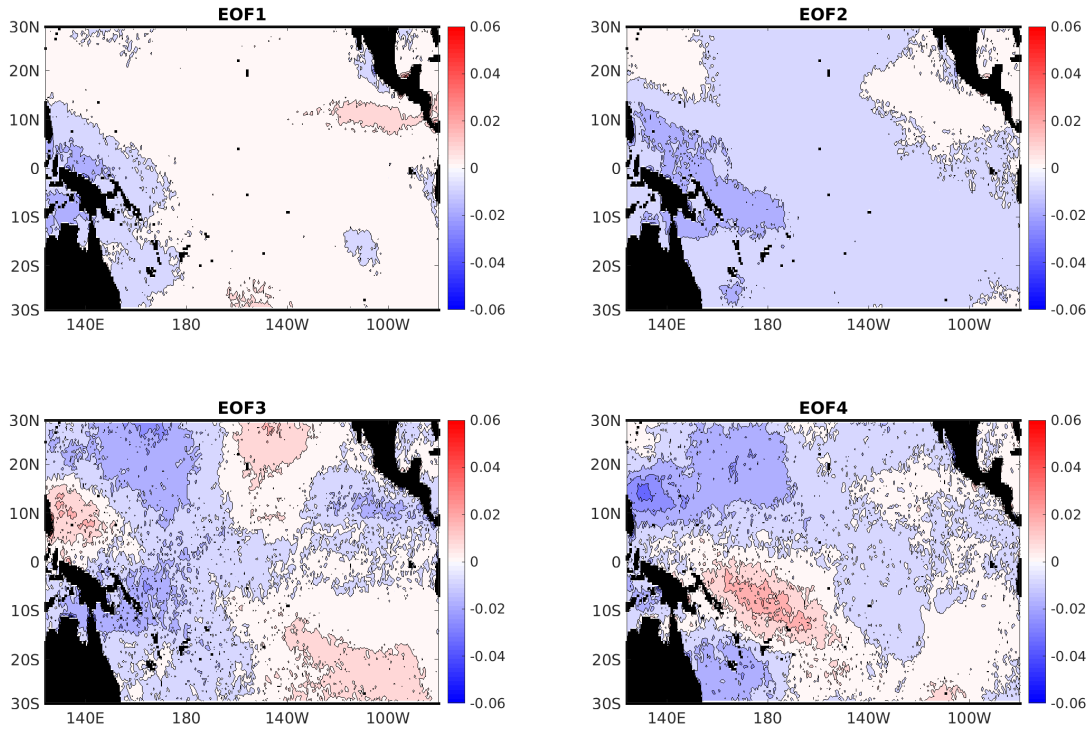


Figure 5.1: Amplitudes of EOFs resultant from HSVD analysis performed on observed intraseasonally bandpass filtered wind stress anomalies. Units are $N \cdot m^{-2}$

$W_{MJO,K}$. To compare the results of this method with the direct calculation, Figure 5.2 shows the correlation between the actual and proxy values of $W_{MJO,K}$ averaged between $5^\circ S$ and $5^\circ N$, computed independently for each year and zonal gridpoint. In this comparison the proxy values are computed by treating observations as forecasts. There is some disagreement between these terms, and that disagreement varies on interannual timescales. Because u_K is computed the same way for each, the difference must be due to the difference between the total wind stress anomalies and the intraseasonal anomalies.

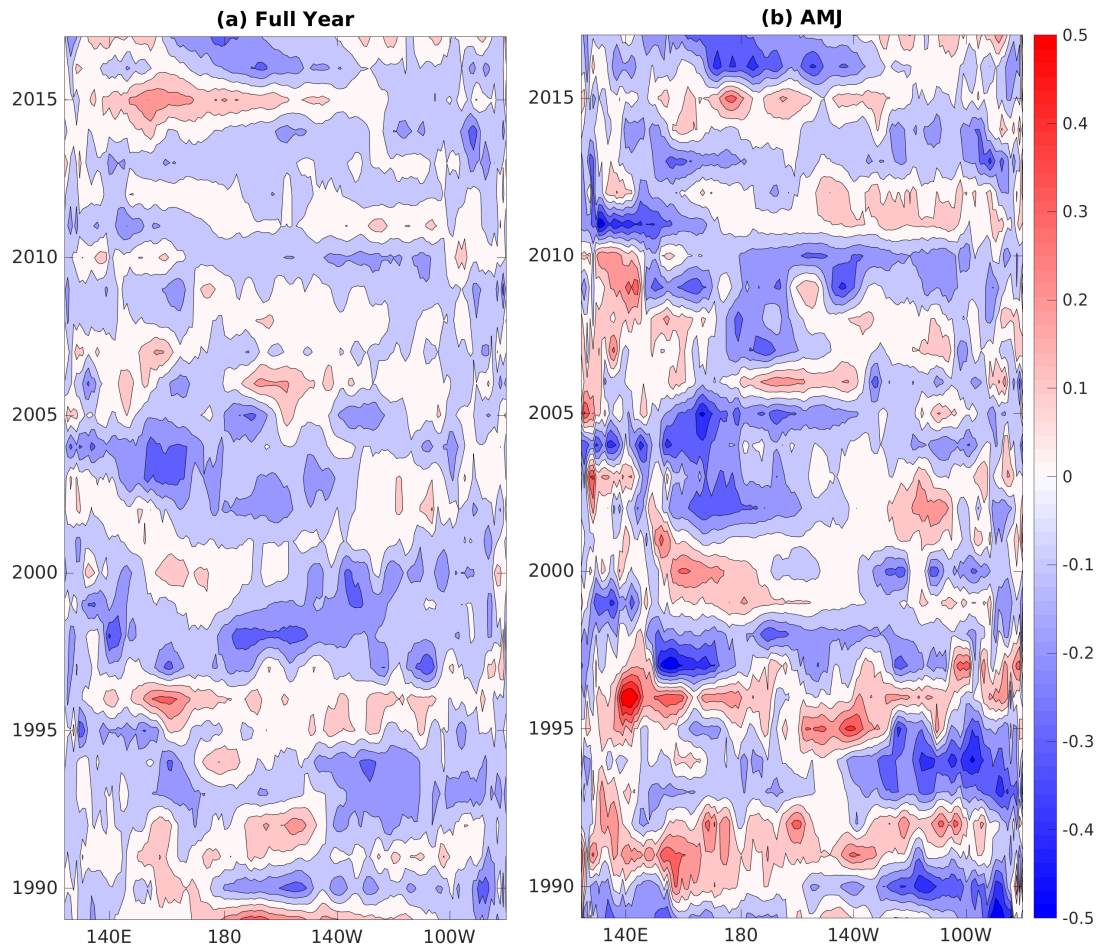


Figure 5.2: Hovmöller diagrams of correlation coefficients between actual $W_{MJO,K}$ and the proxy $W_{MJO,K}$. This correlation is computed for each year independently, for the full year (a) and for only the AMJ season (b).

5.1.2 EOF Analysis

Chapter 3 determined that El Niño events that are influenced by the MJO, defined as years with relatively high $W_{MJO,K}$ variance from January-July, show development of El Niño-like thermocline anomalies earlier in the year, stronger and more frequent Kelvin wave activity, and higher SSTs at the peak of the event than years for which $W_{MJO,K}$ has relatively low variance. However, when the $W_{MJO,K}$ index is computed for every year and used as a predictor, there is little skill in predicting El Niño events, consistent with the fact that the MJO and corresponding Kelvin wave activity occurs in varying strength irrespective of the presence of El Niño, and consistent with the idea that the MJO is not the primary initiator or driver of El Niño events.

To capture the covariability of MJO wind stress, Kelvin wave activity, and SST anomalies as an attempt to improve the prediction skill of this analysis, the multivariate empirical orthogonal functions (EOFs) of equatorially ($5^{\circ}\text{S} - 5^{\circ}\text{N}$) averaged values of $W_{MJO,K}$ and SST anomalies are computed. The zonal structure of the leading two EOFs of the combined fields of $W_{MJO,K}$ and SST anomalies are shown in Figure 5.3. EOF1 explains 30.8% of the daily variance and is dominated by variability in the SST anomalies. EOF2 explains 21.1% of the daily variance and is dominated by variability in $W_{MJO,K}$. EOF1 is reminiscent of ENSO variability, with a dipole structure between the western and central through eastern Pacific. EOF2, however, is very close to zero for much of the western Pacific and acquires increasingly strong positive amplitudes in the central and eastern Pacific, indicating the importance of these regions for SST and $W_{MJO,K}$ covariability. Figure 5.4 shows the daily PC amplitudes, normalized by their respective standard deviations as well as the time series of monthly Niño 3.4 index values along with the 9 El Niño events that occur during this period (1991, 1994, 1997, 2002, 2004, 2006, 2009, 2014, and 2015). Variability of PC1 and Niño 3.4 agrees quite well, while PC2 is dominated by variability in $W_{MJO,K}$, which varies on intraseasonal timescales. Highlighted in red are years identified by the $W_{MJO,K}$ index as being strongly influenced by the MJO (1997, 2006, and 2009). Consistent with Chapter

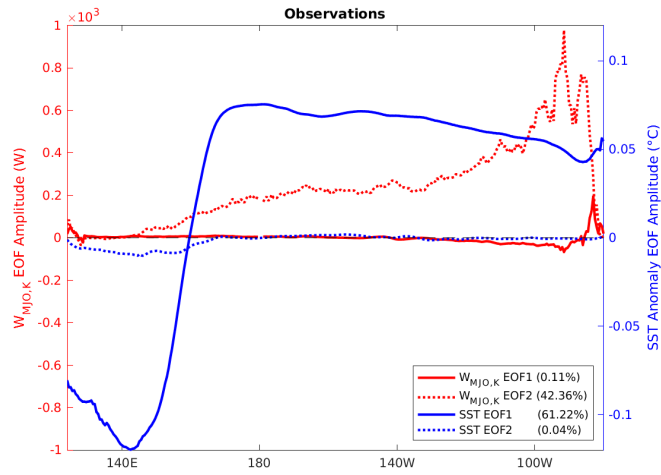


Figure 5.3: Multivariate EOF patterns of equatorially averaged ($5^{\circ}\text{S} - 5^{\circ}\text{N}$) $W_{MJO,K}$ (red) and SST anomalies (blue) in the tropical Pacific. Collectively, EOF1 (solid lines) explains 30.8% of the total daily variability and EOF2 (dotted lines) explains 21.1% of the total daily variability. Included in the legend is the fraction of each EOF explained by each variable.

3, El Niño events with a link to MJO activity show large variability of PC2. Interestingly, La Niña events are generally associated with small amplitudes and weak variability of PC2. Predictive indices have been computed using these PCs. Their derivation and results associated with them are discussed in Section 5.2.

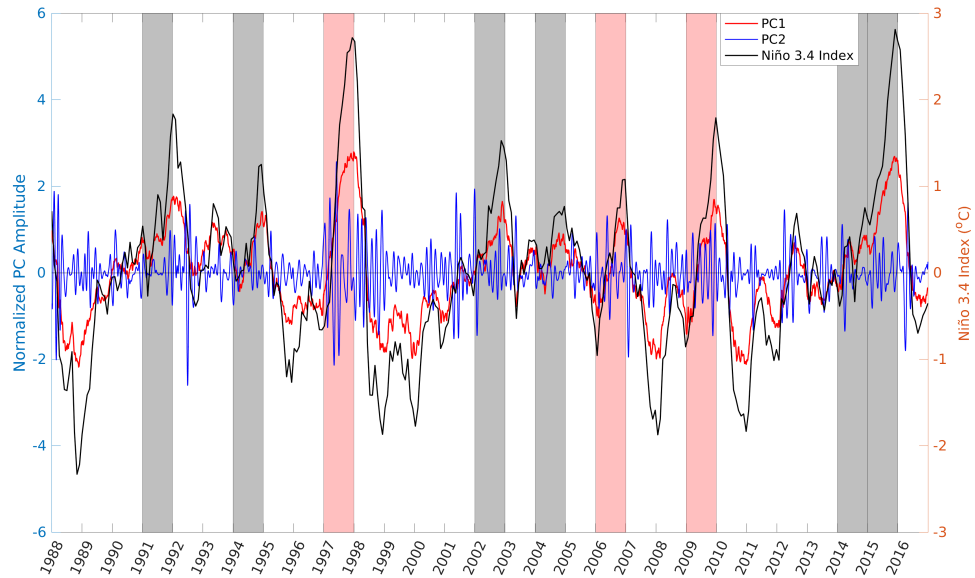


Figure 5.4: Normalized daily time series of PC1 (red) and PC2 (blue) from multivariate EOF analysis on equatorially ($5^{\circ}\text{S} - 5^{\circ}\text{N}$) averaged $W_{MJO,K}$ and daily SST anomalies. PC2 has been smoothed by a 30-day running mean filter. Monthly values of Niño 3.4 (black) are also shown to indicate that PC1 captures much of that variability. El Niño events throughout the time series are indicated by the background shading. Events which are strongly influenced by MJO by the criteria described in Chapter 3 are shaded in red (1997, 2006, and 2009), while the other El Niño events (1991, 1994, 2002, 2004, 2014, and 2015) are shaded in gray.

To approximate the multivariate PC time series for real-time applications, the spatial EOF patterns computed for observations (shown in Figure 5.3) are projected onto equatorially averaged SST anomalies and equatorially averaged values of the proxy $W_{MJO,K}$ described in Section 5.1.1. In each case, these equatorially averaged terms are normalized by the standard deviation of observations at each gridpoint. These PCs are then combined into indices and used as predictors of El Niño events in both observations and CFS-v2 reforecasts.

5.2 El Niño Predictors in Observations

In Chapters 2 and 3, it was shown that El Niño events strongly influenced by the MJO are associated with periods of high $W_{MJO,K}$ variability. To capture this relationship, an index is derived by combining the observational multivariate PCs described in Section 5.1.1 and shown in Figure 5.4. This index describes the covarying nature of MJO, Kelvin wave activity, and ENSO, and thus is called the *MaKE* index. It is defined as the minimum value of the linear combination of PC1 and $|PC2|$ over a 90-day period:

$$MaKE(t_m) = \min_{0 < t < 90} (PC1(t) + |PC2(t)|) \quad (5.1)$$

where t_m indicates monthly frequency and t indicates daily frequency beginning on the first day of each month. For example, the value of *MaKE* for April is the minimum value of $PC1(t) + |PC2(t)|$ on any day between April and June. Note that *MaKE* is defined only for each month whereas PC1 and PC2 are defined daily.

The index is intended to capture El Niño events, which are associated with positive values of PC1 (Figure 5.4) and negative values of W (Goddard and Philander, 2000; Hu et al., 2014; Lybarger and Stan, 2018), thus necessitating the absolute value for PC2 so that positive SST anomalies and negative values of W act in the same direction. Figure 5.5 shows the monthly time series of *MaKE* with El Niño years highlighted. A threshold value of -0.5σ for this index in April (i.e. the minimum over AMJ) is found, above which a given year is more likely to result in El Niño, and below which a given year is less likely to result in El Niño. When *MaKE* values are greater than -0.5σ , it means that either PC1 and therefore SST anomalies which are covarying with $W_{MJO,K}$ are consistently positive over this period (which would tend to suggest El Niño growth), or that negative/neutral SST anomalies are accompanied by consistently strong wind anomalies and Kelvin wave activity captured by $|PC2|$. The latter case could correspond to La Niña events, such as the events in 1995/96, 2005/06, and 2016/17. In those cases, Niño 3.4 is near zero in AMJ, but significant amplitudes of PC2 cause *MaKE* to identify these years as El Niño events.

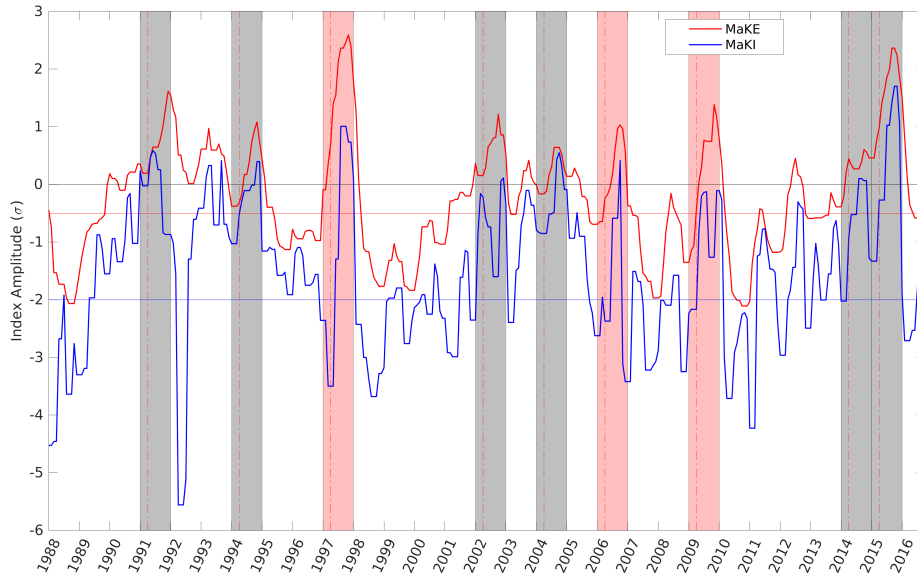


Figure 5.5: Time series of the *MaKE* (red) and *MaKI* (blue) indices in observations. El Niño years are highlighted by the background shading, with events that are strongly influenced by El Niño highlighted in red and all other events highlighted in gray. The -0.5σ (-2σ) threshold value for *MaKE* (*MaKI*) is shown by the horizontal thin red (blue) line. For each El Niño year, the month of April is indicated by the vertical dash-dotted red line because that is the month identified as having predictive power for these indices.

Tests conducted using only PC1 as a predictor showed that PC1 misses many El Niño events that have not developed strongly positive SST anomalies during AMJ. Including the influence of absolute wind power captures every El Niño, but also produces more false positives. Verification using a contingency table, shown in Table 5.1, demonstrates the finding that $MaKE > -0.5\sigma$ has predictive skill with respect to El Niño. A similar metric using Niño 3.4 is also created for comparison. Over each three-month period for which *MaKE* is calculated, the mean of the Niño 3.4 index is also computed. Table 5.2 shows the corresponding results using $mean(Ni\tilde{no}3.4) > 0.2^{\circ}C$ as a predictor (a threshold of $0.2^{\circ}C$ was chosen to give the most generous prediction skill to this predictor). Although several false positives are found, it is notable that *MaKE* correctly predicts all El Niño events using only

Table 5.1: Contingency tables for April-May-June (top) and May-June-July (bottom) for *MaKE* used as a predictor. All 9 observed El Niño events are correctly predicted. The Heidke Skill Scores (HSS) for each period is also shown.

| MaKE | | Observed | | | HSS |
|-------|---------|----------|-------|-------|-------|
| | | El Niño | Other | Total | |
| April | El Niño | 9 | 8 | 17 | 0.482 |
| | Other | 0 | 12 | 12 | |
| | Total | 9 | 20 | 29 | |
| May | El Niño | 9 | 9 | 18 | 0.431 |
| | Other | 0 | 11 | 11 | |
| | Total | 9 | 20 | 29 | |

data from AMJ, although it admittedly outperforms using the mean of Niño 3.4 over this period only slightly, with Heidke skill scores (HSSs) of 0.482 and 0.453, respectively (HSS < 0 indicates a prediction worse than chance, HSS = 0 indicates a prediction equivalent to random chance, and HSS > 0 indicates the fraction of correct predictions that are beyond what is expected by random chance). When this same metric is applied to the May-June-July season, the predictive power of *MaKE* wanes slightly, achieving an HSS of 0.431, while using the mean of Niño 3.4 over this period does not change that result.

Table 5.2: Contingency tables for April-May-June (top) and May-June-July (bottom) for Niño 3.4 used as a predictor, as well as corresponding Heidke Skill Scores (HSS).

| Niño 3.4 | | Observed | | | HSS |
|----------|---------|----------|-------|-------|-------|
| | | El Niño | Other | Total | |
| April | El Niño | 6 | 4 | 10 | 0.453 |
| | Other | 3 | 16 | 19 | |
| | Total | 9 | 20 | 29 | |
| May | El Niño | 6 | 4 | 10 | 0.453 |
| | Other | 3 | 16 | 19 | |
| | Total | 9 | 20 | 29 | |

The analyses described in the previous chapters using $W_{MJO,K}$ focused on identifying El Niño years which are strongly influenced by the MJO, so it is natural to pursue a method for achieving this goal for real-time applications. The *MaKE* index does not have any skill in selecting the El Niño events influenced by the MJO. To achieve this objective, a second index is computed, meant to be used in conjunction with *MaKE*. This second index should only be applied to those events predicted to be El Niño by *MaKE*, as it is of little value in differentiating between El Niño and non-El Niño events. The MJO and Kelvin wave Influence (*MaKI*) index is defined as the minimum value of the linear combination of PC1 and PC2 over a 90-day period:

$$MaKI(t_m) = \min_{0 < t < 90} (PC1(t) + PC2(t)) \quad (5.2)$$

where again t_m indicates monthly frequency and t indicates daily frequency beginning on the first day of each month. Like the *MaKE* index, *MaKI* is defined only for each month. Because the years to which this index is applied are predicted by *MaKE* to be El Niño, the absolute value used in computing *MaKE* can be relaxed due to the fact that negative wind power can be assumed to contribute to the growth of El Niño (Goddard and Philander, 2000; Hu et al., 2014; Lybarger and Stan, 2018). Figure 5.5 shows the monthly time series

of *MaKI* with El Niño events influenced by the MJO highlighted in red.

In this case, the threshold for determining whether the predicted El Niño will be strongly influenced by the MJO is given as $MaKI < -2\sigma$. These events are tending toward El Niño according to *MaKE*, thus PC1 will usually be positive. For this condition to be met, PC2 must have at least one strongly negative phase that dominates PC1 enough to bring their sum below -2σ . The reasoning for only applying this index to events predicted to be El Niño should be clear: if applied to a year tending toward La Niña, many years would meet the $MaKI < -2\sigma$ criterion due to the influence of strongly negative SST anomalies on PC1. Applying this metric to the set of 17 years predicted to be El Niño in AMJ by the *MaKE* metric results in correctly identifying the three years that are strongly influenced by the MJO according to the methodology described in Chapter 2 (1997, 2006, and 2009), as well as identifying three other years as being strongly influenced by the MJO (1992, 2001, and 2016). Figure 5.5 demonstrates that the *MaKE* index correctly predicts each El Niño (red and gray background shading) in April (indicated by the vertical dash-dot red line in each El Niño year), and that the *MaKI* index correctly predicts the El Niño events which are influenced by the MJO (red background shading). The set of years which meet both the $MaKE > -0.5\sigma$ and $MaKI < -2\sigma$ criteria in April are the El Niño years 1997, 2006, and 2009 (all identified by the $W_{MJO,K}$ index as being strongly influenced by the MJO), the ENSO-neutral years 1992 and 2001, and the La Niña year 2016. Table 5.3 summarizes these findings, with *MaKI* achieving an HSS of 0.564 in April when applied to the 17 years that meet the *MaKE* threshold. The MJO influence on El Niño years is shown in Chapter 4 to be due to coherent variations between the MJO wind stress and Kelvin wave activity, so lag correlations are now computed to investigate this relationship with respect to the years selected by these criteria. These lag-correlation plots can also be used to validate whether the events selected by *MaKI* as El Niño events without a link to MJO lack the coherence between the MJO wind stress and oceanic Kelvin waves.

Table 5.3: Contingency tables for April-May-June (top) and May-June-July (bottom) for *MaKI* used as a predictor, as well as corresponding Heidke Skill Scores (HSS). It should be noted that this metric is only applied to the set of years predicted by the *MaKE* index to be El Niño events (n=17).

| MaKI | | Observed | | | HSS |
|-------|--------|----------|-------|-------|-------|
| | | Strong | Other | Total | |
| April | Strong | 3 | 3 | 6 | 0.564 |
| | Other | 0 | 11 | 11 | |
| | Total | 3 | 14 | 17 | |
| May | Strong | 2 | 3 | 5 | 0.368 |
| | Other | 1 | 12 | 13 | |
| | Total | 3 | 15 | 18 | |

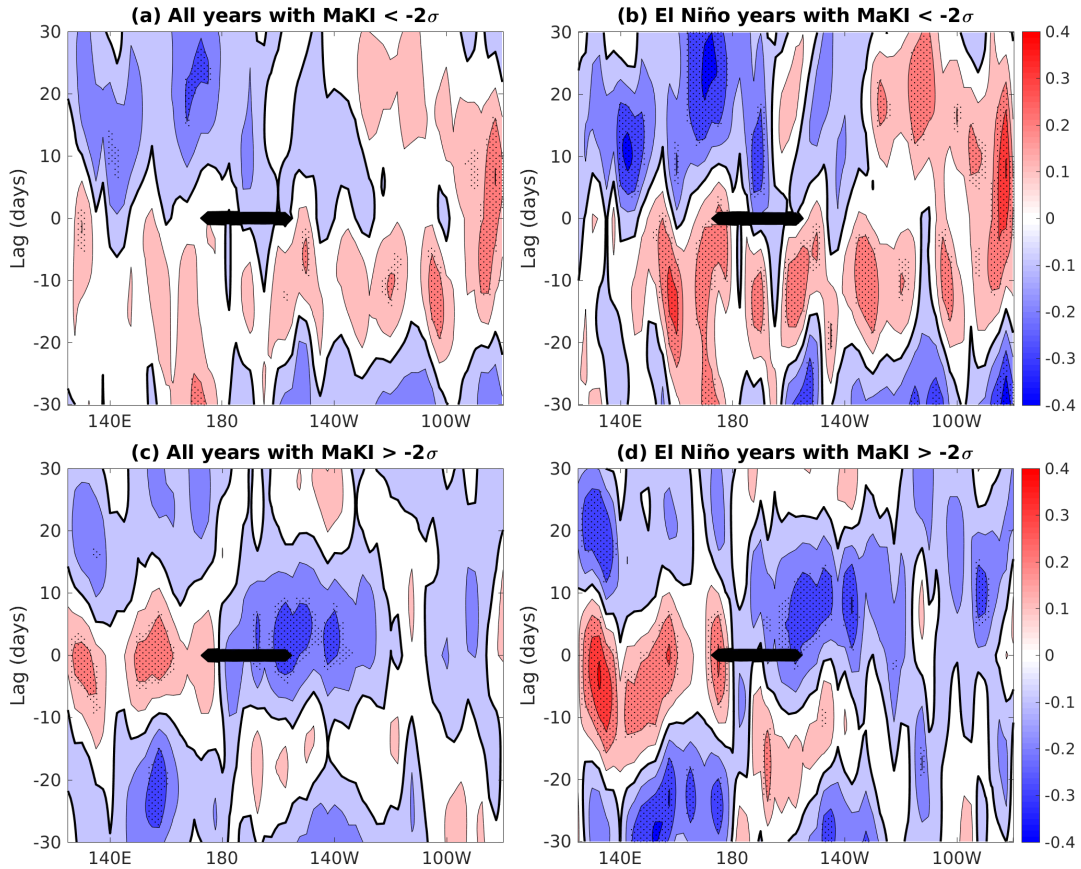


Figure 5.6: Composites of AMJ lag correlation between MJO wind stress in the $W_{MJO,K}$ region and equatorially ($5^{\circ}\text{S} - 5^{\circ}\text{N}$) averaged Kelvin wave depth, defined as the meridional structure of a Kelvin wave projected onto daily anomalies of the 20°C isotherm. The sign convection is such that a downwelling Kelvin wave (positive thermocline anomaly) would be correlated with a westerly MJO wind stress anomaly. Each composite includes only years which meet the $MaKE$ threshold. Shown are composites of (a) all years which also meet the $MaKI$ index threshold (1992, 1997, 2001, 2006, 2009, 2014, and 2016; $n=7$), (b) El Niño years which meet the $MaKI$ threshold (1997, 2006, 2009, and 2014; $n=4$), (c) all years which do not meet the $MaKI$ threshold (1990, 1991, 1993, 1994, 1995, 2002, 2004, 2005, 2012, and 2015; $n=10$), (d) and El Niño years which do not meet the $MaKI$ threshold (1991, 1994, 2002, 2004, and 2015; $n=5$). The zonal extent of the $W_{MJO,K}$ region is blacked out. Positive (negative) lags indicate MJO wind stress leading (lagging) Kelvin wave depth. Stippling indicates statistical significance at the 95% level.

Figure 5.6 shows the AMJ lag correlation between the area average of τ_{MJO} in the $W_{MJO,K}$ region ($3^{\circ}\text{S} - 1^{\circ}\text{N}$, $175^{\circ}\text{E} - 160^{\circ}\text{W}$) and the meridional average ($5^{\circ}\text{S} - 5^{\circ}\text{N}$) of the Kelvin wave component of the anomalies of the 20°C isotherm. Chapter 4 shows that for El Niño events influenced by the MJO wind stress, westerly MJO wind stress anomalies over the $W_{MJO,K}$ region tend to be preceded by upwelling Kelvin wave activity in the western Pacific and followed by downwelling Kelvin waves that propagate into the eastern Pacific. Four different composites are shown, corresponding to whether the year achieves the $MaKI$ threshold and whether that year resulted in El Niño. In each composite shown in Figure 5.6, $MaKE > -0.5\sigma$, and is therefore predicted by that metric to be an El Niño event. Figure 5.6(a) shows the composites of all years (1992, 1997, 2001, 2006, 2009, 2014, and 2016; $n=7$) that meet the condition $MaKI < -2\sigma$ and Fig. 5.6(b) shows the composite of the actual El Niño years (1997, 2006, 2009, 2014; $n=4$). The composites in these two figures consist of years predicted by that metric to be strongly influenced by the MJO wind forcing. Figure 5.6(c) shows the composite of all years (1990, 1991, 1993, 1994, 1995, 2002, 2004, 2005, 2012, and 2015; $n=10$) for which $MaKI > -2\sigma$ and Fig. 5.6(d) shows the composite of the actual El Niño years (1991, 1994, 2002, 2004, 2015; $n=5$). The composites in these two figures consist of years predicted by $MaKI$ to *not* be strongly influenced by the MJO wind forcing. Figure 5.6(b) and (d) show a composite of a subset of years included in (a) and (c) which, in reality, evolve into El Niño. The set of years included in each composite is specified in the caption for Figure 5.6. The El Niño years in Figures 5.6(b) and (d) show essentially the same spatial structures as their counterparts in Figures 5.6(a) and (c), but with stronger amplitudes. An exception to this is the slightly stronger eastward propagation seen in (d) as compared to (c), which looks more like a standing wave. This result contrasts with previous findings of Roundy and Kiladis (2006) who showed a decrease in Kelvin wave phase speeds as the ocean state evolves toward El Niño, though that study investigated the summer and autumn prior to El Niño, and not AMJ as shown here. MJO wind stress is followed by Kelvin wave depth of opposite sign when $MaKI$ does not meet the -2σ threshold (Figures 5.6(c) and (d)), indicating MJO wind stress that is out of phase with

Kelvin wave activity, consistent with the findings of Chapter 4. Curiously, Figures 5.6(c) and (d) also show the development of positive correlations at negative lags, indicating MJO wind stress is preceded by Kelvin wave activity of the same sign. It seems that in these composites, MJO wind stress in this region in AMJ works to reverse Kelvin wave activity. In the $MaKI < -2\sigma$ composites (Figures 5.6(a) and (b)), coherent phasing between MJO wind stress and Kelvin wave activity throughout the basin is seen at negative lags, significantly so in years resulting in El Niño (Figure 5.6(b)). At positive lags, the western and central Pacific Kelvin waves are anticorrelated with MJO wind stress, while the eastern Pacific is positively correlated (Figure 5.6(b)). The composites of events selected by $MaKI$ show coherence between the $W_{MJO,K}$ region and the eastern Pacific at positive lags suggesting that this index is effectively capturing the source of MJO influence on ENSO shown in Chapter 4. Figure 5.6(d) is reminiscent of WCtl shown in Figure 4.9(b).

5.3 El Niño Forecast in CFS-v2

The metrics that have been applied to observations were also applied to the principal components (described in Section 5.1.1) computed for CFS-v2 reforecasts of each year in the period 1980-2014. The PCs were computed for each of the 5 ensemble members. Table 5.4 shows the contingency table using $MaKE$ as a predictor. The same threshold value of -0.5σ as in observations is used for prediction of El Niño events by the model. Table 5.5 shows the contingency table resulting from the use of Niño 3.4 as a predictor. The threshold value of $mean(Niño3.4) > 0.2^\circ C$ in AMJ is used for prediction of El Niño events by CFS-v2, as was done for observations. Nine of the eleven El Niño events observed between 1980-2014 are correctly predicted by $MaKE$, as well as nine false positives, while only five El Niño events are captured using the mean of Niño 3.4 metric, with nine false positives as well. The skill score of the Niño 3.4 predictor measured by HSS is 0.074, just barely outperforming chance, and is outperformed considerably by the $MaKE$ predictor, which achieves an HSS of 0.378. In CFS-v2 both $MaKE$ and Niño 3.4 predictors have a lower forecast skill than

Table 5.4: *MaKE* contingency table as applied to CFS-v2 reforecasts of each year between 1980 and 2014. The Heidke Skill Score is shown.

| MaKE | | Observed | | | HSS |
|--------|---------|----------|-------|-------|-------|
| | | El Niño | Other | Total | |
| CFS-v2 | El Niño | 9 | 9 | 18 | 0.378 |
| | Other | 2 | 15 | 17 | |
| | Total | 11 | 24 | 35 | |

Table 5.5: Niño 3.4 contingency table as applied to CFS-v2 reforecasts of each year between 1980 and 2014. The Heidke Skill Score is shown.

| Niño 3.4 | | Observed | | | HSS |
|----------|---------|----------|-------|-------|-------|
| | | El Niño | Other | Total | |
| CFS-v2 | El Niño | 5 | 9 | 14 | 0.074 |
| | Other | 6 | 15 | 21 | |
| | Total | 11 | 24 | 35 | |

their counterparts computed in observations, providing some hope for improving El Niño prediction.

To explore the probabilistic forecast skill of CFS-v2 using *MaKE* and compare it to that based on Niño 3.4, the receiving operating characteristic (ROC) plots associated with Table 5.4 and Table 5.5 are shown in Figure 5.7 for each ensemble member and predictor. On this ROC plot, any point above the red dotted line outperforms chance, while any point below does not. Each ensemble member for both predictors outperform chance, in agreement with their positive HSS values, but the distance from the center line in the group of points representing the *MaKE* metric for each ensemble member is considerably larger than for the group of points representing the mean of Niño 3.4 metric for each ensemble member. For Niño 3.4, all members achieve a true positive rate (TPR) of 45%, with two

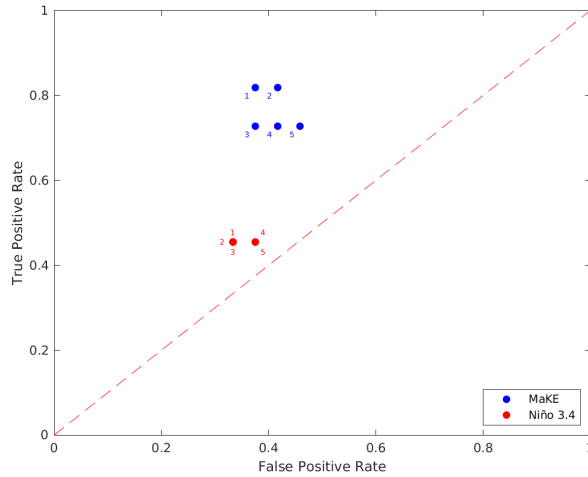


Figure 5.7: Receiver operating characteristic (ROC) plots for each ensemble member of the CFS-v2 reforecasts. ROC plots compare the true positive rate and false positive rate, with any points above the center line outperforming chance. Note that the distance between each point and the center line for *MaKE* (blue) is considerably larger than for Niño 3.4 (red). The numbered labels indicate the ensemble members represented by each point.

members having a false positive rate (FPR) of 37.5% and three having an FPR of 33.3%. That the ensemble members agree so closely for Niño 3.4 could be due to overconfidence in CFS-v2, with error growth outpacing ensemble spread with respect to lead time (Peng et al., 2013).

The mean of Niño 3.4 metric suffers a far more dramatic loss of skill in predicting El Niño than does the metric based on *MaKE*. A possible explanation for this is an insufficient coupling between oceanic and atmospheric processes in CFS-v2, such that the wind variability does not accurately influence the ocean (though the state of the ocean may still strongly influence the atmosphere). This would result in inaccuracies in Niño 3.4 that can be compensated by also directly quantifying the impact of the MJO wind variability on the ocean surface, thus resulting in a more accurate predictor of El Niño events. These results indicate that including the influence of $W_{MJO,K}$ can be a significant source of ENSO

predictability as early as April in CFS-v2 forecasts.

The *MaKI* metric to identify El Niño events which are strongly influenced by the MJO is also applied to the CFS-v2 reforecast years predicted by the *MaKE* metric to be El Niño years. Unlike for observations, this metric does not capture every El Niño year, specifically missing 1986/87 and 2009/10 (the latter of which has been identified as strongly influenced by the MJO in observations). Furthermore, because the satellite-derived wind stress data used in this study is only available going back to 1987, it is possible that years between 1980 and 1987 could have included El Niño events which were strongly influenced by the MJO, which would provide more targets for *MaKI* to forecast. For instance, the 1982/83 El Niño event is known to be of strong amplitude, but little MJO activity was observed in the year prior to that event (Tang and Yu, 2008). It should therefore be expected that *MaKI* does not predict strong influence by the MJO on that event. Indeed, *MaKI* attains a value of -0.54σ in the CFS-v2 reforecast of 1982, and so does not achieve the threshold value of -2σ . This reinforces the idea that *MaKI* has some value in predicting the MJO influence on ENSO. Because so few targets are available for CFS-v2, the best possible outcome for applying this metric to these CFS-v2 reforecasts would be to correctly predict strong MJO influence prior to the El Niño events in 1997 (-0.81σ) and 2006 (-1.03σ). No years meet the threshold of -2σ , though the years which come closest are 2006 and 2012 (-1.59σ , ENSO-neutral).

To demonstrate the lack of coherence between MJO wind stress and SST anomalies in CFS-v2 forecasts, Hovmöller diagrams for the ensemble average, equatorial average ($5^{\circ}\text{S} - 5^{\circ}\text{N}$) zonal MJO wind stress, total wind stress anomalies, and SST anomalies are compared in Figure 5.8. Despite the significant periods and regions over which the MJO wind stress and the total wind stress anomalies are easterly, the SST anomalies show a quite uniform growth of positive anomalies in the central and eastern Pacific after May. The period of negative SST anomalies that emerges in the eastern Pacific in April is accompanied by westerly MJO winds, counter to what should be expected, though there are easterlies in the total wind stress daily anomalies in the central/eastern Pacific during this period. These

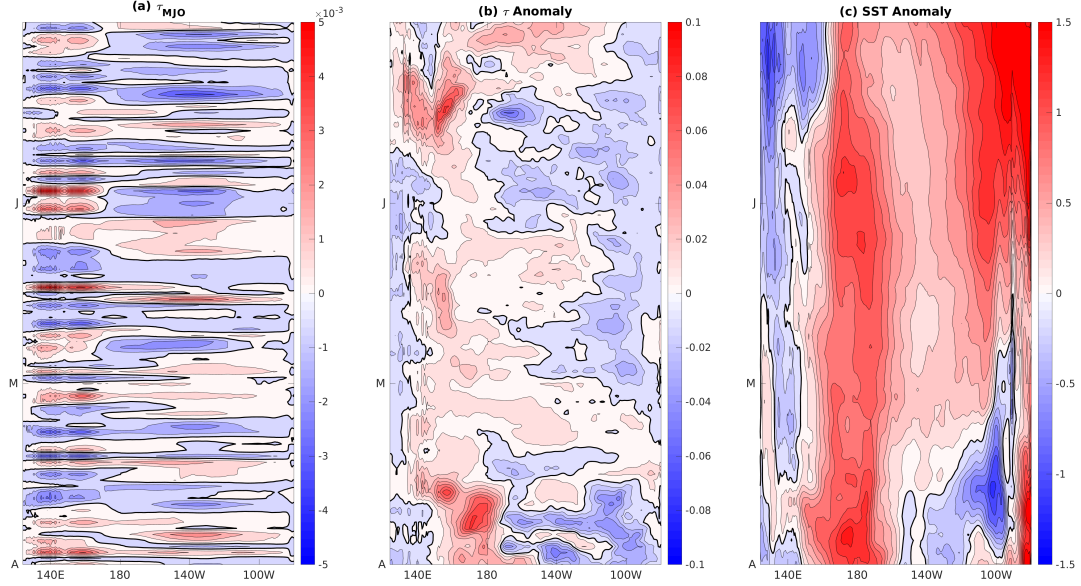


Figure 5.8: Hovmöller diagram of equatorially averaged ($5^{\circ}\text{S} - 5^{\circ}\text{N}$) zonal (a) MJO wind stress, (b) total wind stress daily anomaly, and (c) SST anomaly. Units of wind stress are $N \cdot m^{-2}$, and units of SST anomaly are $^{\circ}\text{C}$

easterly anomalies drive upwelling consistent with the cool SST anomalies during April in this region. Notable periods of easterly anomalies in the total wind stress field in this same region occur in May and June as well, though positive SST anomalies continue to grow during these periods despite the easterlies (indeed, the extensive period of easterly wind stress anomalies in June is accompanied by some of the most rapid SST growth of the three months). One possible explanation for the weak ocean-atmosphere interactions in CFS-v2 could be the shortcomings in the convective parameterization scheme. For example, Wu et al. (2007) showed that in a GCM the MJO, wind stress anomalies, and SST growth became closely associated when the convection scheme was modified.

The fact that *MaKE* performs as well as it does and *MaKI* does not perform at all reinforces the interpretation of the lack of prediction skill in using the metric based on Niño 3.4. That is, the ocean state is affecting wind variability such that including the wind

anomalies in *MaKE* improves model’s ability to forecast El Niño. Because the winds do not project strongly back onto the ocean state, i.e., CFS-v2 does not properly capture the coherence between MJO and Kelvin wave activity seen in MJO-influenced El Niño events, as demonstrated in the previous chapters, *MaKI* fails to capture these events. These results imply that the forecast skill of El Niño can be improved by using other metrics than Niño indices and further improvements in the skill can be achieved by improving the air-sea coupling of the model. Additional information provided by the *MaKI* index could be used to predict some features of El Niño events such as intensity and flavor (not shown here).

5.4 Discussion

The previous chapters focused on differences between El Niño events and found an association between variability in $W_{MJO,K}$ and the earlier development of a flattened, El Niño-like tropical Pacific thermocline state, enhanced Kelvin wave activity, and stronger SST amplitude development at the peak of the event (Lybarger and Stan, 2018). Further, in those events with high $W_{MJO,K}$ variability, a coherence between MJO-related wind stress and Kelvin wave activity in AMJ is found, and sensitivity experiments wherein coherence between those phenomena is enhanced show similarities to sensitivity experiments wherein MJO events are added to the wind stress forcing of the model (Chapter 4). This study uses the covariability of MJO wind stress with oceanic Kelvin waves and SST anomalies to construct a diagnostic framework for El Niño events and applies the diagnostic to a set of seasonal forecasts with the CFV-v2 model. The framework consists of two indices derived from the multivariate EOF analysis of $W_{MJO,K}$ and SST daily anomalies over the domain between 3°S - 1°N and 175°E - 160°W. The first index, *MaKE*, captures years in which either SSTs are consistently above normal, or if not, are compensated by strong wind power associated with coincident MJO and Kelvin wave activity. This index correctly predicts every El Niño using data from AMJ observations. While it does predict more false positives than using a metric based on Niño 3.4, it outperforms that metric according to HSS, albeit slightly. The second index, *MaKI*, is recommended to be used only for those years predicted

to be El Niño by *MaKE*, and correctly predicts which El Niño events are expected to be strongly influenced by MJO, based on using the January-July average $W_{MJO,K}$ index, as defined in Chapter 2. *MaKI* captures the coherence between the MJO wind stress in the tropical central Pacific and Kelvin wave activity in the eastern Pacific identified in Chapter 4 as the driving mechanism of the MJO-El Niño interaction. Lagged correlation plots of El Niño events stratified according to *MaKI* threshold show a coherence (decoherence) between MJO wind stress in the tropical central Pacific and Kelvin wave activity in the eastern Pacific at positive lags in composites of events which achieve (do not achieve) the *MaKI* threshold.

When these metrics are applied to three-month CFS-v2 reforecasts initialized in April, the *MaKE* index is found to strongly outperform the Niño 3.4 metric that was applied to observations. However, application of the *MaKI* index is markedly less successful, with no years achieving the threshold. It is speculated that *MaKE* can predict El Niño due to CFS-v2 capturing the first leg of atmosphere-ocean interactions in the Pacific Ocean, namely, the ocean’s influence on the winds. As the ocean evolves toward an El Niño state, *MaKE* captures the enhanced wind anomalies which, in observations, tend to reinforce that state. In CFS-v2, however, the forcing from the atmosphere to the ocean is not consistent with observations, thus *MaKI* fails because this metric depends on coherence between MJO winds and Kelvin wave activity.

This study exploits the MJO-ENSO relationship to develop metrics which are shown to have skill in predicting El Niño events and the influence of MJO wind stress on the development of those events. This is due to these indices capturing not only the covariability between MJO and Kelvin wave activity, but also the covariability of these phenomena with the SST, which is strongly correlated with thermocline variability primarily in the eastern Pacific, as demonstrated by the zonal structure of the multivariate EOFs seen in Figure 5.3. These indices thus provide a holistic proxy for the MJO influence on the development of El Niño. Future work will involve the application of these indices to seasonal forecast models with more robust coupling between ocean and atmosphere, which should be better able

to capture the relationship between these metrics and ENSO seen in observations. With further development of these indices, they could be applied to ENSO forecasts to predict events and to quantify the MJO influence on those events.

The objectives of this work have been sufficiently achieved. A quantitative definition capturing the MJO influence on ENSO via Kelvin wave activity has been derived and displays a relationship between that index and the development of strong El Niño events, both in observations and a GCM study. It has been shown that $W_{MJO,K}$ variability is associated with lower frequency MJO winds, which more strongly project onto the Kelvin wave state. Coherence between MJO winds and Kelvin wave activity has been shown to be a necessary condition for strong MJO influence on El Niño evolution, but not a necessary condition for El Niño itself, despite the fact that the MJO can have a significant effect on the timing and strength of El Niño events. With respect to the ENSO theory paradigms discussed in Section 1.1, the findings of this work suggest that ENSO is a self-sustained and periodic oscillatory mode for which atmospheric forcing provides the observed irregularity and aperiodicity. A quantitative framework for MJO-ENSO interactions with an underlying mechanistic explanation for that framework has been developed and has been shown to have value for improving ENSO prediction.

Bibliography

- Andersen, J. A., and Z. Kuang, 2011: Moist Static Energy Budget of MJO-like Disturbances in the Atmosphere of a Zonally Symmetric Aquaplanet. *Journal of Climate*, **25** (8), 2782–2804, doi:10.1175/JCLI-D-11-00168.1.
- Batstone, C., and H. H. Hendon, 2005: Characteristics of Stochastic Variability Associated with ENSO and the Role of the MJO. *Journal of Climate*, **18** (11), 1773–1789, doi:10.1175/JCLI3374.1.
- Battisti, D., 1988: Dynamics and Thermodynamics of a Warming Event in a Coupled Tropical Atmosphere Ocean Model. *Journal of the Atmospheric Sciences*, **45** (20), 2889–2919, doi:10.1175/1520-0469(1988)045<2889:DATOAW>2.0.CO;2.
- Bentamy, A., and D. C. Fillon, 2012: Gridded surface wind fields from Metop/ASCAT measurements. *International Journal of Remote Sensing*, **33** (6), 1729–1754, doi:10.1080/01431161.2011.600348.
- Bergman, J. W., H. H. Hendon, and K. M. Weickmann, 2001: Intraseasonal air–sea interactions at the onset of El Niño. *Journal of Climate*, **14** (8), 1702–1719.
- Bjerknes, J., 1969: Atmospheric teleconnections from the equatorial pacific. *Monthly Weather Review*, **97** (3), 163–172, doi:10.1175/1520-0493(1969)097<0163:ATFTEP>2.3.CO;2.
- Boullanger, J.-P., C. Menkes, and M. Lengaigne, 2004: Role of high- and low-frequency winds and wave reflection in the onset, growth and termination of the 1997–1998 El Niño. *Climate Dynamics*, **22** (2-3), 267–280, doi:10.1007/s00382-003-0383-8.

- Chang, P., B. Wang, T. Li, and L. Ji, 1994: Interactions Between the Seasonal Cycle and the Southern Oscillation - Frequency Entrainment and Chaos in a Coupled Ocean-Atmosphere Model. *Geophysical Research Letters*, **21 (25)**, 2817–2820, doi:10.1029/94GL02759.
- Chiodi, A. M., and D. E. Harrison, 2017: Observed El Nino SSTA Development and the Effects of Easterly and Westerly Wind Events in 2014/15. *Journal of Climate*, **30 (4)**, 1505–1519, doi:10.1175/JCLI-D-16-0385.1.
- Choi, K.-Y., G. A. Vecchi, and A. T. Wittenberg, 2013: ENSO Transition, Duration, and Amplitude Asymmetries: Role of the Nonlinear Wind Stress Coupling in a Conceptual Model. *Journal of Climate*, **26 (23)**, 9462–9476, doi:10.1175/JCLI-D-13-00045.1.
- Cravatte, S., J. Picaut, and G. Eldin, 2003: Second and first baroclinic Kelvin modes in the equatorial Pacific at intraseasonal timescales. *Journal of Geophysical Research-Oceans*, **108 (C8)**, 3266, doi:10.1029/2002JC001511.
- DeMott, C. A., N. P. Klingaman, and S. J. Woolnough, 2015: Atmosphere-ocean coupled processes in the Madden-Julian oscillation. *Reviews of Geophysics*, **53 (4)**, 1099–1154, doi:10.1002/2014RG000478.
- Dommenget, D., and Y. Yu, 2016: The seasonally changing cloud feedbacks contribution to the ENSO seasonal phase-locking. *Climate Dynamics*, **47 (12)**, 3661–3672, doi:10.1007/s00382-016-3034-6.
- Duvel, J. P., and J. Vialard, 2007: Indo-Pacific Sea Surface Temperature Perturbations Associated with Intraseasonal Oscillations of Tropical Convection. *Journal of Climate*, **20 (13)**, 3056–3082, doi:10.1175/JCLI4144.1.
- Eisenman, I., L. S. Yu, and E. Tziperman, 2005: Westerly wind bursts: ENSO’s tail rather than the dog? *Journal of Climate*, **18 (24)**, 5224–5238, doi:10.1175/JCLI3588.1.

- Enfield, D. B., 1987: The Intraseasonal Oscillation in Eastern Pacific Sea Levels: How Is It Forced? *Journal of Physical Oceanography*, **17** (11), 1860–1876, doi:10.1175/1520-0485(1987)017<1860:TIOIEP>2.0.CO;2.
- Fedorov, A. V., and S. G. Philander, 2001: A stability analysis of tropical ocean-atmosphere interactions: Bridging measurements and theory for El Nino. *Journal of Climate*, **14** (14), 3086–3101, doi:10.1175/1520-0442(2001)014<3086:ASAOTO>2.0.CO;2.
- Flugel, M., and P. Chang, 1996: Impact of dynamical and stochastic processes on the predictability of ENSO. *Geophysical Research Letters*, **23** (16), 2089–2092, doi:10.1029/96GL01959.
- Flugel, M., P. Chang, and C. Penland, 2004: The role of stochastic forcing in modulating ENSO predictability. *Journal of Climate*, **17** (16), 3125–3140, doi:10.1175/1520-0442(2004)017<3125:TROSFI>2.0.CO;2.
- Gill, A., 1980: Some Simple Solutions for Heat-Induced Tropical Circulation. *Quarterly Journal of the Royal Meteorological Society*, **106** (449), 447–462, doi:10.1256/smsqj.44904.
- Goddard, L., and S. G. Philander, 2000: The energetics of El Nino and La Nina. *Journal of Climate*, **13** (9), 1496–1516, doi:10.1175/1520-0442(2000)013<1496:TEOENO>2.0.CO;2.
- Halkides, D. J., L. E. Lucas, D. E. Waliser, T. Lee, and R. Murtugudde, 2011: Mechanisms controlling mixed-layer temperature variability in the eastern tropical Pacific on the intraseasonal timescale. *Geophysical Research Letters*, **38** (17), doi:10.1029/2011GL048545.
- Hayes, S., L. Mangum, J. Picaut, A. Sumi, and K. Takeuchi, 1991: Toga-Tao - a Moored Array for Real-Time Measurements in the Tropical Pacific-Ocean.

- Bulletin of the American Meteorological Society*, **72** (3), 339–347, doi:10.1175/1520-0477(1991)072<0339:TTAMAF>2.0.CO;2.
- Hendon, H., and M. Salby, 1994: The Life-Cycle of the Madden-Julian Oscillation. *Journal of the Atmospheric Sciences*, **51** (15), 2225–2237, doi:10.1175/1520-0469(1994)051<2225:TLCOTM>2.0.CO;2.
- Hendon, H. H., B. Liebmann, and J. D. Glick, 1998: Oceanic Kelvin waves and the Madden-Julian oscillation. *Journal of the Atmospheric Sciences*, **55** (1), 88–101, doi:10.1175/1520-0469(1998)055<0088:OKWATM>2.0.CO;2.
- Hendon, H. H., M. C. Wheeler, and C. Zhang, 2007: Seasonal dependence of the MJO–ENSO relationship. *Journal of Climate*, **20** (3), 531–543.
- Hu, S., and A. V. Fedorov, 2016: Exceptionally strong easterly wind burst stalling El Niño of 2014. *Proceedings of the National Academy of Sciences of the United States of America*, **113** (8), 2005–2010, doi:10.1073/pnas.1514182113.
- Hu, S., A. V. Fedorov, M. Lengaigne, and E. Guilyardi, 2014: The impact of westerly wind bursts on the diversity and predictability of El Niño events: An ocean energetics perspective: Hu et al.: WWB and ENSO diversity: energetics view. *Geophysical Research Letters*, **41** (13), 4654–4663, doi:10.1002/2014GL059573.
- Huang, B., C.-S. Shin, J. Shukla, L. Marx, M. A. Balmaseda, S. Halder, P. Dirmeyer, and J. L. Kinter, 2017: Reforecasting the ENSO Events in the Past 57 Years (1958–2014). *Journal of Climate*, **30** (19), 7669–7693, doi:10.1175/JCLI-D-16-0642.1.
- Jin, F., J. Neelin, and M. Ghil, 1994: El-Niño on the Devils Staircase - Annual Subharmonic Steps to Chaos. *Science*, **264** (5155), 70–72, doi:10.1126/science.264.5155.70.
- Jin, F. F., 1997: An equatorial ocean recharge paradigm for ENSO .1. Conceptual model. *Journal of the Atmospheric Sciences*, **54** (7), 811–829, doi:10.1175/1520-0469(1997)054<0811:AEORPF>2.0.CO;2.

- Jin, F.-F., L. Lin, A. Timmermann, and J. Zhao, 2007: Ensemble-mean dynamics of the ENSO recharge oscillator under state-dependent stochastic forcing. *Geophysical Research Letters*, **34** (3), L03 807, doi:10.1029/2006GL027372,.
- Kalnay, E., and Coauthors, 1996: The NCEP/NCAR 40-Year Reanalysis Project. *Bulletin of the American Meteorological Society*, **77** (3), 437–472, doi:10.1175/1520-0477(1996)077<0437:TNYRP>2.0.CO;2.
- Kanamitsu, M., W. Ebisuzaki, J. Woollen, S.-K. Yang, J. J. Hnilo, M. Fiorino, and G. L. Potter, 2002: NCEP–DOE AMIP-II Reanalysis (R-2). *Bulletin of the American Meteorological Society*, **83** (11), 1631–1644, doi:10.1175/BAMS-83-11-1631.
- Kapur, A., C. Zhang, J. Zavala-Garay, and H. H. Hendon, 2012: Role of stochastic forcing in ENSO in observations and a coupled GCM. *Climate Dynamics*, **38** (1), 87–107, doi:10.1007/s00382-011-1070-9.
- Kessler, W., M. Mcphaden, and K. Weickmann, 1995: Forcing of Intraseasonal Kelvin Waves in the Equatorial Pacific. *Journal of Geophysical Research-Oceans*, **100** (C6), 10 613–10 631, doi:10.1029/95JC00382.
- Kessler, W. S., and R. Kleeman, 2000: Rectification of the Madden-Julian oscillation into the ENSO cycle. *Journal of Climate*, **13** (20), 3560–3575, doi:10.1175/1520-0442(2000)013<3560:ROTMJO>2.0.CO;2.
- Kirtman, B. P., 1997: Oceanic Rossby wave dynamics and the ENSO period in a coupled model. *Journal of Climate*, **10** (7), 1690–1704, doi:10.1175/1520-0442(1997)010<1690:ORWDAT>2.0.CO;2.
- Kleeman, R., and A. M. Moore, 1997: A theory for the limitation of ENSO predictability due to stochastic atmospheric transients. *Journal of the Atmospheric Sciences*, **54** (6), 753–767, doi:10.1175/1520-0469(1997)054<0753:ATFTLO>2.0.CO;2.

- Larson, S. M., and B. P. Kirtman, 2017: Drivers of coupled model ENSO error dynamics and the spring predictability barrier. *Climate Dynamics*, **48** (11), 3631–3644, doi:10.1007/s00382-016-3290-5.
- Lau, K.-M., 1985: Elements of a Stochastic-Dynamical Theory of the Long-Term Variability of the El Niño/Southern Oscillation. *Journal of the Atmospheric Sciences*, **42** (14), 1552–1558, doi:10.1175/1520-0469(1985)042<1552:EOASDT>2.0.CO;2.
- Levine, A., F. F. Jin, and M. J. McPhaden, 2016: Extreme Noise-Extreme El Nino: How State-Dependent Noise Forcing Creates El Nino-La Nina Asymmetry. *Journal of Climate*, **29** (15), 5483–5499, doi:10.1175/JCLI-D-16-0091.1.
- Levine, A. F. Z., F. F. Jin, and M. F. Stuecker, 2017: A simple approach to quantifying the noise-ENSO interaction. Part II: the role of coupling between the warm pool and equatorial zonal wind anomalies. *Climate Dynamics*, **48** (1-2), 19–37, doi:10.1007/s00382-016-3268-3.
- Levine, A. F. Z., and M. J. McPhaden, 2016: How the July 2014 easterly wind burst gave the 2015-2016 El Nino a head start. *Geophysical Research Letters*, **43** (12), 6503–6510, doi:10.1002/2016GL069204.
- Lucas, L. E., D. E. Waliser, and R. Murtugudde, 2010: Mechanisms governing sea surface temperature anomalies in the eastern tropical Pacific Ocean associated with the boreal winter Madden-Julian Oscillation. *Journal of Geophysical Research: Oceans*, **115** (C5), doi:10.1029/2009JC005450.
- Lukas, R., and E. Lindstrom, 1991: The mixed layer of the western equatorial Pacific Ocean. *Journal of Geophysical Research: Oceans*, **96** (S01), 3343–3357, doi:10.1029/90JC01951.
- Lybarger, N. D., and C. Stan, 2018: The effect of the MJO on the energetics of El Niño. *Climate Dynamics*, **51** (7-8), 2925–2839, doi:https://doi.org/10.1007/s00382-017-4047-5.

- Madden, R., and P. Julian, 1972: Description of Global-Scale Circulation Cells in Tropics with a 40-50 Day Period. *Journal of the Atmospheric Sciences*, **29** (6), 1109–+, doi:10.1175/1520-0469(1972)029<1109:DOGSCC>2.0.CO;2.
- Marshall, A. G., O. Alves, and H. H. Hendon, 2009: A Coupled GCM Analysis of MJO Activity at the Onset of El Niño. *Journal of the Atmospheric Sciences*, **66** (4), 966–983, doi:10.1175/2008JAS2855.1.
- McPhaden, M. J., 1995: The Tropical Atmosphere Ocean Array Is Completed. *Bulletin of the American Meteorological Society*, **76** (5), 739–744, doi:10.1175/1520-0477-76.5.739.
- McPhaden, M. J., 2002: Mixed Layer Temperature Balance on Intraseasonal Timescales in the Equatorial Pacific Ocean. *Journal of Climate*, **15** (18), 2632–2647, doi:10.1175/1520-0442(2002)015<2632:MLTBOI>2.0.CO;2.
- McPhaden, M. J., and X. Yu, 1999: Equatorial waves and the 1997–98 El Niño. *Geophysical Research Letters*, **26** (19), 2961–2964, doi:10.1029/1999GL004901.
- McPhaden, M. J., X. Zhang, H. H. Hendon, and M. C. Wheeler, 2006: Large scale dynamics and MJO forcing of ENSO variability. *Geophysical Research Letters*, **33** (16), doi:10.1029/2006GL026786.
- Menkes, C. E., M. Lengaigne, J. Vialard, M. Puy, P. Marchesiello, S. Cravatte, and G. Cambon, 2014: About the role of Westerly Wind Events in the possible development of an El Niño in 2014. *Geophysical Research Letters*, **41** (18), 6476–6483, doi:10.1002/2014GL061186.
- Moore, A. M., and R. Kleeman, 1996: The dynamics of error growth and predictability in a coupled model of ENSO. *Quarterly Journal of the Royal Meteorological Society*, **122** (534), 1405–1446, doi:10.1002/qj.49712253409.
- Moore, A. M., and R. Kleeman, 1999a: Stochastic forcing of ENSO by the intraseasonal oscillation. *Journal of Climate*, **12** (5), 1199–1220.

- Moore, A. M., and R. Kleeman, 1999b: The nonnormal nature of El Nino and intraseasonal variability. *Journal of Climate*, **12** (10), 2965–2982, doi:10.1175/1520-0442(1999)012<2965:TNNOEN>2.0.CO;2.
- Munnich, M., M. Cane, and S. Zebiak, 1991: A Study of Self-Excited Oscillations of the Tropical Ocean Atmosphere System .2. Nonlinear Cases. *Journal of the Atmospheric Sciences*, **48** (10), 1238–1248, doi:10.1175/1520-0469(1991)048<1238:ASOSEO>2.0.CO;2.
- Neelin, J., 1991: The Slow Sea-Surface Temperature Mode and the Fast-Wave Limit - Analytic Theory for Tropical Interannual Oscillations and Experiments in a Hybrid Coupled Model. *Journal of the Atmospheric Sciences*, **48** (4), 584–606, doi:10.1175/1520-0469(1991)048<0584:TSSSTM>2.0.CO;2.
- Neelin, J. D., D. S. Battisti, A. C. Hirst, F. F. Jin, Y. Wakata, T. Yamagata, and S. E. Zebiak, 1998: ENSO theory. *Journal of Geophysical Research-Oceans*, **103** (C7), 14 261–14 290, doi:10.1029/97JC03424.
- Nishida, T., T. Kitakado, H. Matsuura, and S.-P. Wang, 2011: Validation of the Global Ocean Data Assimilation System (GODAS) data in the NOAA National Centre for Environmental System (NCEP) by theory, comparative studies, applications and sea truth, Victoria, Seychelles.
- Peng, G., H.-M. Zhang, H. P. Frank, J.-R. Bidlot, M. Higaki, S. Stevens, and W. R. Hankins, 2013: Evaluation of Various Surface Wind Products with OceanSITES Buoy Measurements. *Weather and Forecasting*, **28** (6), 1281–1303, doi:10.1175/WAF-D-12-00086.1.
- Penland, C., and L. Matrosova, 1994: A Balance Condition for Stochastic Numerical-Models with Application to the El-Nino-Southern Oscillation. *Journal of Climate*, **7** (9), 1352–1372, doi:10.1175/1520-0442(1994)007<1352:ABCFSN>2.0.CO;2.

- Penland, C., and P. Sardeshmukh, 1995: The Optimal-Growth of Tropical Sea-Surface Temperature Anomalies. *Journal of Climate*, **8 (8)**, 1999–2024, doi:10.1175/1520-0442(1995)008<1999:TOGOTS>2.0.CO;2.
- Picaut, J., E. Hackert, A. J. Busalacchi, R. Murtugudde, and G. S. E. Lagerloef, 2002: Mechanisms of the 1997–1998 El Niño–La Niña, as inferred from space-based observations. *Journal of Geophysical Research: Oceans*, **107 (C5)**, 5–1–5–18, doi:10.1029/2001JC000850.
- Puy, M., J. Vialard, M. Lengaigne, and E. Guilyardi, 2016: Modulation of equatorial Pacific westerly/easterly wind events by the Madden-Julian oscillation and convectively-coupled Rossby waves. *Climate Dynamics*, **46 (7-8)**, 2155–2178, doi:10.1007/s00382-015-2695-x.
- Roundy, P. E., and G. N. Kiladis, 2006: Observed relationships between oceanic kelvin waves and atmospheric forcing. *Journal of Climate*, **19 (20)**, 5253–5272, doi:10.1175/JCLI3893.1.
- Saha, S., and Coauthors, 2006: The NCEP climate forecast system. *Journal of Climate*, **19 (15)**, 3483–3517.
- Saha, S., and Coauthors, 2013: The NCEP Climate Forecast System Version 2. *Journal of Climate*, **27 (6)**, 2185–2208, doi:10.1175/JCLI-D-12-00823.1.
- Seiki, A., Y. N. Takayabu, K. Yoneyama, N. Sato, and M. Yoshizaki, 2009: The Oceanic Response to the Madden-Julian Oscillation and ENSO. *Sola*, **5**, 93–96, doi:10.2151/sola.2009-024.
- Stan, C., and L. Xu, 2014: Climate simulations and projections with a super-parameterized climate model. *Environmental Modelling & Software*, **60**, 134–152, doi:10.1016/j.envsoft.2014.06.013.
- Suarez, M., and P. Schopf, 1988: A Delayed Action Oscillator for Enso.

- Journal of the Atmospheric Sciences*, **45** (21), 3283–3287, doi:10.1175/1520-0469(1988)045<3283:ADAOFE>2.0.CO;2.
- Takahashi, K., and B. Dewitte, 2016: Strong and moderate nonlinear El Niño regimes. *Climate Dynamics*, **46** (5-6), 1627–1645, doi:10.1007/s00382-015-2665-3.
- Tang, Y., and B. Yu, 2008: MJO and its relationship to ENSO. *Journal of Geophysical Research: Atmospheres*, **113** (D14), doi:10.1029/2007JD009230.
- Thompson, C. J., and D. S. Battisti, 2000: A linear stochastic dynamical model of ENSO. Part I: Model development. *Journal of Climate*, **13** (15), 2818–2832, doi:10.1175/1520-0442(2000)013<2818:ALSDMO>2.0.CO;2.
- Tziperman, E., M. Cane, and S. Zebiak, 1995: Irregularity and Locking to the Seasonal Cycle in an Enso Prediction Model as Explained by the Quasi-Periodicity Route to Chaos. *Journal of the Atmospheric Sciences*, **52** (3), 293–306, doi:10.1175/1520-0469(1995)052<0293:IALTTS>2.0.CO;2.
- Wang, B., A. Barcilon, and Z. Fang, 1999: Stochastic dynamics of El Niño-Southern Oscillation. *Journal of the Atmospheric Sciences*, **56** (1), 5–23, doi:10.1175/1520-0469(1999)056<0005:SDOENO>2.0.CO;2.
- Wang, C., 2001: A Unified Oscillator Model for the El Niño–Southern Oscillation. *Journal of Climate*, **14** (1), 98–115, doi:10.1175/1520-0442(2001)014<0098:AUOMFT>2.0.CO;2.
- Wang, C., C. Deser, J.-Y. Yu, P. DiNezio, and A. Clement, 2017: El Niño and Southern Oscillation (ENSO): A Review. *Coral Reefs of the Eastern Tropical Pacific*, P. W. Glynn, D. P. Manzello, and I. C. Enochs, Eds., Vol. 8, Springer Netherlands, Dordrecht, 85–106, doi:10.1007/978-94-017-7499-4_4.
- Wang, W., M. Chen, A. Kumar, and Y. Xue, 2011: How important is intraseasonal surface wind variability to real-time ENSO prediction?: ISV IMPACTS ON ENSO PREDICTION. *Geophysical Research Letters*, **38** (13), doi:10.1029/2011GL047684.

- Weisberg, R. H., and C. Wang, 1997: A Western Pacific Oscillator Paradigm for the El Niño-Southern Oscillation. *Geophysical Research Letters*, **24** (7), 779–782, doi:10.1029/97GL00689.
- Wheeler, M. C., and H. H. Hendon, 2004: An all-season real-time multivariate MJO index: Development of an index for monitoring and prediction. *Monthly Weather Review*, **132** (8), 1917–1932, doi:10.1175/1520-0493(2004)132<1917:AARMMI>2.0.CO;2.
- Wu, X., L. Deng, X. Song, G. Vettoretti, W. R. Peltier, and G. J. Zhang, 2007: Impact of a modified convective scheme on the Madden-Julian Oscillation and El Niño–Southern Oscillation in a coupled climate model. *Geophysical Research Letters*, **34** (16), doi:10.1029/2007GL030637.
- Wyrtki, K., 1975: El Niño—The Dynamic Response of the Equatorial Pacific Ocean to Atmospheric Forcing. *Journal of Physical Oceanography*, **5** (4), 572–584, doi:10.1175/1520-0485(1975)005<0572:ENTDRO>2.0.CO;2.
- Wyrtki, K., 1985: Water displacements in the Pacific and the genesis of El Niño cycles. *Journal of Geophysical Research: Oceans*, **90** (C4), 7129–7132, doi:10.1029/JC090iC04p07129.
- Zebiak, S., 1989: On the 30-60 Day Oscillation and the Prediction of El Niño. *Journal of Climate*, **2** (11), 1381–1387, doi:10.1175/1520-0442(1989)002<1381:OTDOAT>2.0.CO;2.
- Zebiak, S., and M. Cane, 1987: A Model El-Niño Southern Oscillation. *Monthly Weather Review*, **115** (10), 2262–2278, doi:10.1175/1520-0493(1987)115<2262:AMENO>2.0.CO;2.
- Zhang, C., 2005: Madden-Julian Oscillation. *Reviews of Geophysics*, **43** (2), doi:10.1029/2004RG000158.

- Zhang, C. D., 2001: Intraseasonal Perturbations in Sea Surface Temperatures of the Equatorial Eastern Pacific and Their Association with the Madden–Julian Oscillation. *Journal of Climate*, **14** (6), 1309–1322, doi:10.1175/1520-0442(2001)014<1309:IPISST>2.0.CO;2.
- Zhang, C. D., and J. Gottschalck, 2002: SST anomalies of ENSO and the Madden-Julian oscillation in the equatorial Pacific. *Journal of Climate*, **15** (17), 2429–2445, doi:10.1175/1520-0442(2002)015<2429:SAOEAT>2.0.CO;2.
- Zhang, H.-M., J. J. Bates, and R. W. Reynolds, 2006a: Assessment of composite global sampling: Sea surface wind speed. *Geophysical Research Letters*, **33** (17), doi:10.1029/2006GL027086.
- Zhang, H.-M., R. W Reynolds, and J. J Bates, 2006b: Blended and gridded high resolution global sea surface wind speed and climatology from multiple satellites: 1987–present.
- Zhu, J., A. Kumar, B. Huang, M. A. Balmaseda, Z.-Z. Hu, L. Marx, and J. L. Kinter, 2016: The role of off-equatorial surface temperature anomalies in the 2014 El Nino prediction. *Scientific Reports*, **6**, 19677, doi:10.1038/srep19677.

Curriculum Vitae

Nicholas D. Lybarger graduated from Father Ryan High School, Nashville, Tennessee, in 2009. He received his Bachelor of Science in Physics and Earth and Planetary Sciences from the Johns Hopkins University, Baltimore, Maryland, in 2013. His research interests include tropical variability, time scale interactions, ocean-atmosphere coupled processes, and seasonal prediction. He received the Summer Research Fellowship from George Mason University for the Summer 2019 semester, a competitive award for funding to complete this dissertation.